Universidade Federal da Paraíba

Centro de Tecnologia

PROGRAMA DE PÓS-GRADUAÇÃO EM ENGENHARIA CIVIL E AMBIENTAL

– MESTRADO –

EVALUATION OF DAMAGE IN REINFORCED CONCRETE SLABS WITH DIFFERENT REINFORCEMENT RATIOS USING DAMAGE INDICATORS AND NUMERICAL MODELING

By

Gabriel Soares Ferreira

Dissertação de Mestrado apresentada à Universidade Federal da Paraíba para obtenção do grau de Mestre

João Pessoa – Paraíba **Agosto de 2019**

Universidade Federal da Paraíba

Centro de Tecnologia

PROGRAMA DE PÓS-GRADUAÇÃO EM ENGENHARIA CIVIL E AMBIENTAL

– MESTRADO –

AVALIAÇÃO DE DANOS EM LAJES MACIÇAS DE CONCRETO ARMADO COM DIFERENTES TAXAS DE ARMAÇÃO MEDIANTE INDICADORES DE DANO E MODELAGEM NUMÉRICA

Dissertation submitted in partial fulfilment of the requirements for the Degree of Master in Civil and Environmental Engineering at Federal University of Paraiba.

Dissertation by

Gabriel Soares Ferreira

Supervisor

Prof. Dr. Roberto Leal Pimentel

João Pessoa – Paraíba **August, 2019**

Catalogação na publicação
Seção de Catalogação e Classificação

F383e Ferreira, Gabriel Soares.
EVALUATION OF DAMAGE IN REINFORCED CONCRETE SLABS WITH DIFFERENT REINFORCEMENT RATIOS USING DAMAGE INDICATORS AND NUMERICAL MODELING / Gabriel Soares Ferreira. - João Pessoa, 2019.
123 f.

Dissertação (Mestrado) - UFPB/CT.

1. Slabs. 2. Damage. 3. Cracking. 4. Modeling. 5. Reinforcement. I. Título

UFPB/BC

"AVALIAÇÃO DE DANOS EM LAJES MACIÇAS DE CONCRETO ARMADO COM DIFERENTES TAXAS DE ARMAÇÃO MEDIANTE INDICADORES DE DANO E MODELAGEM NUMÉRICA"

GABRIEL SOARES FERREIRA
Dissertação aprovada em 26 de agosto de 2019

Período Letivo: 2019.2

Prof. Dra. Roberto Leal Pimentel – UFPB
Orientador

Prof. Dr. Aline Figueirêdo Nóbrega de Azerêdo – UFPB
Examinadora Interna

Prof. Dr. Flávio de Souza Barbosa – UFJF
Examinador Externo

João Pessoa/PB
2019

AGRADECIMENTOS

Agradeço primeiramente a Deus, porque com braço forte me sustentou e com mão poderosa me guiou a mais essa conquista. Dedico minha vitória à minha guerreira mãe Maria Cleide Soares de Sousa e ao meu pai Antonio Ferreira do Nascimento (*in memoriam*), pois nunca mediram esforços para que pudesse ter acesso ao bem mais valioso: conhecimento.

Agradeço ao meu orientador, Prof. Roberto Leal Pimentel, o qual aprendi a admirar e respeitar, pela paciência que teve nos momentos mais difíceis, pelo incentivo, apoio, de dedicação e fundamentalmente por acreditar em minha capacidade.

Agradeço aos meus familiares pelo apoio e companheirismo, aos amigos que sempre estiveram presentes, aos que oram por mim e, principalmente, àqueles que me estenderam a mão quando precisei.

Agradeço aos servidores do LABEME/UFPB (Sebastião, Delby, Otoniel, Mizo, Beto, Cláudio), sem os quais não teria sido possível a realização desta pesquisa.

Agradeço aos professores do programa e as servidoras Miriam e Sara, que muito me ajudaram a chegar aqui.

Agradeço aos alunos do PIBIC (Chiara e Lucas) e aos voluntários (Gabriela, João e Leonardo), como também a Rafaelle Finotti e demais membros da PEC/UFJF que ajudaram a tornar essa pesquisa possível.

Obrigato a todos que colaboraram para que os frutos dessa pesquisa fossem colhidos.

RESUMO

A presença de fissuras em uma estrutura é um fato que chama a atenção sobre potenciais problemas de funcionalidade ou perda de capacidade resistente. Lajes de concreto armado têm um padrão diferente de fissura em comparação com as vigas, onde as fissuras tendem a se espalhar na superfície do elemento, não necessariamente atingindo as bordas da laje, com profundidade visível a partir da mesma. A taxa de armadura também é um fator que pode mudar esse padrão. Para avaliar o efeito do dano no padrão de fissuração, nas freqüências naturais e formas modais em lajes de concreto armado, foram testadas duas dessas estruturas com diferentes dimensões e taxas de armadura em ambas as direções, nas quais foram induzidas fissuras por aplicação de carga estática, seguidas por testes modais usando excitação de impacto. Extraindo frequências e modos usando o software StarModal, diferentes índices de danos foram avaliados para comparar ambas as lajes, atentando que o padrão de fissuração foi diferente para ambas as estruturas. Para entender o motivo de um comportamento diferente (estimado como causado por uma mudança no comportamento isotrópico para ortotrópico devido a fissuras), ambas as lajes foram modeladas numericamente utilizando elementos finitos. O modelo considerando a perda da rigidez no elemento finito que continha a fissura e nos elementos vizinhos mostrou-se mais adequado que o modelo onde a rigidez era reduzida em todos os elementos que atingiam o momento de fissuração, seja na comparação em frequência ou por forma modal através do parâmetro MAC. Modelos isotrópicos e ortrotrópicos não apresentaram diferenças significativas entre si, o que traz resultados inconclusivos sobre a transição de comportamento de isotrópico para ortrotrópico como causa do diferente padrão de fissuração. As tangentes nas curvas experimentais carga versus deslocamento no carregamento e descarregamento apresentaram valores relativamente próximos indicando que os modelos, embora elaborados para o estágio de descarregamento, também podem ser aplicados na fase de carregamento.

PALAVRAS-CHAVE: Lajes, dano, fissuração, modelagem, armadura

ABSTRACT

Slabs of reinforced concrete (RC) have a different crack pattern in comparison to beams, where the cracks in bending tend to spread on the surface of the element. The reinforcement ratio is also a factor that can change this pattern. In order to evaluate the effect of damage on cracking pattern, natural frequency and mode shapes in RC slabs, two of such structures with different dimensions and reinforcement ratios in both directions were tested, in which cracks were induced through application of static load, followed by modal tests using impact excitation. Extracting the frequencies and mode shapes using StarModal software, different damage indexes were used to compare both slabs, bearing in mind that differences in the cracking pattern occurred in both structures. To understand the reason for a different behavior, both slabs were modelled numerically using finite elements. The model considering the loss of stiffness in the finite element which have the crack and its nearby elements showed better results than the model in which the stiffness reduction was applied in all elements that reached the cracking moment; the comparison was made through the evaluation of frequencies and modal parameter MAC, which indicate that the cracking affects locally the stiffness of the elements. Isotropic and orthotropic models did not show significant diferences among themselves, what brings inconclusive results about the transition from isotropic to orthotropic behavior as the cause of different cracking pattern. The slopes in loading and unloading stages presented values relatively close to each other, indicating that the models, although adjusted for unloading stage, can also be used for the loading stage.

KEYWORDS: Slabs, damage, cracking, modeling, reinforcement

INDEX

LIST OF FIGURES

LIST OF TABLES

1. INTRODUCTION

The design of civil engineering structures is made worldwide using building code requirements where it is expected that the most unfavorable load cases are considered, so that the structure remains safe and functional along its lifetime. However, during its use, structures can be subjected to severe load conditions that can affect their integrity. Additionally, even if undamaged, it is of growing interest to monitor the structural performance and level of integrity, optimizing the maintenance and repair operations whose costs grows with the damage level. An interesting strategy is the use of nondestructive tests, which can provide information without damaging the structure .

Different classifications for nondestructive tests are available in literature. A well known classification was proposed by Rytter (1993) based on the deepness of the information provided by the tests. Another classification proposed by Saadt *et al* (2004) is based either on the detection capabilities of the techniques (with global techniques having the capability to detect and locate the damage) or on the available information about the damaged structure (based or not in models).

Considering the point of view of material's behavior, the detection techniques can be either linear or nonlinear. On linear techniques, as mentioned by Zamuy *et al* (2014), the behavior is considered approximately linear even after the damage, within a certain range of excitation, where there is a direct relationship between vibratory properties (natural frequencies, mode shapes and damping ratio) and changes in physical properties (mass, stiffness and damping). Considering the nonlinear techniques, specially in structures of cracked reinforced concrete, the consideration of nonlinearity is more realistic, since nonlinearity is an intrinsic condition of this material (Ebrahimian e*t al*,2017). The occurrence of super and subharmonics, for example, which are originated from nonlinear behavior, were studied by Gianninni *et al* (2003). Responses depending on the level of excitation is another characteristic of nonlinearity, as studied by Waltering *et al* (2008) or Hamad *et al* (2010).

The behavior of cracks during the process of excitation is also a source of nonlinearity when they open and close, what is called breathing cracks (Nguyen, 2013; Andreaus and Baragatti, 2009; Chrondros *et al*, 2001; Paolo *et al*, 2014).

Still about the cracking process of reinforced concrete (RC) structures, it is influenced by the reinforcement ratio. However, in comparison to RC beams, that are investigated to a large extent, reinforced concrete slabs have a different patern of

cracking, what brings doubts about the use, for slabs, of beam-based linear or nonlinear damage evaluation methods.

This work makes an investigation over the usability of linear and nonlinear techniques to evaluate damage in two reinforced concrete slabs with different reinforcement ratios in both longitudinal and transverse directions. Both slabs received stepped growing static load (steps being based on the design collapse load), followed by dynamic tests after each step to evaluate the changes in their modal properties as the induced damage increases. The crack pattern and evolution with the applied load is also detected. A numerical model of both slabs is then produced based on the experimental data to help finding, as a first goal, the best cracking model that can be used in both tested structures.

It is also important to mention that this work is result of a cooperation between UFPB and Federal University of Juiz de For a (UFJF) in the modeling, experimental testing and processing of the data, with fundraise of the project PROCAD/CAPES: Rede de Cooperação Acadêmica em Durabilidade de Estruturas – Experimentação e Modelagem Rede de Cooperação Acadêmica em Durabilidade de Estruturas – Experimentação e Modelagem.

Main objective:

Evaluate damage in reinforced concrete slabs having different reinforcement ratios and damaged by bending (where the behavior is naturally nonlinear) using linear and nonlinear techniques based on the experimental data and numerical modelling.

Specific objectives:

- Evaluate the viability of using linear damage indicators (based on changes of eigenfrequency, mode shapes or damping ratios) in concrete slabs with different reinforcement ratios and different crack patterns;
- Evaluate the viability of using a nonlinear damage indicator, based on the ratio of changes of natural frequency along the decay signal induced by an applied impact
- Create a numerical model of slabs initially as linear elastic material and adjust it using experimental data (frequencies and mode shapes);

- Evaluate a better crack model that can be used in both slabs (that present different crack pattern);

The structure of the dissertation is the following: in the first chapter an Introduction about the theme was shown. Chapter 2 makes a literature review on the topics related to the research. Chapter 3 presents the materials and methods used in the investigation. Chapter 4 shows the results obtained and a discussion about them. The final chapter have the conclusions about the research.

2. LITERATURE SURVEY

2.1. Damage detection techniques: linear and nonlinear aproaches

The presence of cracks in reinforced concrete structures is a sign of problems and can have several origins: due to loading (excessive or not), foundation problems, design errors, among others. Since cracking changes the structure's physical properties, it can be related with changes in vibratory properties, like natural frequencies, mode shapes or damping ratios, for the detection, localization and quantification of damage. The research on damage detection techniques based on vibration-data began in late 1970s in aerospace structures. Applications regarding this in different structures and employing different techniques can be cited (Zanuy et al., 2014; Capozucca and Magagnini, 2017; Xu et al., 2018; Cao et al., 2017). The choice of the damage evaluation technique depends on the level of information that can be extracted from data as well as on the structural behavior after damage.

A review of damage detection techniques can be found in Sinou (2009), Das, Saha and Patro (2016), Fand and Quiao (2010), and Jassim *et al* (2013). By considering the structural behavior, two groups of techniques can be specified: linear and nonlinear techniques.

2.1.1. Linear techniques

The group of linear techniques considers that the structure is approximately linear after damage, within a certain range of excitation, and consequently a direct relationship is assumed between changes in vibratory properties (natural frequencies, mode shapes and damping ratios) and changes in physical properties (mass, stiffness and damping). The magnitude and the amount of modes affected will depend on the severity and location of the damage as these two factors can affect modes differently.

Fan and Quiao (2010) made a classification of these techniques into four categories: based on mode shape, based on curvature mode shape changes, based on natural frequencies, and on a combination of natural frequencies and mode shapes.

2.1.1.1. Changes in natural frequency

Changes in natural frequency associated to damage is the most popular and used method in structural assessment. Its use is simple for two main reasons: first, the use of a few sensors is enough for many applications. The second point is that frequencies are less subjected to the influence of noise and can be obtained with a relative confidence.

The simplest model consists of an undamped system having mass *m* and attached to a spring of stiffness *k*, vibrating at one of its natural frequencies. The respective natural frequency of this model is given by Equation 1:

$$f = \frac{1}{2\pi}\sqrt{\frac{k}{m}} \quad (1)$$

Based on Equation 1**,** it can be seen the frequencies of the damaged or undamaged structure is mainly related to the stiffness of the system since cracks don't imply in mass changes. Based on this information, as the damage produce stiffness reduction, it results in changes of frequency (reduction), which can be associated to damage.

As mentioned by Fan and Quiao (2010), natural frequency-based methods can be divided into two groups: the forward problem and the inverse problem. In the forward problem there is a damaged structure with location and severity known and the frequency changes must be determined. In the inverse problem, the frequency is known but the position and intensity of damage is the desired information.

According to Doebling et al. (1996), Lifshitz and Rotem (1969) presented what may be the first journal article to propose damage detection via vibration measurements. They used the shift in natural frequencies through changes in Young's modulus, what can be associated to the frequency change as a damage indicator, an example of inverse problem. The use of frequency change in damage detection can be found in several studies along the literature evolution (Pan *et al*, 2019; Lee and Chung, 2000; Springer *et al*, 1988).

2.1.1.2. Changes in damping ratio

The dissipation of energy provided by crack friction in reinforced concrete is an interesting source for damage index that can be more sensitive than natural frequency decrease. Tests made by Modena et al. (1999) on panels of reinforced concrete indicated that the presence of small cracks caused trivial changes in natural frequencies (due to little decreases or uncertainties) but noticeable changes in damping.

Corroborating the limitation of frequency change on damage detection, Pandey and Biswas (1994) pointed that the localization of damage using such changes is difficult since damage at two different locations associated with a certain amount of damage can produce the same frequency change.

Experimental tests made by Bovsunovsky (2004) concluded that the source of dissipation on cracks is not always provided by friction of crack surfaces: the energy dissipation in an edge non-propagating fatigue crack is caused mainly by the elastoplastic zone in the vicinity of crack tip.

Different authors have explored damping as a damage index (Xu *et al*, 2018; Pešić *et al*, 2015; Hsu *et al*, 2014; Limongelli and Carvelli, 2015; Cao *et al*, 2017). Limitations of damping usage are its difficulty of measurement and sensibility to environmental conditions such as temperature and humidity (Modena *et al*, 1999). A state-of-art about the use of damping can be found in Cao *et al* (2017).

2.1.1.3. Changes in mode shapes and mode shape curvature

In comparison to natural frequency or damping changes, the mode shapes and their derivatives (the curvatures and their numerical adjustments) have more advantages. Since the mode shape is a spatial information for each natural frequency, they contain local information that can be used directly in the detection of multiple damages and their evolution. On the other hand, this method requires more sensors and is more susceptible to noise disturbance than natural frequency measurements, which may hinder the detection of damage (Pandey *et al*, 1991). In the same article, Pandey *et al* (1991) used the curvature of mode shape instead (second derivative of mode shape obtained through a central difference approximation).

In literature it could be seen that damage detection techniques based on mode shapes and derivatives has been used successfully (Cao et al, 2014; Ratcliffe, 2000; Wahab and De Roeck, 1999), because they come from the fact that damage affects mode shapes (and its derivatives). Roy (2017) presented a damage localization method using the derivative of mode shapes of an intact and a damaged frame simulating a building. Frans et al (2017) used variation of mode shape curvature of a truss bar modelled numericaly and observed changes in nearby nodes, associating it to damage. Rucevskis et al. (2016), in turn, employed modal curvature to detect damage on metal

plates but without the need of a baseline for the undamaged state, and successfully detected the existing damage.

Still on curvature of mode shapes, the use of different approximation functions has been cited in literature. Ratcliffe (1997) proposed an indicator based on a relationship of modal curvature affected by damage and a third-degree polynomial representing the undamaged stage. As an improvement, Qiao et al (2007) proposed the use of a fourth-degree polynomial. Dessi and Camerlengo (2015) used sine and cosine functions to model the mode shape of and Euler-Bernouli cantilever beam, using several indicators reported in literature and based in curvature. Jiao et al (2015) evaluated numerically the use of Chebyshev polynomials aiming to obtain the curvature of bridges beams. Xu et al (2017) evaluated the use of modal curvature adjusted by polynomials in aluminium plates.

2.1.1.4. Modal Assurance Criterion (MAC), Coordinate Modal Assurance Criterion (COMAC) and other assurance criteria

The Modal Assurance Criterion (MAC) is a scalar constant that evaluates the degree of linearity (consistency) between two modal vectors. It shows more sensibility to large differences and little sensibility to small differences in the mode shapes, producing a good statistic indicator and a degree of consistency between mode shapes. The MAC between two sets of vectors $\{\varphi_A\}$ and $\{\varphi_X\}$ can be expressed by Equation 2:

$$MAC\ (i,j) = \frac{\left|\{\varphi_A\}_i^T\{\varphi_X\}_j\right|^2}{(\{\varphi_A\}_i^T\{\varphi_A\}_i)(\{\varphi_X\}_j^T\{\varphi_X\}_j)} \quad (2)$$

Making use of orthogonality for comparison of two mode shapes vectors, MAC ranges from zero (representing no consistent correspondence) to one – what represents that two sets of data are fully correlated. Based on this fact, a low MAC value for the same resonant frequency can be interpreted as a damage indicator (Pastor *et al*, 2012).

As mentioned by Allemang (2003), MAC has several applications listed on literature, like:

- Validation of experimental modal models;
- Correlation with analytical modal models (mode pairing);
- Correlation with operating response vectors;

- Mapping matrix between analytical and experimental modal models;
- Modal vector error analysis;
- Modal vector averaging;
- Experimental modal vector completion and/or expansion;
- Weighting for model updating algorithms;
- Modal vector consistency/stability in modal parameter estimation algorithms;
- Structural fault/damage detection;
- Quality control evaluations;
- Optimal sensor placement.

Though MAC criteria can assess the orthogonality of two data sets of mode shapes, its limitation lies in not showing the exact points where this comparison has low correspondence. To overcome this issue, a new indicator based on correlation between vectors was proposed by Lieven and Ewins (1988). This way, the Co-Ordinate Modal Assurance Criterion (COMAC) identifies the co-ordinates at which the correspondence of two data sets is poor, that is, those parts of the structure which are contributing to low degrees of correlation. The COMAC factor at a point *i* between n sets of mode shapes is given by Equation 3:

$$COMAC\ (i) = \frac{\left(\sum_{j=1}^{n}\left|(\Phi_A)_{ij}(\Phi_B)_{ij}^{*}\right|\right)^2}{\sum_{j=1}^{n}\left|((\Phi_A)_{ij})\right|^2 \sum_{j=1}^{n}\left|((\Phi_B)_{ij})\right|^2} \quad (3)$$

where *n* defines the number of correlated mode shapes, $(\Phi_A)_{ij}$ and $(\Phi_B)_{ij}$ denote the j^{th} value at a point *i* for the states (eg. numerical, experimental) A and B respectively.

Other assurance criterion factors were developed like Weighted Modal Analysis Criterion (WMAC), Partial Modal Analysis Criterion (PMAC) (Heylen, 1990), Modal Assurance Criterion Square Root (MACSR) (O'Callahan, 1998), Scaled Modal Assurance Criterion (SMAC) (Brechlin *et al*, 1998), Modal Assurance Criterion Using Reciprocal Vectors (MACRV) (Wei *et al*, 1990), Enhanced Coordinate Modal Assurance Criterion (ECOMAC) (Hunt, 1992), Mutual Correspondence Criterion (MCC) (Milecek, 1994), Inverse Modal Assurance Criterion (IMAC) (Mitchell, 2001), Frequency Response Assurance Criterion (FRAC) (Heylen and Lammens, 1996; Fregolent and D'Ambroglo, 1997).

2.1.2. Nonlinear techniques

As mentioned by Frizzarin *et al* (2010), the techniques based on modal parameters as previously mentioned (based on natural frequencies, damping and mode shapes) have an important difference from the methods based on identification of anomalies, which are the nonlinear methods.While in the methods based on classical modal parameters, damage is revealed though a difference in behavior between undamaged and damaged conditions (becoming compromised if the data of the undamaged state is unknown or unavailable), in the methods based on nonlinearity, the anomaly itself reveals the damage, without any reference to the undamaged state.

In cracked reinforced concrete structures, nonlinearity is an intrinsic condition of this material. The crack pattern during the excitation stage or immediately after it is relevant in nonlinear methods and there are two major cracking models: the models that consider the cracks remaining open (called open crack models), and the models considering cracks opening and closing (called breathing cracks models) (Nguyen, 2013; Andreaus et al.,2007; Chondros et al., 2001). Breathing cracks, in special, are sources of nonlinearity because they change the stiffness of the structure during the process of vibration. The majority of the works explored this feature of breathing cracks through use of cyclic excitation (Cheng et al., 1999; Andreaus and Baragatti, 2011; Bovsunovsky and Surace, 2005; Xu and Castel, 2016).

Still in the group of nonlinear damage detection techniques, the use of impact excitation in concrete structures remains less explored, although it is a quick assessment technique, with data being promptly acquired by few sensors positioned on the structure. The majority of works using this technique are devoted to beams. Neild et al. (2003) carried out tests with impact excitation on beams for increasing damage levels produced by static load intercalated by modal tests, and explored the changes of natural frequency along the decay as a nonlinear assessment method. An addition to the previous research line was made by Zhu and Law (2007) who applied the Hilbert-Huang Transform on cracked reinforced concrete beams to evaluate the changes in natural frequency along the decay. Wang et al. (2012), in turn, tested reinforced concrete beams and proposed a window width to evaluate the natural frequencies after the impact.

Different from beams, reinforced concrete slabs have a crack pattern in which the existing cracks tend to spread on the surface of the structure. Still, a factor that can affect the crack pattern is the reinforcement ratio. Han (2011) observed that the transverse reinforcement in one-way slabs can restrain flexural crack opening, indicating that this reinforcement can modify the cracking pattern, as was also observed by Lantsoght et al. (2013) in slabs under concentrated load. The influence of reinforcement ratio in RC slabs was also noticed when they were subjected to blast loads because the deformation and damage degree decreased with the increase of this ratio (Yao et al., 2016).

The major use of damage index models and crack models in literature is for beams ellements. In this work, the investigation about the applicability of them is made for reinforced concrete one-way slabs. Although the cracking pattern and deformation of one–way slabs is different from beams, the support conditions of the tested structures (similar to simply supported beam) and the results of previous investigations justify the research interest.

2.2. Crack modeling

Cracks are among the events that can affect structure and so the evaluation of damage produced by them is a typical application of structural health monitoring. In the literature, the crack modeling fall in three main categories: local stiffness reduction, continuous models and discrete spring models. A review of these and other models can be found in Meruane (2016). The choice of the best crack model depends, among other, in the structure behavior (linear or not) and the number of dimensions it has. If detailing the stress-strain distribution around the crack is necessary, a finite element in three or two dimensions is adequate, while a one dimension model is better for beam-like or fames structures. The representation of breathing effect in cracks can be made by the use of nonlinear contact elements or constraints (Xu and Castel, 2016; Nandi and Neogy, 2002). However, iterative models with meshing update may be required in order to provide precise information like location and depth of crack (Carneiro and Inman, 2002).

The methods in the first group (local stiffness reduction, also called smeared crack models) are the simplest approaches to develop a finite model of a damaged structure since it is just required a well refined mesh in order to reduce the stiffness component (as bending stiffness, for example) in the elements where the damage is located [7, 8, 9].

An adequate model requires a fine mesh and the main question relies on the amount of stiffness reduction in each element with crack in order to match global modal parameters. Coming from experimental data, it is possible to quantify and localize damage. The method is well consolidated for use in beam elements and many applications can be found in literature (Pandey and Biswas, 1991; Zou et al, 2002; Dixit and Hanagud, 2011; Pandey and Biswas, 1994).

In the second group of methods (discrete spring or lumped flexibility models), the cracks are represented by spring elements without mass (Patil and Maiti, 2003), allowing the cracked element to separate in two parts linked by the springs. Since the elements along the crack can change position, the model can represent the severity of the damage.

In the third group of methods, the strain-stress distribution around the crack in the continuous cracked models is defined by a decay function, in an attempt to clearly represent significant properties of crack (like location and depth). Christides and Barr (1984) tested this method in beams and obtained great correlation between the experimental and predicted frequencies. A validation of the formulation was made by Shen and Pierre (1990) using finite element models for comparison and, going beyond, extended the same model validity for single edge breathing cracks. Sinha et al. (2002) followed the studies by developing a model for multi-cracked beams and discovered that the exponential decay of Christides and Barr (1984) could be approximated by a linear decay. Although the model of Sinha et al. (2002) not accurate at high frequencies, it is simple for use and can be applied in structures of low-frequency (like slabs).

3. MATERIALS AND METHODS

3.1. The slabs specimens

Two reinforced concrete slabs were tested in laboratory. Although they had similar dimensions, their reinforcement ratio was different in both directions as their bearing capacity. Both slabs were 0.08 m thick and simply supported along all their width. Figure 1 shows a sketch of both tested slabs.

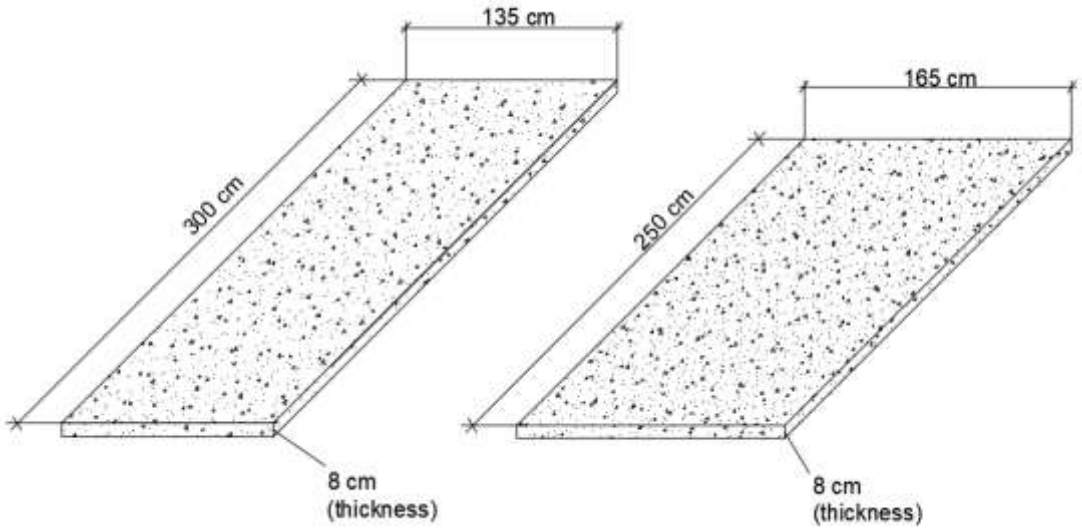

(a) (b)

Figure 1 – Sketch of the slab (a) S1 and (b) S2

3.1.1. Fist slab (S1)

The first slab was named S1 and had a length of 3.0 m and a width of 1.35 m, with rebars of 5.0 mm diameter spaced 9.0 cm along the width and 22.0 cm along the length.

The rebar used was type CA-50 (yielding strength 500 MPa) of 5,0 mm diameter. Fifteen bars with 3,0 m of length and spaced every 9,0 cm along the width were used in main reinforcement ,and fourteen bars with 1,5 m length and spaced every 22,0 cm were used along the length. All bars were bent 4,0 cm and 90º in the ends. The longitudinal and transverse reinforcement ratio in S1 was, respectively, 2.15 cm^2/m and 0.98 cm^2/m.

The S1 casting used concrete with 25 MPa compression strength. The mix in terms of unit weight was 1:2,26:2,60-0,54, where, one unit in weight of cement was

mixed to 2,26 units of sand and 2,60 units of gravel, using a water/cement ratio of 0,54. The cement used was CPV-ARI, a rapid hardening cement. No additives were used.

In order to evaluate the compression resistance, fifteen speciments of 10 cm diameter and 20 cm height were cast, according to the Brazilian standard NBR NM33 and the curing process last 21 days under shadowed place, following the standard NBR 5758.

Table 1 shows the results of compression tests for the speciments. The characteristic strength (fck) found was of 24,7 MPa, a bit lower than the design fck (25 MPa).

CHARACTERISTIC STRENGTH – S1		
Speciment	Load (kgf)	Strength (MPa)
1	20000	25,465
2	23200	29,539
3	24800	31,576
4	19000	24,192
5	22000	28,011
6	19000	24,192
7	22000	28,011
8	22600	28,775
9	22600	28,775
10	23900	30,430
11	23600	30,048
12	22600	28,775
13	27000	34,377
14	22000	28,011
15	22000	28,011

Table 1 – Characteristic strength of concrete speciments – S1.

3.1.2. Second slab (S2)

The second slab, named S2, had a length of 2.50 m and was 1.65 m wide, using rebars of 6.3 mm spaced 7.0 cm along the width and 7.5 cm along the length, and a concrete of 30 MPa of compression strength. The longitudinal and transverse reinforcement ratio in the slab were, respectively, 4,36 cm^2/m and 4,05 cm^2/m. The mix in terms of unit weight was 1:2,42:1,21-0,46. Four specimens with the same dimensions of the ones used in S1 were cast to evaluate the compression strength but were tested for

compression more than 28 days after casting. The average strength was 32,59 MPa. Table 2 shows the results of compression tests for the speciments.

CHARACTERISTIC STRENGTH – S2	
Speciment	Strength (MPa)
1	31,00
2	33,12
3	33,38
4	32,87

Table 2 – Characteristic strength of concrete speciments – S2.

3.2. Equipment used on tests

3.2.1. Load Cell

Load cell is a transducer equipment that converts force into electrical signals proportional to the load. The load cell used had a capacity of 1 MN (Figure 2) and 0.1 kN resolution connected to an Ahlborn data logger model Almemo 2890-9.

Figure 2 – Load cell used for static load aplication.

3.2.2. LVDTs (Linear Variable Differential Transformer)

LVDT (Linear Variable Differential Transformer ou Transformador Diferencial Variável Linear) is a displacement sensor that converts linear movements into a signal. It basically contains some coils that create current according to the tip position. The LVDTs were used for measuring the slab deflection in static load tests, and had a sensibility of 0,01mm, as illustrated in Figure 3.

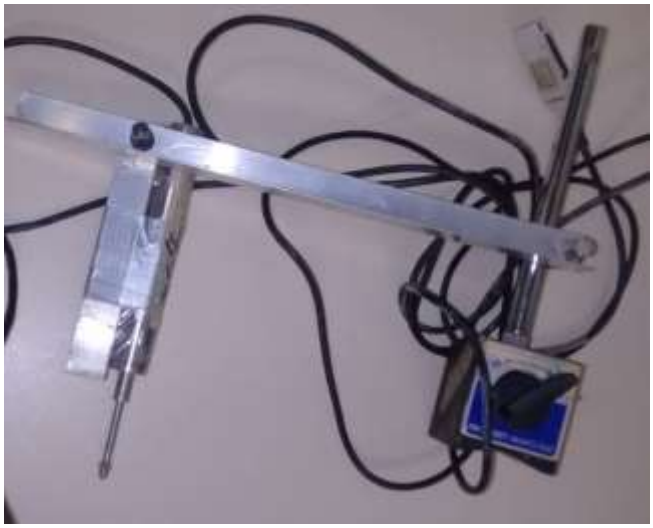

Figure 3 – One of the LVDT sensors used on tests.

3.2.3. Impact hammer

An instrumented impact hammer consists of a hammer that uses tips of different stiffness and a piezoelectric cell inside its head to measure the applied force. Therefore, when the structure is excited, a current is generated and read by an acquisition system.

There are tips with different stiffness that can be used. The choice depends on the stiffness of the structure under test. The stiffer the structure, the shorter is the impulse length and, as result, the longer is the frequency range. Analogously, the more flexible the tip the shortest is the excited frequency range. In the test case, the chosen head was the most flexible one, in order to concentrate the impact energy in the lower frequency range, which contained the structural frequencies of interest. The model used in both slabs was Type 8208 from Brüel&Kjaer as shown in Figure 4.

Figure 4 – Impact hammer used on tests highlighting the tip used. (Source: Product brochure, modified)

According to the equipment brochure, hammer tips allow to control the amplitude and decay of impact. This can be seen in Figure 5(a), where it can be seen the shape of impulse function as a function of the hammer tip; the stiffer the tip the short is the duration of the hammer blow. Figure 5(b) exhibit force spectra of the hammers showing the frequency response as a function of the used impact tip. The tip used for testing both slabs was the medium one as highlighted in Figure 5(a).

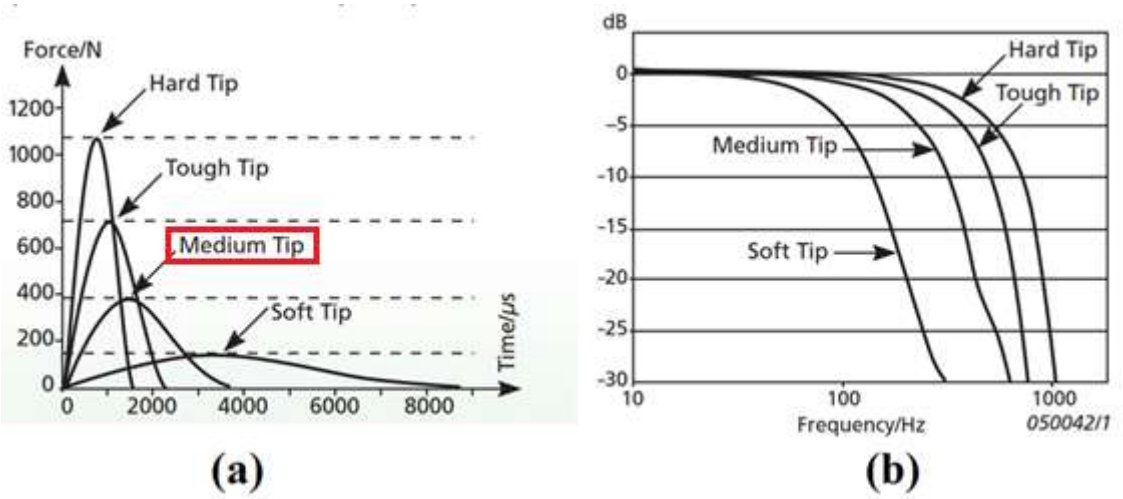

Figure 5 – (a) shape of impulse function (b) spectra of the hammers. (Source: Product brochure)

3.2.4. Piezoelectric accelerometer

Similarly to load cells, accelerometers are also among the equipments called transducers, that work converting mechanical energy into electrical current. The process in an accelerometer is different since it uses an auxiliary mass. According to EWINS (1984), when the structure is excited, the group move together, where the ratio of acceleration of auxiliary mass and accelerometer body (x"/y") is unitary for a range of frequencies from zero up to the transducer's resonant frequency. When the body of the accelerometer moves, the auxiliary mass moves relative to the transducer body causing a deformation of the piezoelectric crystal, generating a current that is transmitted to the acquisition system.

In both tests the accelerometer employed was a Isotron® 752A13 from Endevco®, sensitivity of 1V/g (nominal) and able to work in a frequency range until 100 kHz. It can be seen in Figure 6.

Figure 6 – Accelerometer used for testing

3.2.5. Signal conditioner

The signals produced by the impact hammer or the accelerometers cannot be directly read by the acquisition system due to their low intensity. In order to overcome it, the sinals need to be previously conditioned, and that works in two ways: amplifying current or tension. The conditioner used for both sensors was model 4416B from Endevco®, as can be seen in Figure 7.

Figure 7 – Signal conditioner

3.2.6. Spectrum analyser

The acquisition system consisted of a spectrum analyser; it measures and process the conditioned signals from sources of excitation and response. From the processed signals it is possible to get the modal properties of the structure (damping ratio, natural

frequencies and mode shapes). The analyser used in tests was SignalCalc® Quattro, from Data Physics.

3.3. Slab testing

3.3.1. Impact excitation

Before modal testing, a mesh used for measurement and excitation was marked on S1 surface and the same mesh was marked under the slab to follow the crack evolution as the load levels increased. The 300 cm of length were divided into six parts of 48,33 cm each and the 135 cm of width were divided into four parts of 28,75 each. Additional points were marked along the central line of the slab. Another additional point was marked in order to be the driving point where the response should be acquired. This way, S1 had a total of 42 test points. Figure 8(a) illustrate the modal mesh used for experimental tests side by side to the in situ mesh shown in Figure 8(b). The definition of mesh dimensions, excitation and measurement points were done based on a numerical model in order to get the three first mode shapes of the structure.

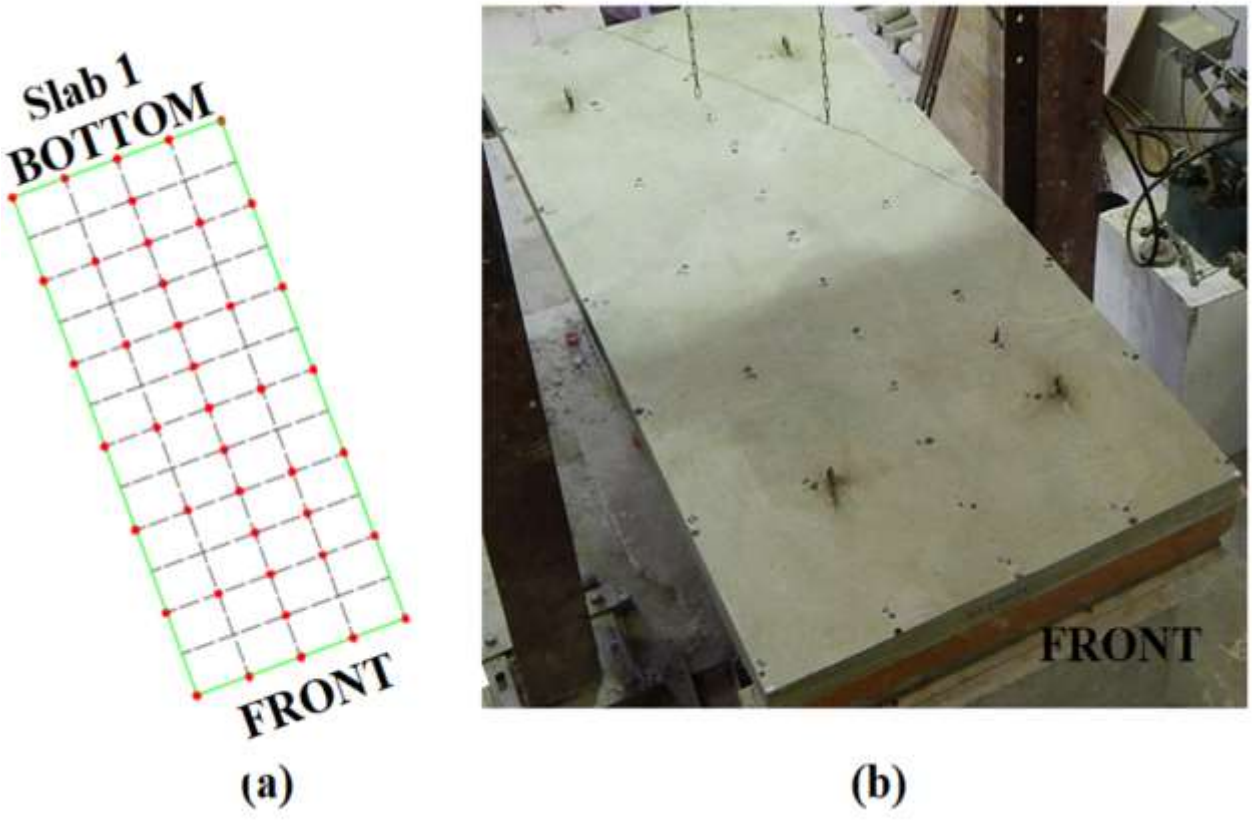

Figure 8 – S1 marked nodes (a) in scheme and (b) in place.

In S2, due to its different dimensions in comparison with S1, an approximately square mesh was employed, with points being 25 cm by 25.6 cm apart along the width and length, respectively, with a total of 77 test points (see Figure 9). In both slabs, the definition of the mesh dimensions were based on obtaining a good resolution for mode shapes, particularly for the first mode, that was similar to the one of a simply supported beam. This was also the main reason for using additional points in the central line of S1. On the other hand, although S2 behaved as a beam-like structure, the way the modes were going to change with increasing damage was unknown. That was the reason to use a denser mesh and an additional driving point, as will be discurssed later on.

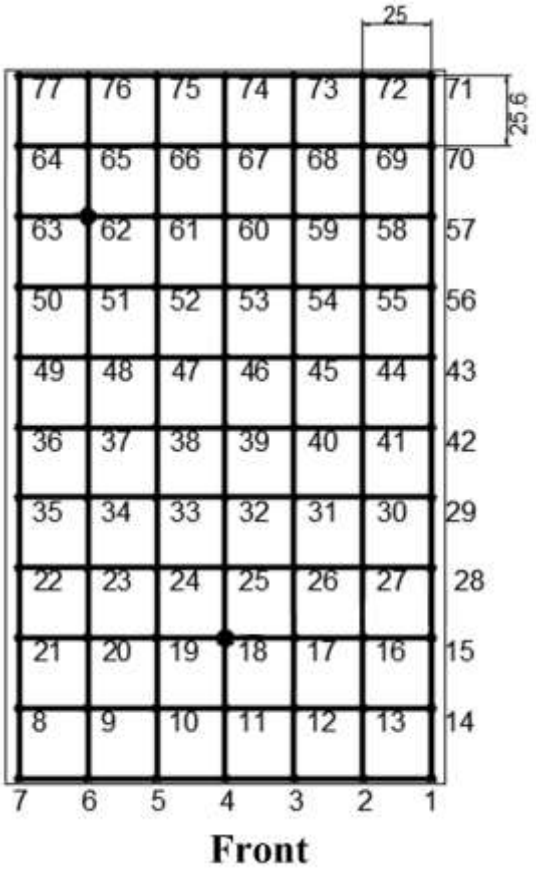

Figure 9 – Mesh used in S2 showing the marked nodes.

After marking the points that were used in modal testing, both slabs were raised using iron cables. Figure 10 shows S1 in its final position for testing. Both slabs were simply supported along their width extremities but using different metallic profiles for

that. Figure 11 shows the support used in S1, being conceived to be a roller and pinned support. Figure 12 shows a detail of S2 supports.

Figure 10 – Side view of S1 showing the continuous support line.

(a) (b)

Figure 11 – Detail of continuous support line of S1 from (a) front side and (b) bottom side

Figure 12 – Detail of continuous support line of S2 (both bottom and front)

After positioning the slab on its final position, the next step was performing a modal testing to evaluate modal properties of the uncracked structure and compare their evolution as the damage increased. Figure 13 illustrate the final position of both mesh and driving point used in both slabs. In S1 a single driving point was used while two driving points were used in S2. The modal testing was performed after each load level was applied and removed in slabs S1 and S2.

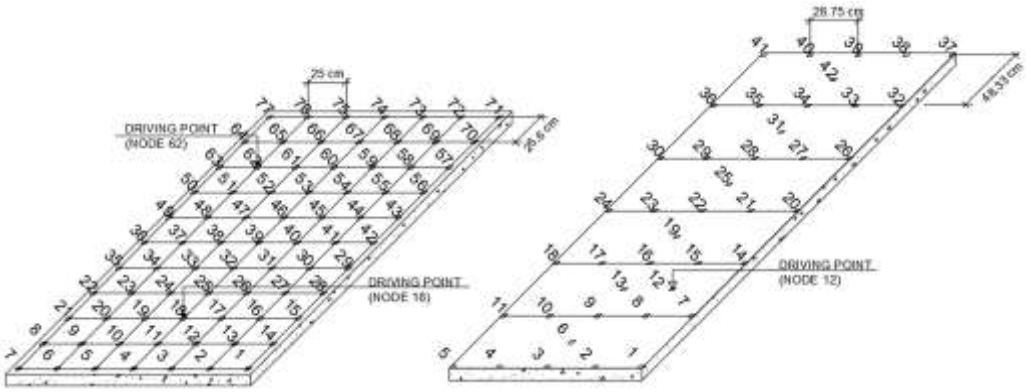

(a) (b)

Figure 13 – Nodes and driving point positions for slabs (a) S2 ans (b) S1.

The excitation was applied in each point using an instrumented impact hammer B&K model 8210. At the driving point in S1 (the point of the experimental mesh where the response acquisition was recorded), an Endevco accelerometer model 752A13 was placed, while the impact hammer excited all the points, one at a time, to perform a modal test. In the case of S2, based on the reciprocity tests (that will be explained later on), the excitation remained fixed at two points while the accelerometer moved along the points of the experimental mesh. The spectrum analyzer SignalCalc Quattro was employed to acquire the excitation and response signals and was connected to a PC Notebook. Each acquired signal lasted 4s and had 4096 points for the tests in S1, and 8s with 8192 points for the tests in S2 (that means an acquisition ratio of 1024 points per second), using in both cases five impacts in each test point so as to obtain average Frequency Response Functions (FRFs) with minimized noise effects, as will be explained later on.

The choice of candidates for driving points (where the excitation or response remained fixed) was priorly made using a simple numerical model (that also was used for testing the mesh definition). For S2, for example, the five first modes had frequencies of 18,24 Hz, 42,26 Hz, 75,72 Hz, 107,25 Hz and 127,92 Hz). In order to confirm the frequencies, adjust the acquisition ratio and verify if the slabs were in the linear-elastic state, several initial tests were performed. Such tests were of linearity, repeatability and reciprocity (HERMEZ et al. 2012; RAO, 2012).

The purpose behind the linearity test is to verify if the relationship between output response and input excitation is constant for a given frequency response function (FRF). This means that the FRF does not depend on input magnitude, what can be evaluated by performing several tests in the same point at different input levels. Then the responses are overlapped to evaluate similarities between them. The reciprocity tests verify if the waves from the excitation do not depend on the input location, and follow the same transfer path. That was verified by applying the excitation at a point X and measuring the response at a point Y and then reversing the configuration by swapping between response and excitation points. An overlap of FRF is expected if the structure is linear. The final verification, repeatability principle, as its name suggests, states that identical samples tested within the same configuration should demonstrate an equal structural behavior. This was made exciting a same point more than once and evaluating if there was difference on the FRFs obtained. Through repeatibility tests it was observed that there was convergence of the average FRF for five excitations (10 and 15 excitations were also tested). It was also noticed that there was an approximate difference of up to 10%. Figure 14 illustrate a modal testing performed

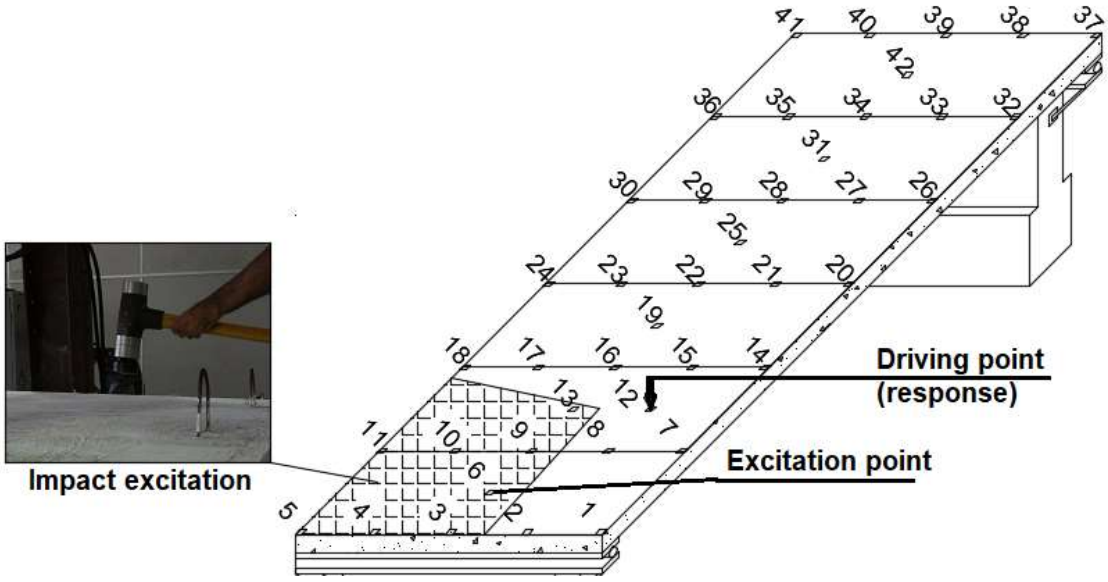

Figure 14 – Illustration of modal test in S1

3.3.2. Static tests

Both slabs used the same load system to perform static load test, using three metallic beams, two dividing the free span in three equal parts (positioned at 1/3 and 2/3 of slab's main span) and the third beam along the central length line. Figures 15 to 17 shows the load application for both slabs.

Figure 15 – Static load application in S1 (side view).

Figure 16 – Static load application in S1 (superior view).

(a) (b)

Figure 17 – Static load system to induce cracking in S2 (a) superior view and (b) side view.

The deflection of slabs according to load level was also of interest. To do that, two LVDT sensors were used above S2. Due to problems in one of the sensors, only

LVDT number 1 was available for S2. The position of the sensors is shown in Figure 18 and Figure 19 shows the LVDTs in use.

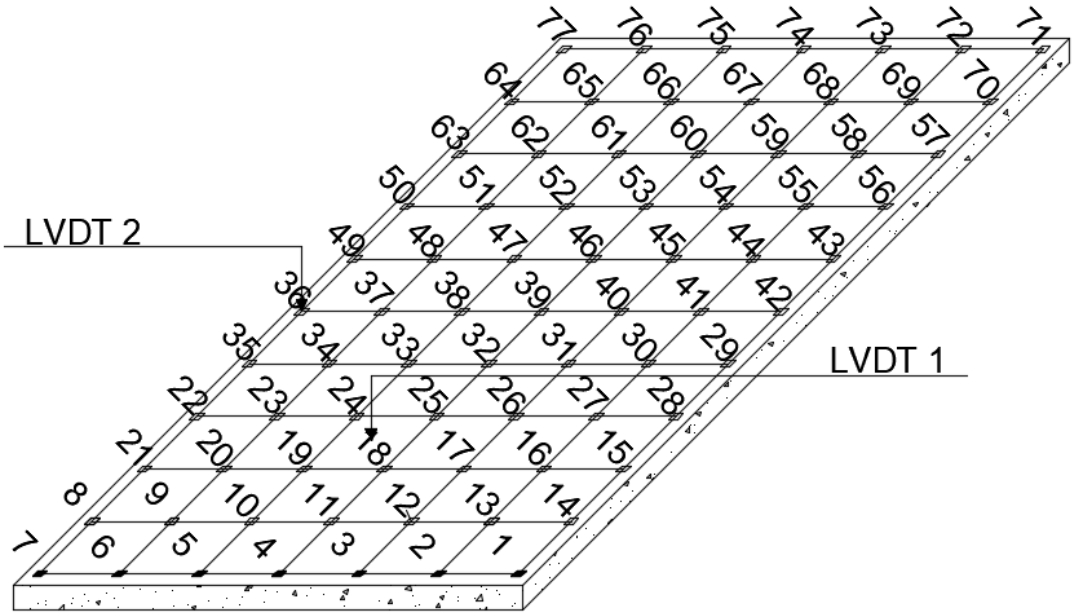

Figure 18 – Distribution of LVDT sensors in S2

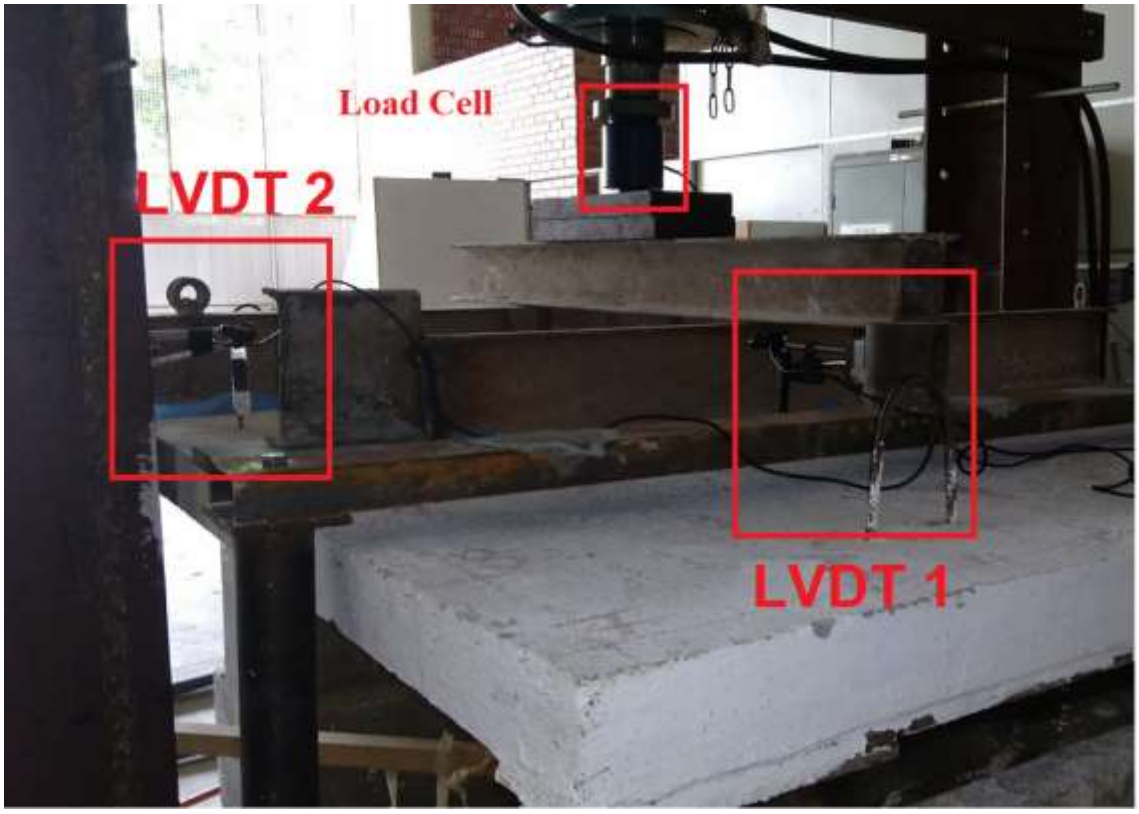

Figure 19 – LVDT used on S2 to measure deflection during static load test

Considering that both slabs were subjected to the same loading configuration but had different reinforcement ratios, the evolution and distribution of crack pattern was also of interest. To follow the evolution with the increase of static load, the same experimental mesh was marked under each slab and the cracks were painted using different colors and line types, as illustrated in Figure 20 for S2.

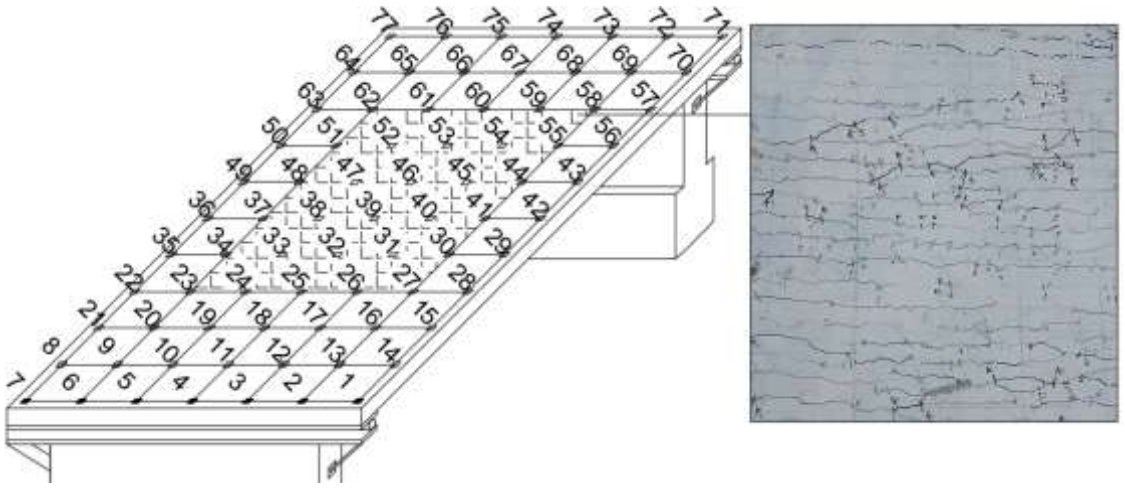

Figure 20 – Illustration of mesh marked under the S2 to follow crack evolution with static load increase.

3.4. Data processing

Natural frequencies and mode shapes from both slabs were obtained using StarModal software v5.3. A polynomial and least-squares complex exponential curve-fitting algorithm is used for extracting the vibration parameters. After importing all FRFs from the whole modal test into a model with nodes previously created and equal to the experimental mesh used on each slab (as illustrated in Figures 21 and 22), the resonant peak is identified using a frequency curve-fitting range that includes all the measurements (as Figure 23 shows). The user defines the range and the number of frequencies in a selected band around the peaks. This is then repeated for the other frequencies. Frequencies and mode shapes are then obtained (Figures 24 and 25).

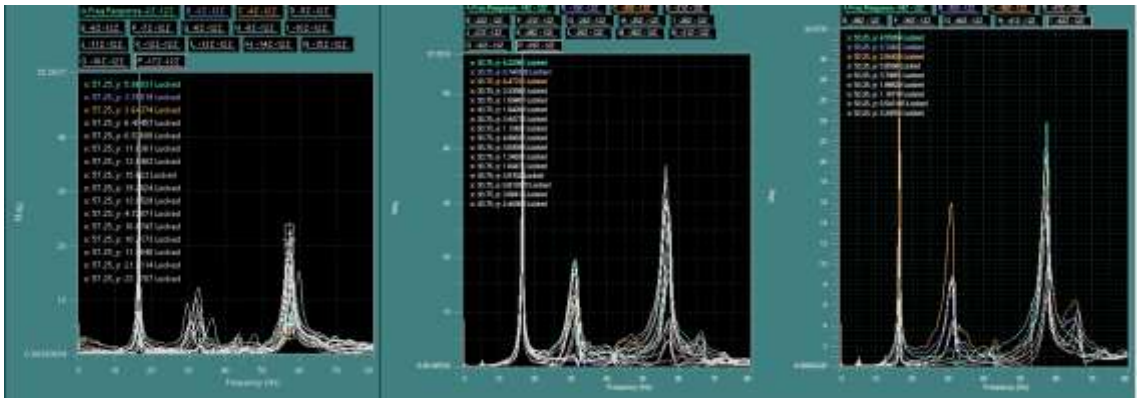

Figure 21 – FRFs of a full modal testing made in S1 before applying load.

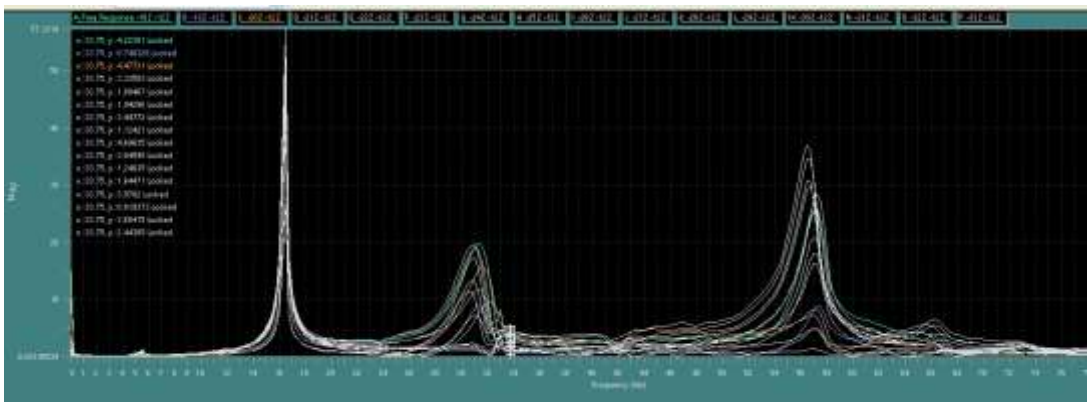

Figure 22 – Detail of FRFs of some points from S1 undamaged modal testing.

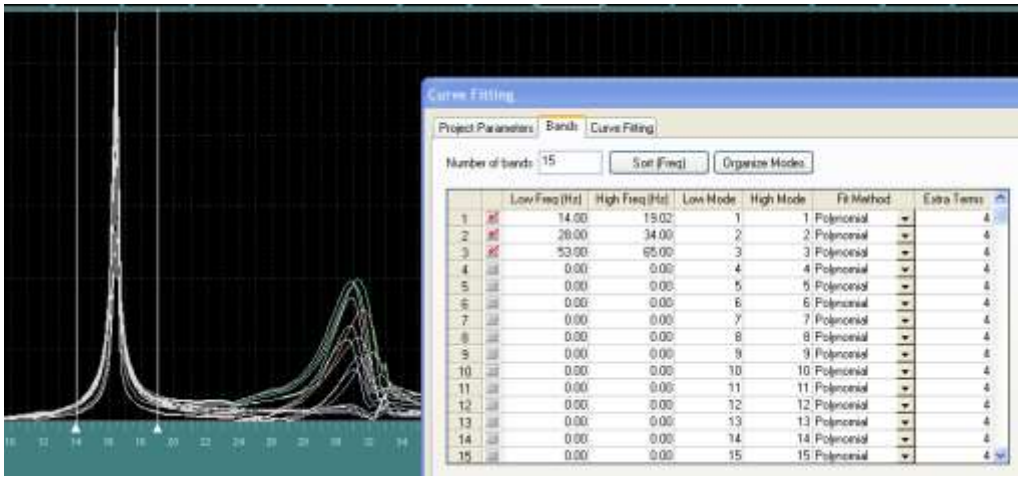

Figure 23 – Band definition for the three initial frequencies (detail of band isolating the first natural frequency).

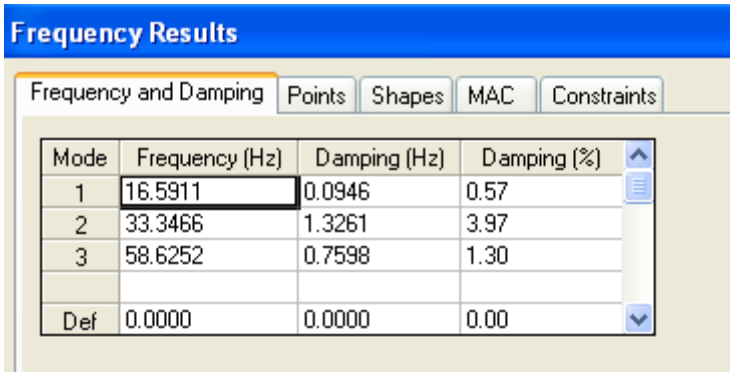

Figure 24 – Example of results of modal properties from curve fitting

Mode

1 - 16.59 | Add | Damping: 0.0946 | Hz: 0.57 | % | Scaling: Residues

Point	Dir 1 (Mag)	Dir 1 (Phase)	Dir 2 (Mag)	Dir 2 (Phase)	Dir 3 (Mag)	Dir 3 (Phase)
2	0.0000e+000	0.00	0.0000e+000	0.00	6.4266e+000	347.85
3	0.0000e+000	0.00	0.0000e+000	0.00	4.1927e+000	346.14
4	0.0000e+000	0.00	0.0000e+000	0.00	2.9311e+000	349.50
5	0.0000e+000	0.00	0.0000e+000	0.00	3.1864e+000	354.33
6	0.0000e+000	0.00	0.0000e+000	0.00	1.1220e+001	343.29
7	0.0000e+000	0.00	0.0000e+000	0.00	2.2385e+001	354.90
8	0.0000e+000	0.00	0.0000e+000	0.00	2.4932e+001	350.10
9	0.0000e+000	0.00	0.0000e+000	0.00	2.5138e+001	350.20
10	0.0000e+000	0.00	0.0000e+000	0.00	3.3497e+001	346.62
11	0.0000e+000	0.00	0.0000e+000	0.00	3.2983e+001	348.07

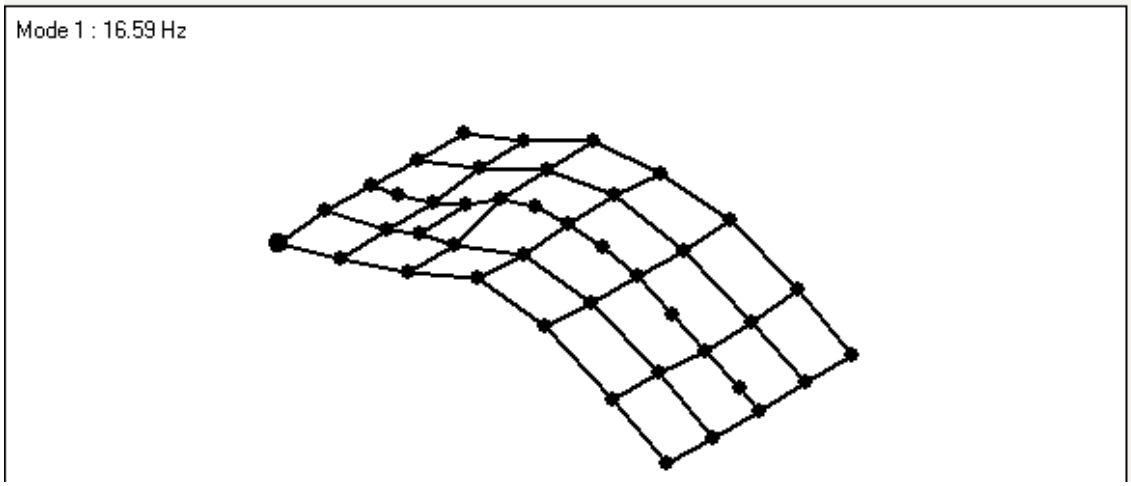

Figure 25 – Example of mode shape of the first natural frequency of S1 and its coordinates.

One of the results from modal testing is the angular coefficient of the signal along the decay, what will be called in this dissertation “gradient” of frequency along the decay. The responses in time domain were filtered, to isolate the component of response at the fundamental natural frequency of the tested slab. The band-pass filter employed was a basic application running in Matlab software. The isolation of the frequency component of interest was carried out in the frequency domain after applying a Fourier Transform to the time domain signal. An Inverse Fourier Transform returned the filtered time domain signal, and frequency spectra of the original and filtered signals were compared to assure the filtering procedure was successful. Then, the variation of the fundamental frequency along the decay of the signal after impact was obtained for each level of induced damage and is discussed in the results section. It should be mentioned that not all the data acquired during the modal tests were employed; this is just a general description of the whole test setup. Figure 26 shows a step-by-step procedure of gradient obtainment.

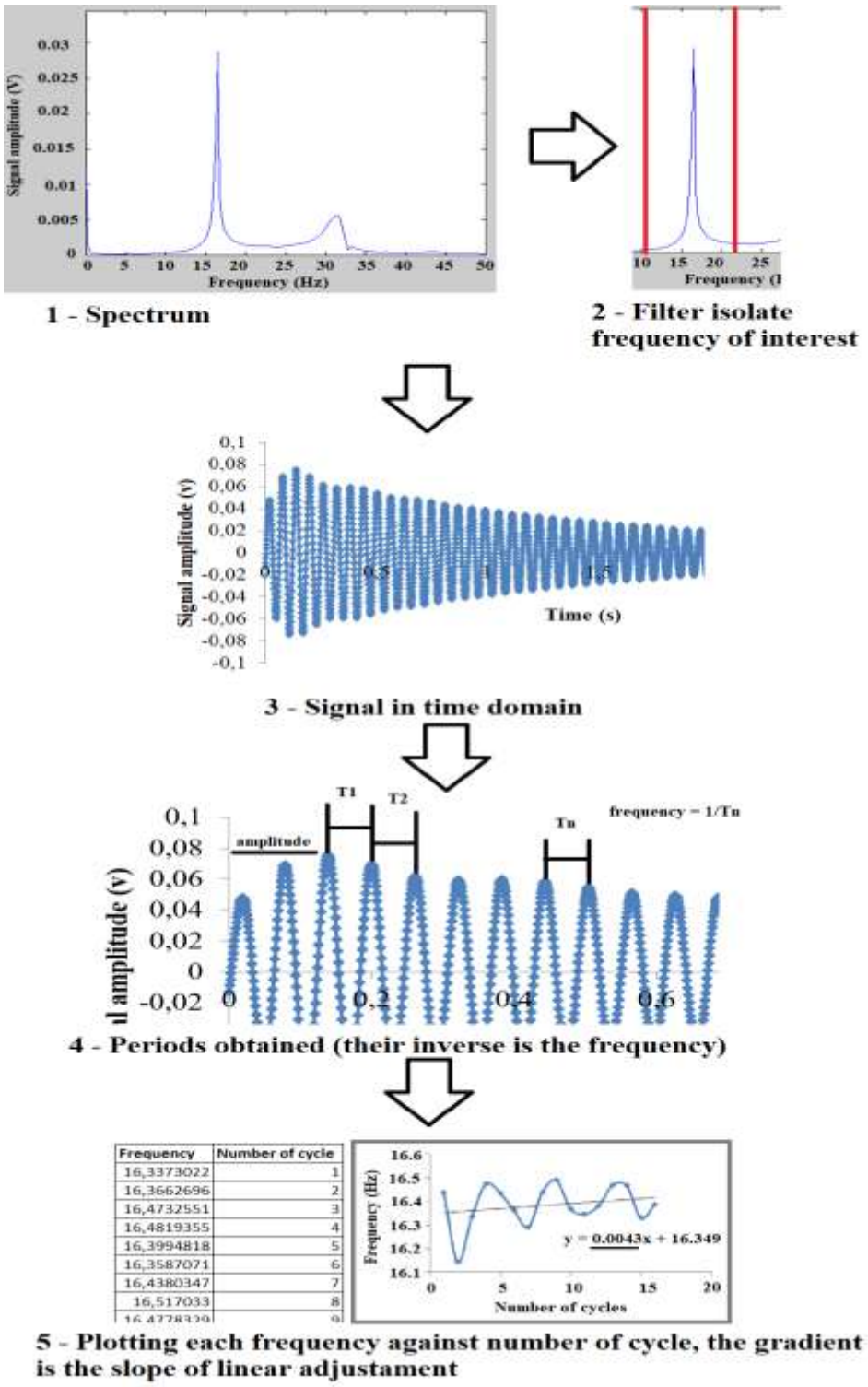

Figure 26 – Schematic representation of gradient obtainment.

From Figure 26 it can be seen that the filter applied is a vertical one used to isolate the frequency of intertest and, as result, the variation of signal along time (Figure 26, step 4) have an initial perturbation the the initial cycles (in the example, two cycles),

after what the sinal presents the expected decay. In other to investigate the influence of the adopted filter, two experiments were performed. In the first one, the adopted filter is applied on experimental data of an impact excitation and compared to Butterworth filters of different orders. The results are shown in Figure 27 and, knowing that the frequency band was from 16 Hz to 17 Hz, it is possible to observe that the original signal and the signal obtained with the adopted filter have the same amplitude in the frequency range of interest. The Butterworth filters had differenc in amplitude where, the higher the order of the filter, the lower the amplitude.

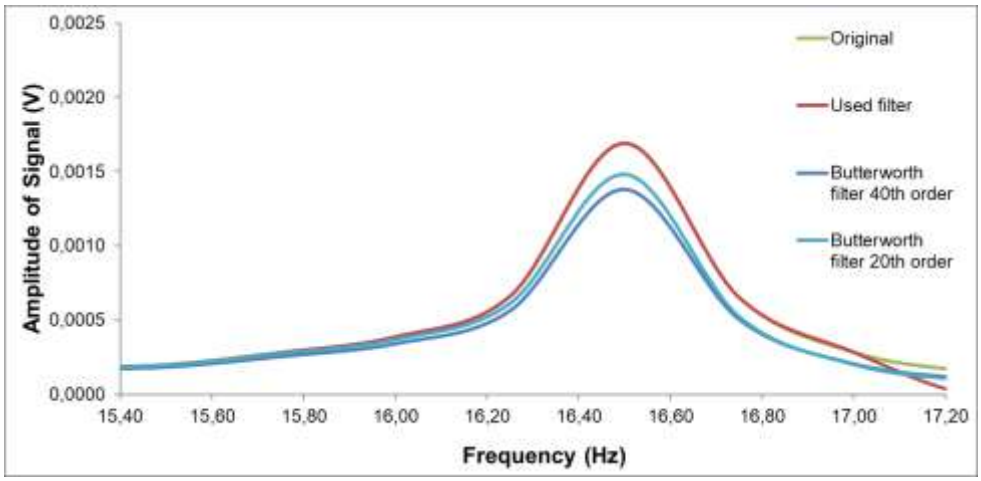

Figure 27 – Filters comparison in frequency domain signal.

The second experiment consisted in obtaining the gradient of a sine sweep signal, where the amplitude of a sine signal with 4096 points in four seconds had an increase of 0,1 Hz in each cycle (approximately 60 points). Comparing the initial cycles from the beginning (0.5 initial seconds) and the ending (0.5 final seconds), it is observed that both Butterworth filter and the adopted filter have a delay of half cycle but the adopted filter does not affect the amplitude of signal (Figures 28 and 29).

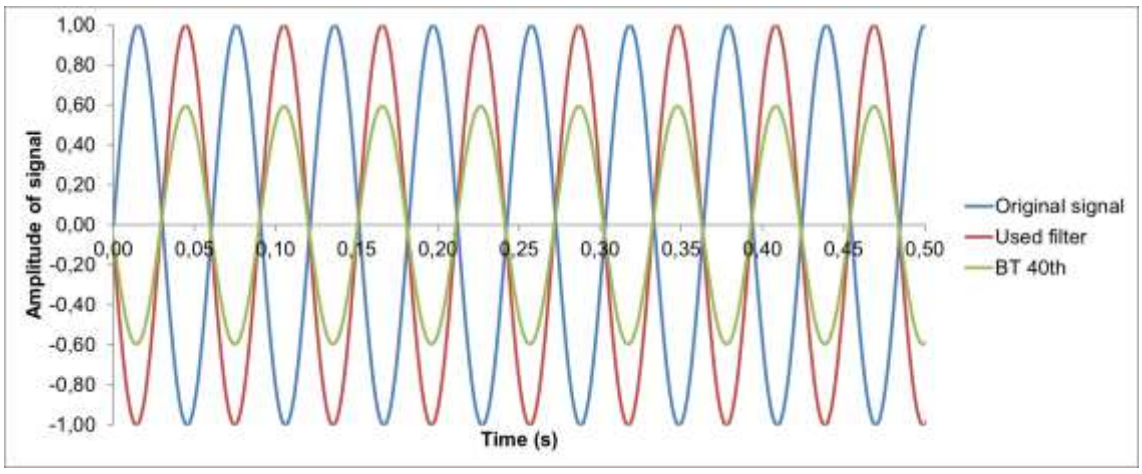

Figure 28 – Signal delay of different filters from 0 to 0.5 seconds.

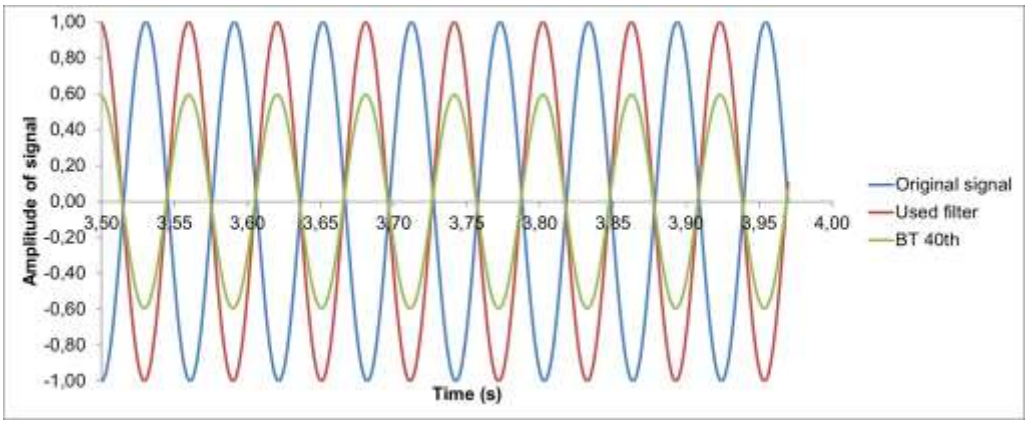

Figure 29 – Signal delay from 3.5 to 4.00 seconds.

The next test was obtaining the gradient of signals. Due the nature of sine-sweep signal, it is expected that the gradient have a linear behavior along the cycles. Taking the ten inicial cycles and comparing the gradient obtained from different signals (Figures 30 to 33), it is noticeable that the gradient of the original signal is equal to the one after applying the adopted filter . For the Butterworth filter, higher order of the filters produced gradients far from the ideal.

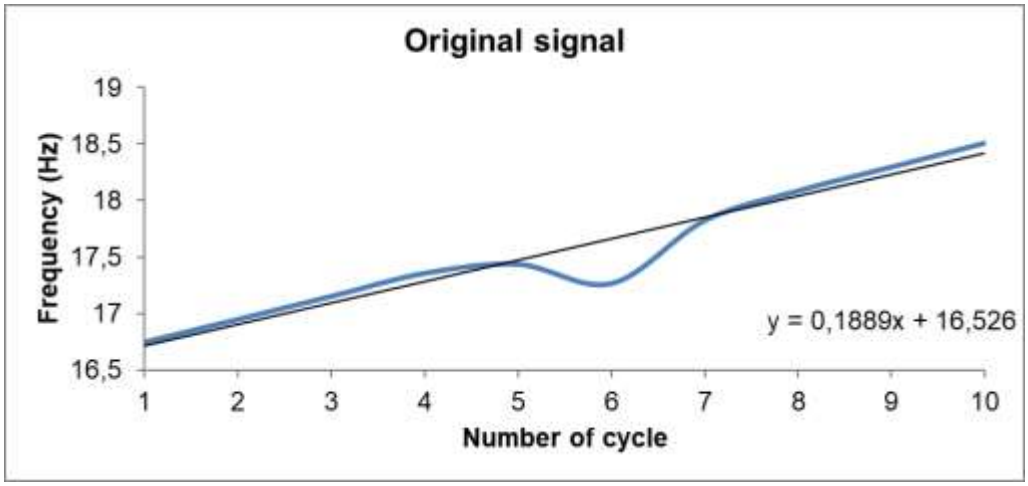

Figure 30 – Gradient obtained from original signal.

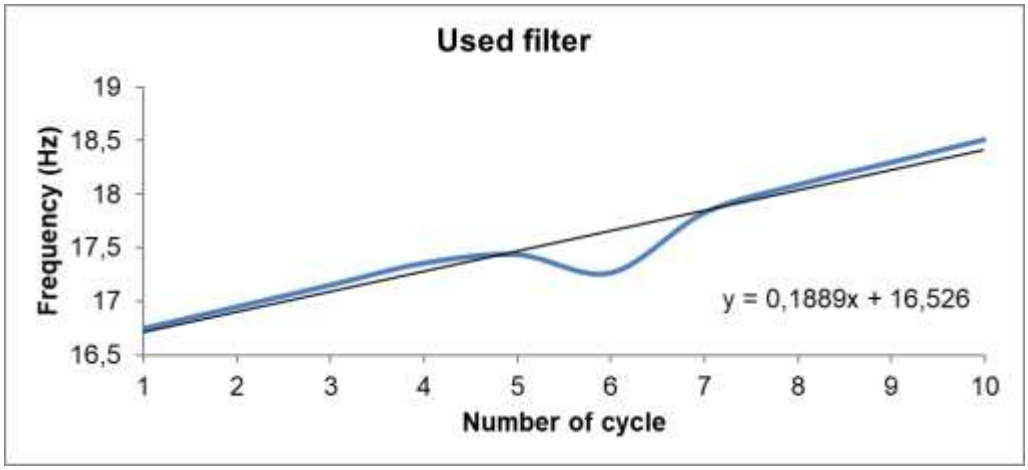

Figure 31 – Gradient obtained from the used filter signal: same gradiant of original signal.

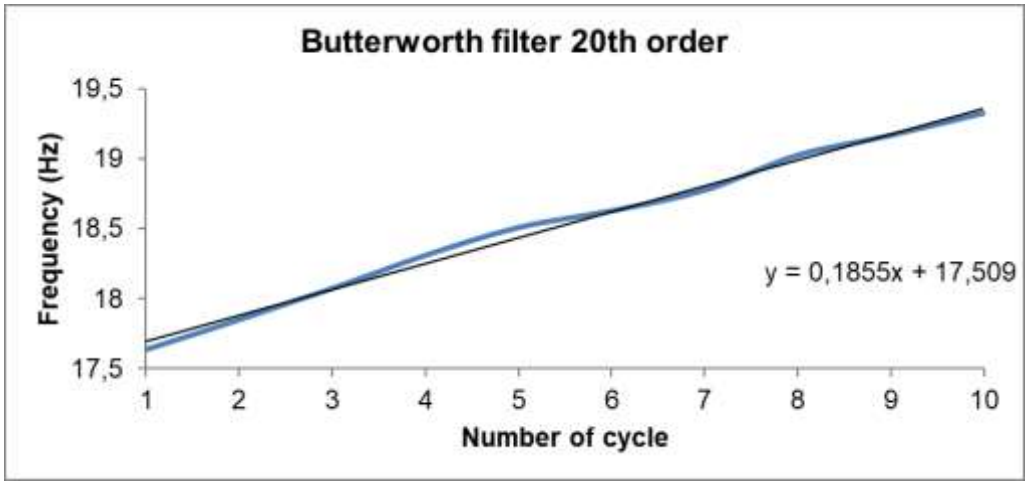

Figure 32 – Gradient obtained from a 20th order Butterworth filter.

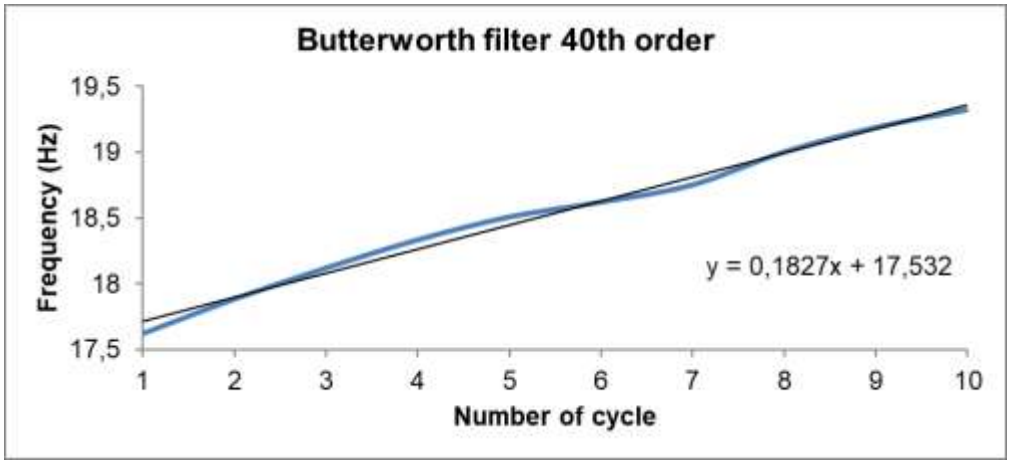

Figure 33 – Gradient obtained from a 40th order Butterworth filter.

Based on the tests made using different filters, it is possible to conclude that, alghough the used filter adds delay to the filtered signal, this delay does not affect the gradient obtainment. In addition, the adopted filter does not affect the signal amplitude. Therefore, the adopted filter is adequate to the use made in this research.

3.5. Numerical modelling

Considering the dimensions, the support condition and the loads applied in both slabs, the numerical model was made using the ANSYS software. The finite element employed was one the library of elements of the software, named SHELL63, a four node element with bending and membrane capabilities, with six degree of freedom at each node: translations in the nodal x, y, and z directions and rotations about the nodal x, y, and z-axes. The element is illustrated in Figure 34.

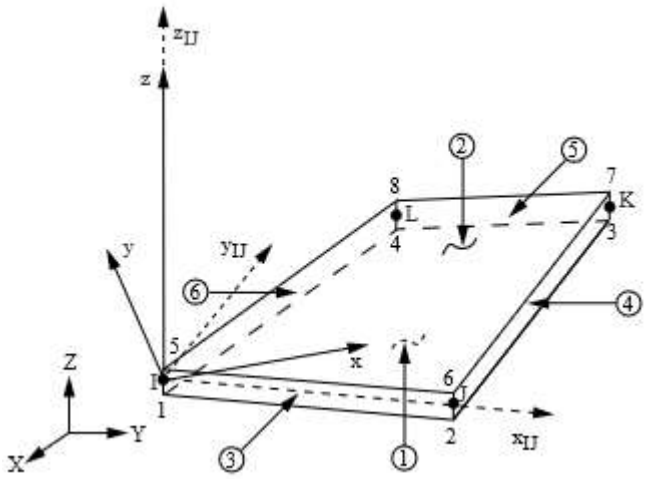

Figure 34 – Element SHELL62 (Source: ANSYS manual)

There were seventy-seven experimental nodes on S2 and, as it has a more dense experimental mesh, it was chosen as reference for start the modeling. When the numerical model was created, experimental nodes remained coincident to computer model nodes, and additional nodes were created between every two real (ie, experimental) nodes. In order to model the support conditions more properly, two coincident (in position) nodes at each experimental node at the supports were used, one restrained in all directions and the other (at the slab) free to move vertically. To connect both nodes, a COMBIN14 element was used. COMBIN14 is a longitudinal spring-

damper connected by two nodes with also torsion capabilities (that were not used), as illustrated in Figure 35.

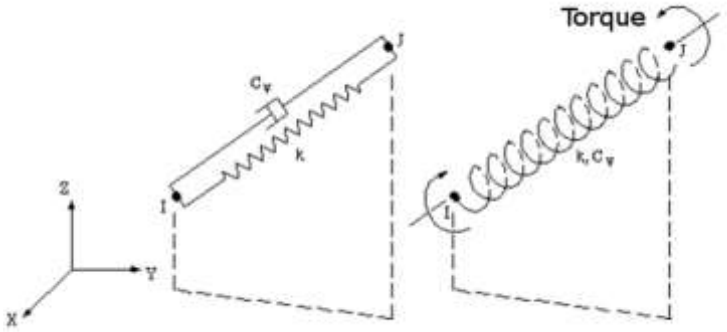

Figure 35 – COMBIN14 element (Source: ANSYS manual)

To define the spring constant of the support nodes, the results of modal testing were employed. First, the mode shape of each natural frequency extracted from modal testing were plotted in vector mode, as shown in Figure 36. The modal displacement of each node along the support was obtained and divided by the maximum nodal value in order to obtain a relative absolute value. The next step was the use linear interpolation for the numerical nodes as shown in Figure 37. In the numerical model each node at the support line has a spring-damper element COMBIN14 where the spring coefficient is adjusted using the data from modal testing. An illustration of the slab with the COMBIN14 elements used at the supports nodes is shown in Figure 38.

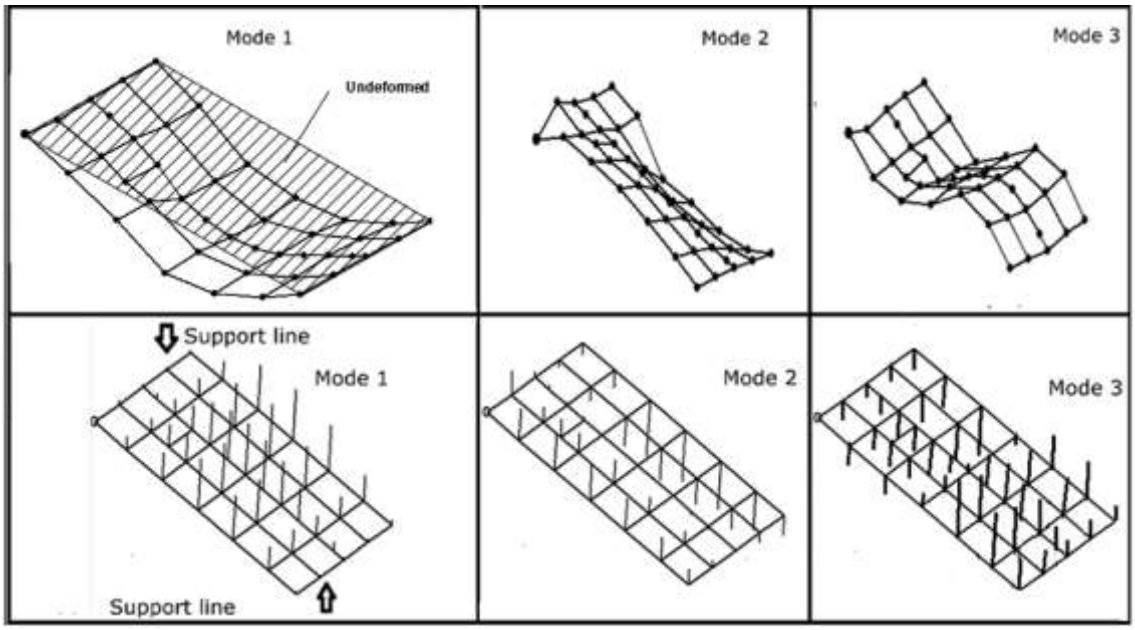

Figure 36 – Mode shape of each frequency (on top) and its correspondent vectorial form (bottom)

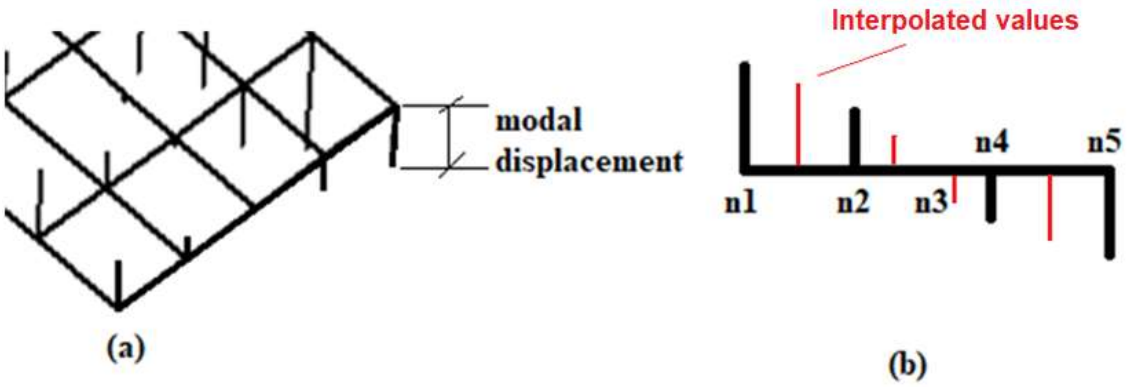

Figure 37 – Modal displacement at support nodes used for COMBIN14 stiffness adjust.

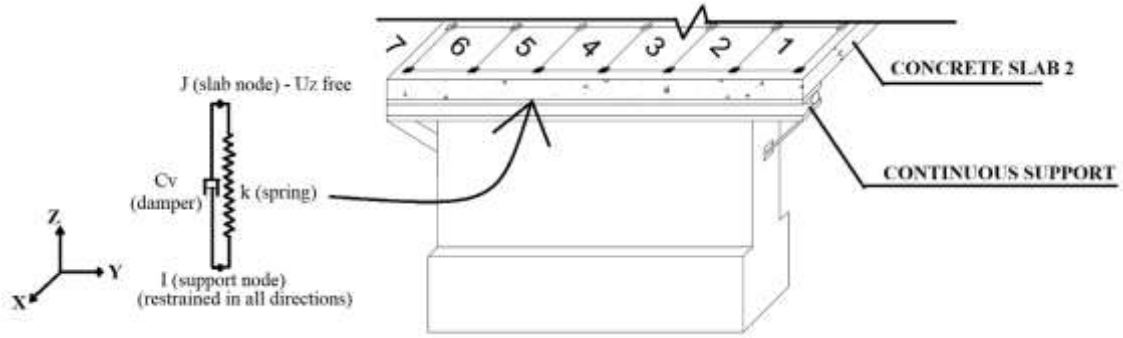

Figure 38 – Scheme of COMBIN14 nodes used at support line.

Regarding the material properties, according to NBR 6118/2014 and ACI 318/95, the secant modulus of concrete (Esc) is related to the initial tangent modulus (Ec) by two expressions

$$E_{SC} = 0.85 * E_C \quad (4)$$

$$E_{SC} = 4730\sqrt{f_{ck}},\ \text{MPa} \quad (5)$$

Combining equations (4) and (5), the result is:

$$E_C = 5565\sqrt{f_{ck}},\ \text{MPa} \quad (6)$$

In Brazilian standard NBR 6118/2014, the coefficient of Equation (6) is 5600 (the value 5565 is used in ACI 318/95) and it was the expression used to calculate the elastic module of concrete used in the numerical model (5600 as the coefficient). The

elastic tangent modulus E_c is the tangent at the beginning of a stress-strain curve, as shown in Figure 39. Similarly, the secant modulus of elasticity E_{sc} represents the slope of a line passing through the origin of the diagram and intercepting it at a stress of about 0.4 f_C, where f_C is the compression strength.

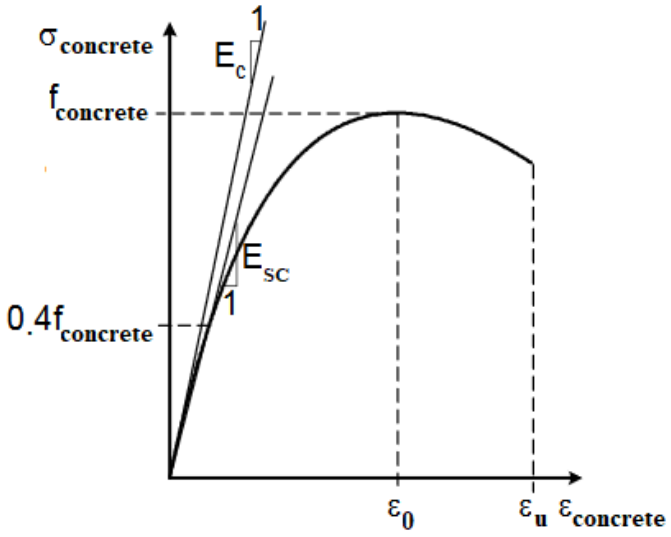

Figure 39 – Stress-strain diagram of concrete

During modal testing, the Young's module of concrete can increase until 40% as a dynamic effect (Metha, 1994), this being confirmed by other authors (Alves et al, 2011). As a result, the initial Young's module of each slab was calculated using Equation 6 but was tested for values increasing until 40% of the value obtained from the equation and the concrete streght used was the average resistance to compression f_{cj} instead of f_{ck}. Furthermore, the spring constant of supports were tested for different values but respecting the proportions of modal displacement from the tests, starting at 10^5 N/m² until 1^{15} N/m², the latter being an extreme value where there were no changes in the three natural frequencies evaluated, meaning a rigid support condition.

By dividing the values of frequencies obtained from the numerical model by the experimental ones (taken as reference values), the results for both slabs was surfaces of adjustment with Young's module and spring constant in X-Y plane and the ratio of frequencies in Z plane. For each spring constant adjusted at the nodes of support line (based in the first, second or third mode shapes) and respecting the proportions found for that adjustment, a corresponding model was created and the three first frequencies were obtained. Following the proportion of each adjustment, the spring constant of

COMBIN14 element is evaluated for different values and for a fixed elastic module of croncrete. The best adjust was in the line where the ratio was equal to 1, which means that the experimental frequency was equal to the numerical one. The 3D surfaces and their respective superior view for both slabs are shown in Figures 33 to 57. For S1, due to small values of modal displacement of this mode along the support nodes, the adjustment could not be done. For this slab, the best adjustment was obtained using the second mode shape, the same being observed for S2. The best adjust in frequency was also observed for the maximum value of elastic module (40% higher than the calculated by Eq. 6). This adjustment of support conditions was made in both slabs for the uncracked stage and the spring constants remained unchanged for the following load levels.

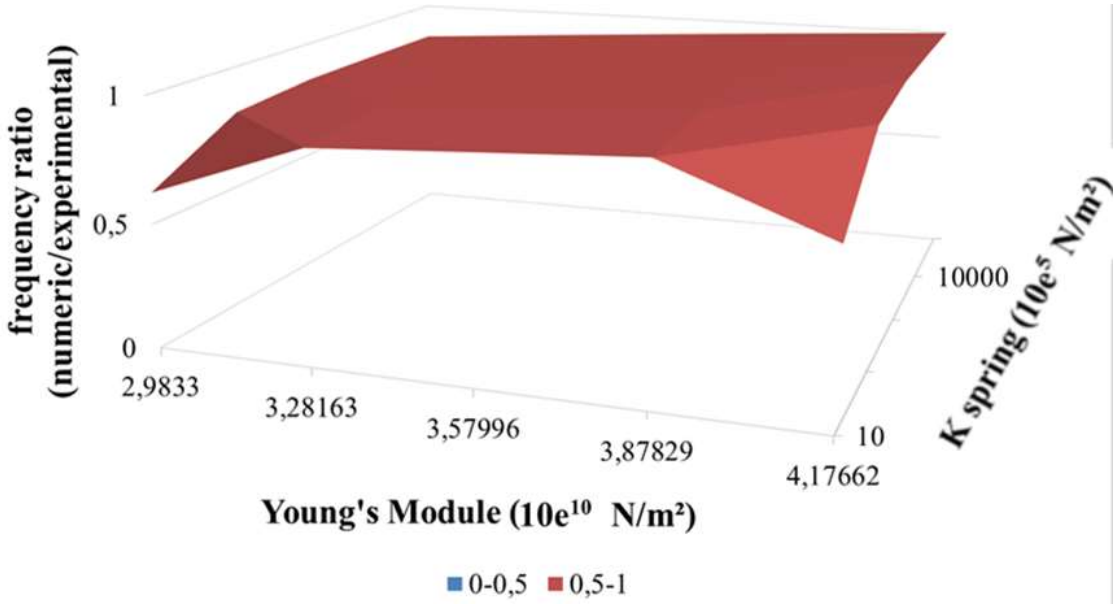

Figure 40 – S1 surface adjust of 1st natural frequency using 2nd mode shape.

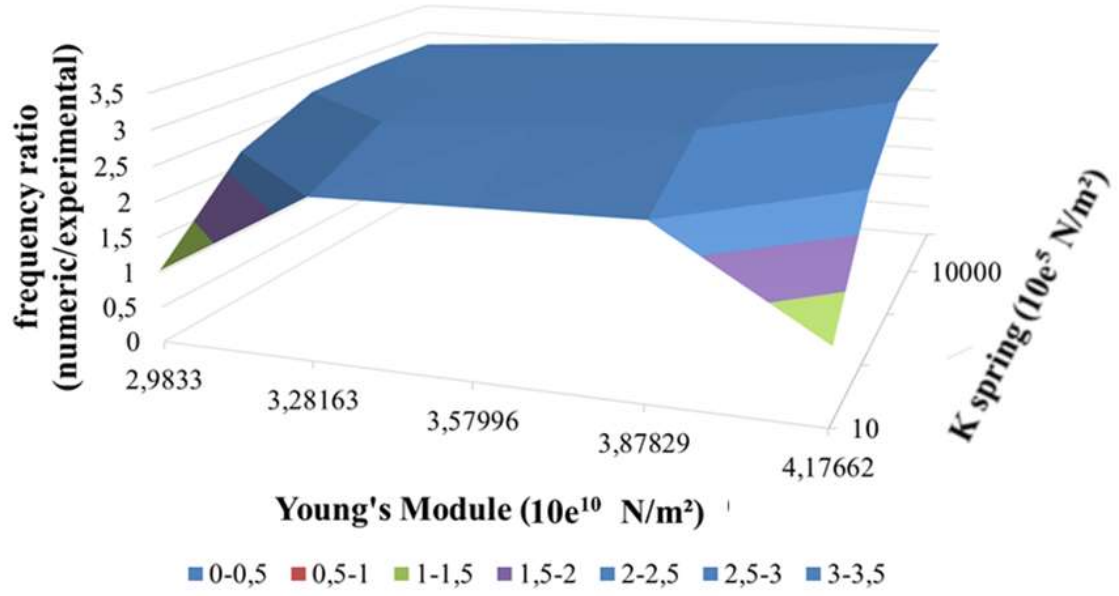

Figure 41 – S1 surface adjust of 2nd natural frequency using 2nd mode shape.

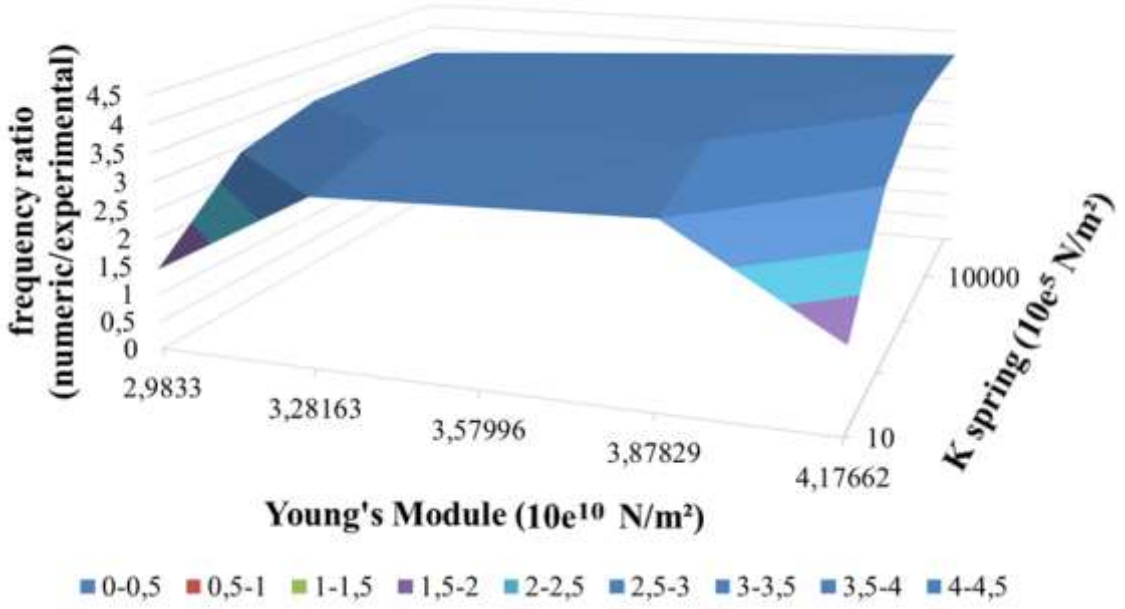

Figure 42 – S1 surface adjust of 3rd natural frequency using 2nd mode shape.

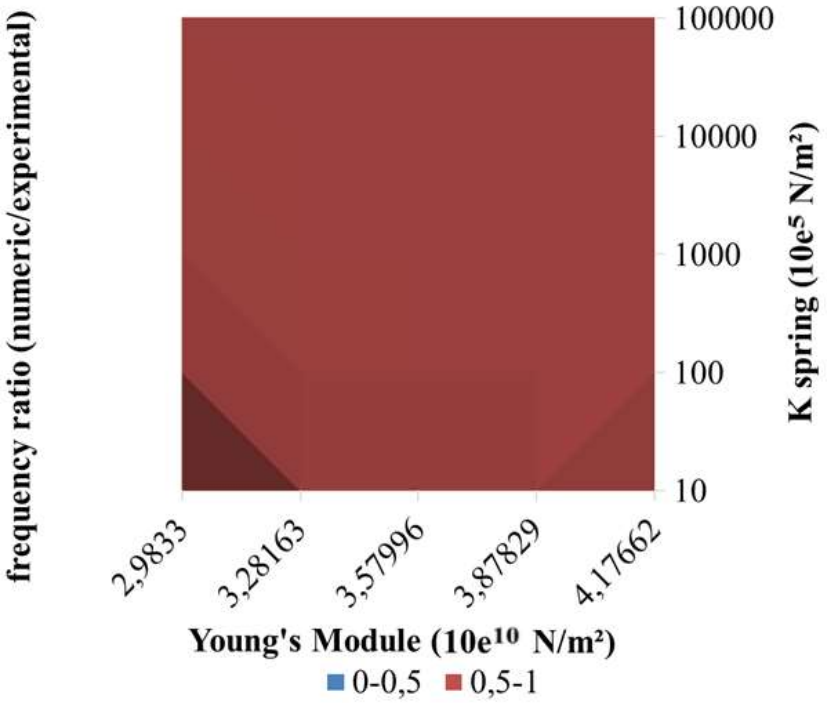

Figure 43 – S1 surface adjust of 1st natural frequency using 2nd mode shape.

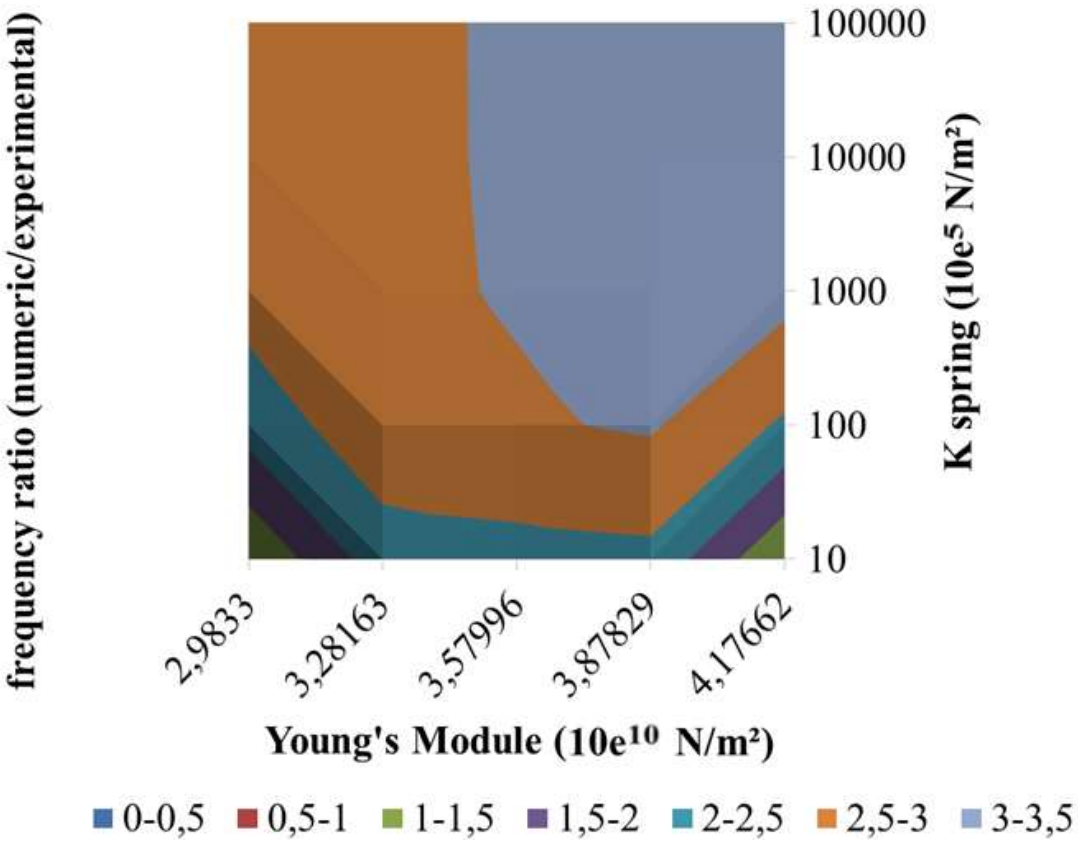

Figure 44 – S1 surface adjust of 2nd natural frequency using 2nd mode shape.

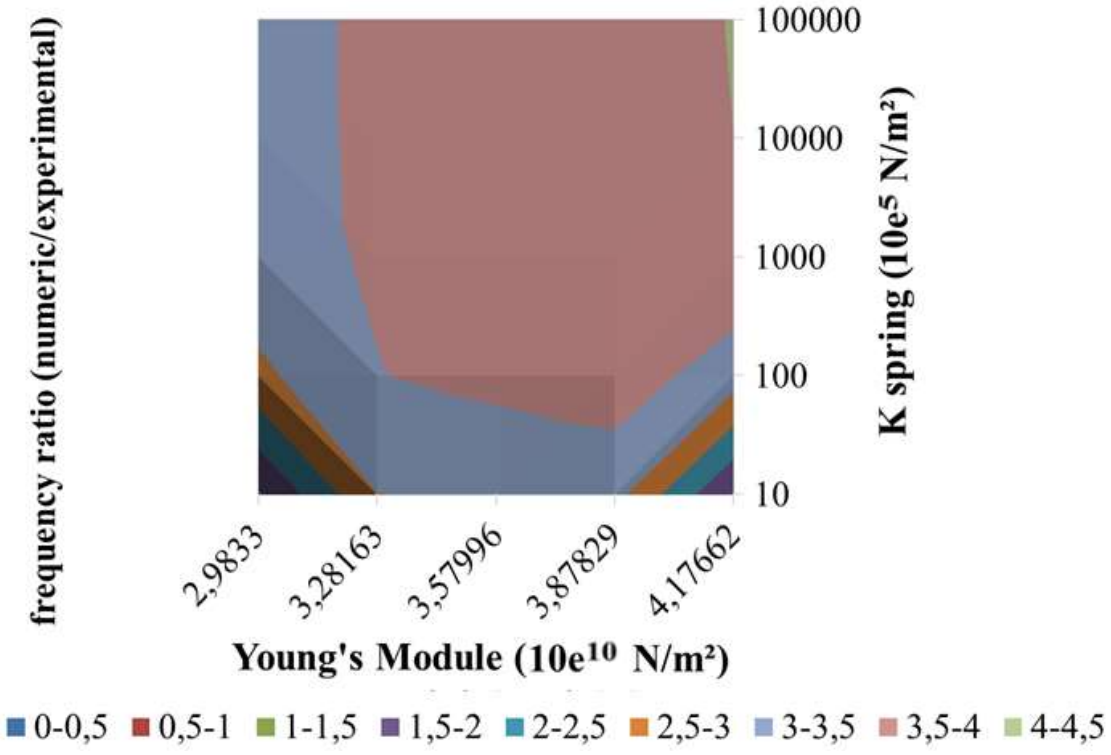

Figure 45 – S1 surface adjust of 3rd natural frequency using 2nd mode shape.

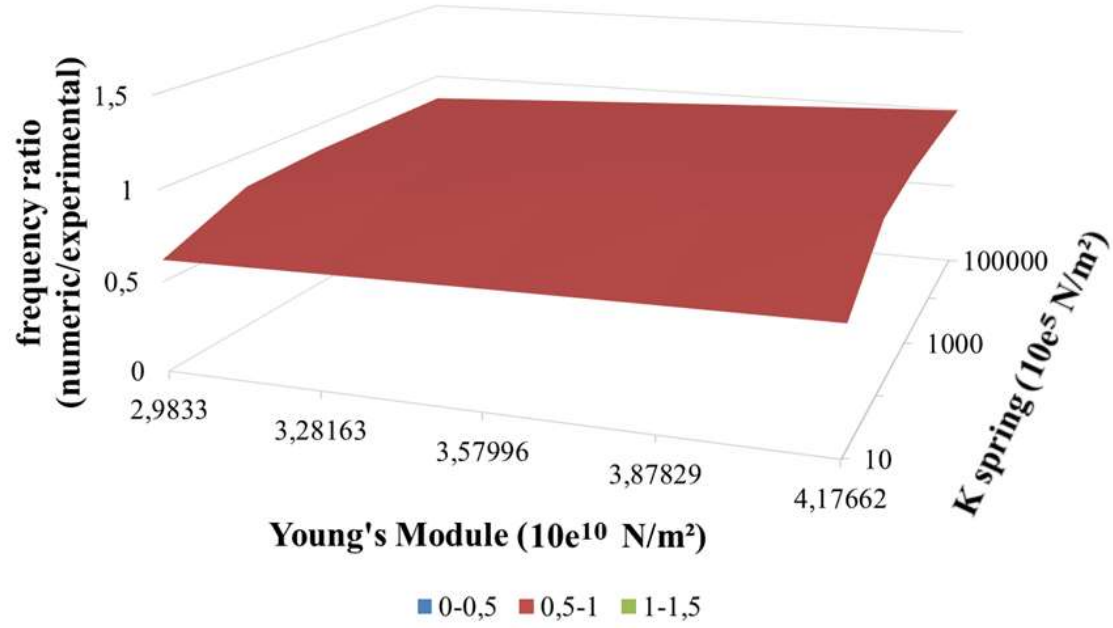

Figure 46 – S1 surface adjust of 1st natural frequency using 3rd mode shape.

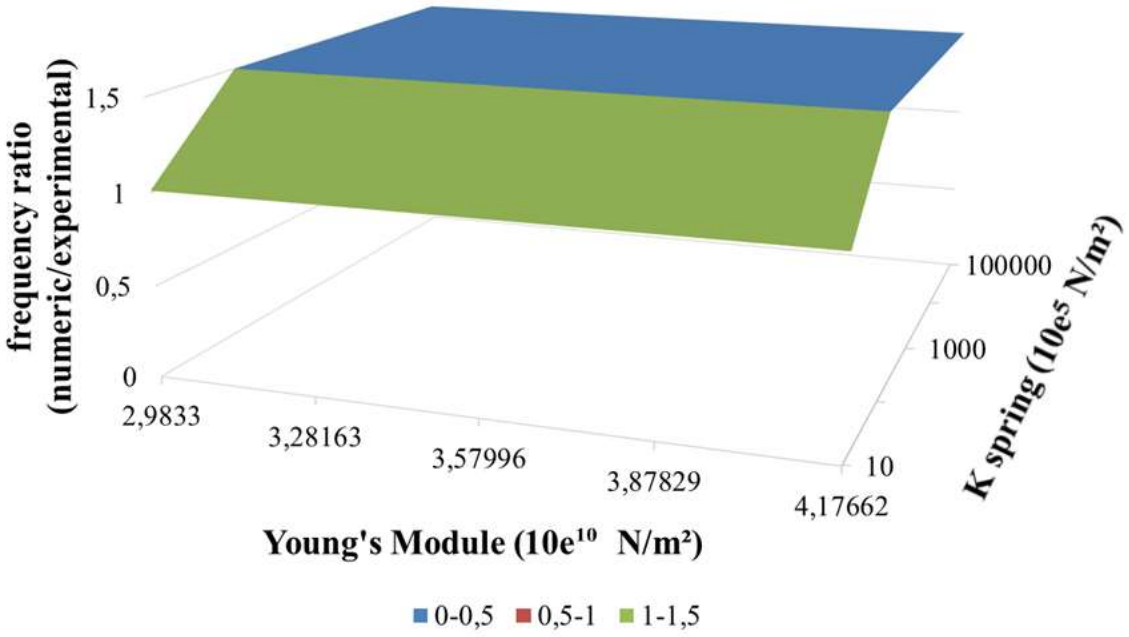

Figure 47 – S1 surface adjust of 2nd natural frequency using 3rd mode shape.

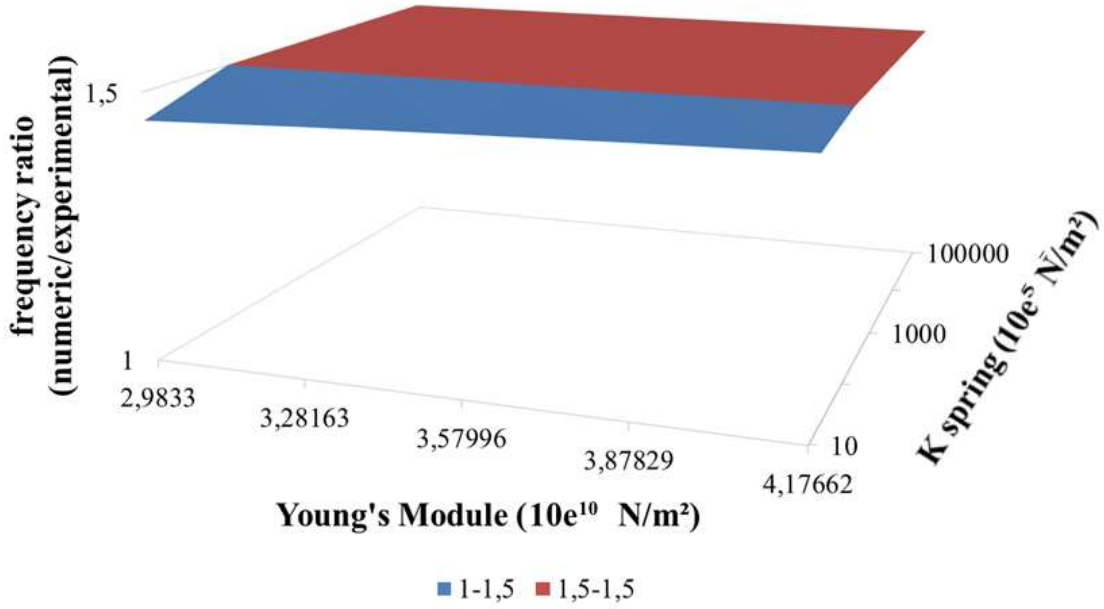

Figure 48 – S1 surface adjust of 3rd natural frequency using 3rd mode shape.

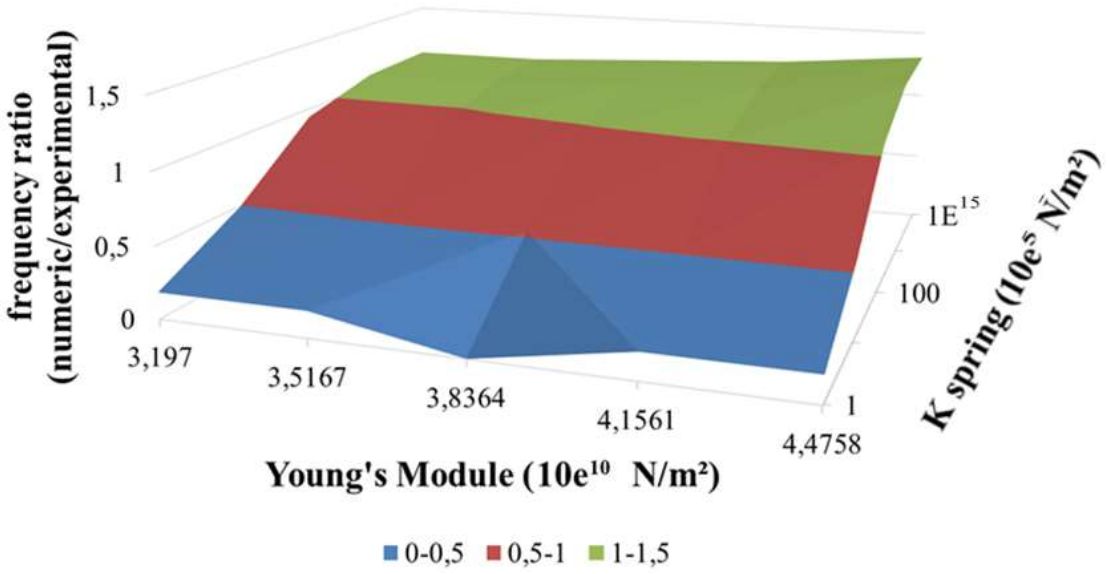

Figure 49 – S2 surface adjust of 1st natural frequency using 1st mode shape.

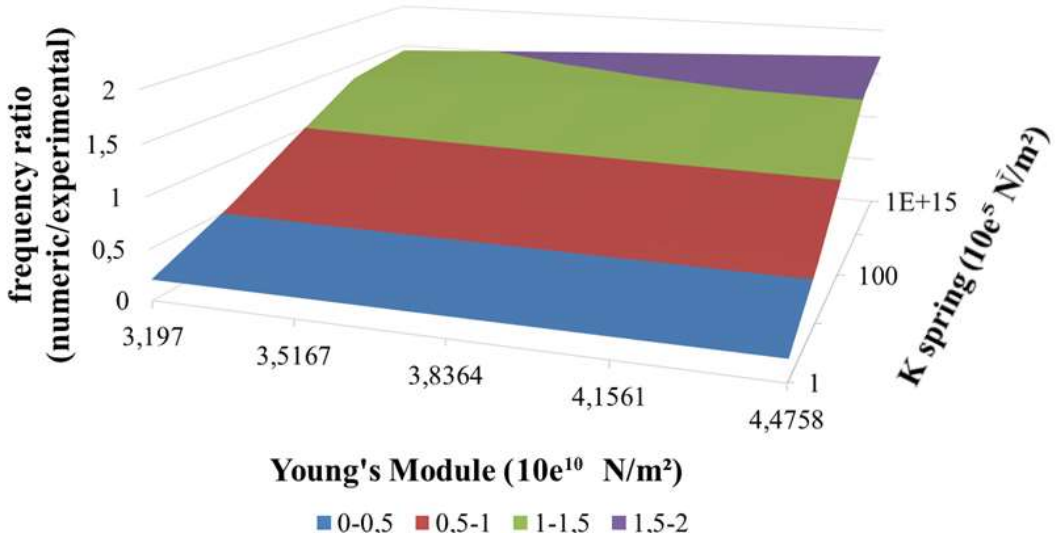

Figure 50 – S2 surface adjust of 2nd natural frequency using 1st mode shape.

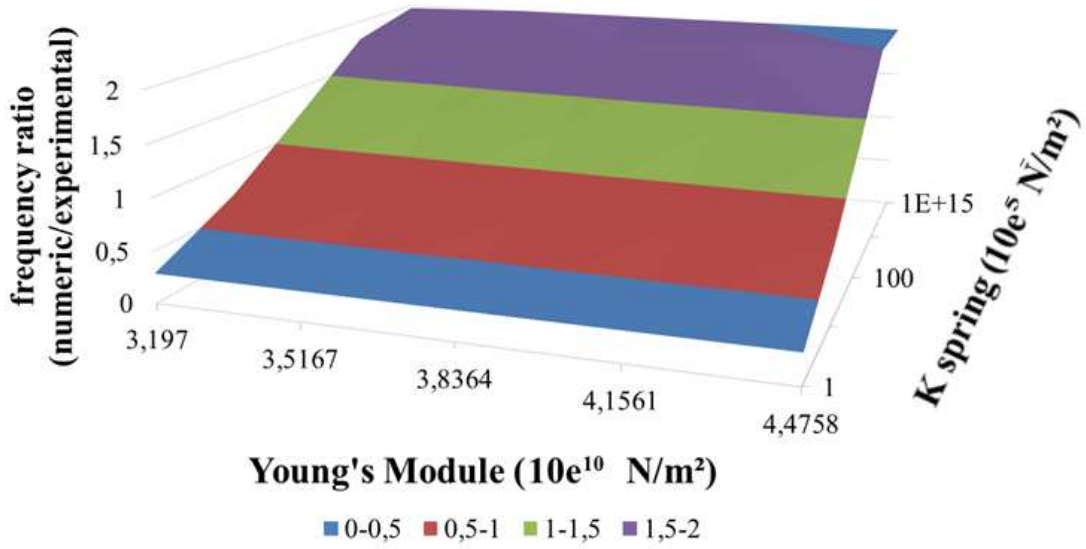

Figure 51 – S2 surface adjust of 3rd natural frequency using 1st mode shape.

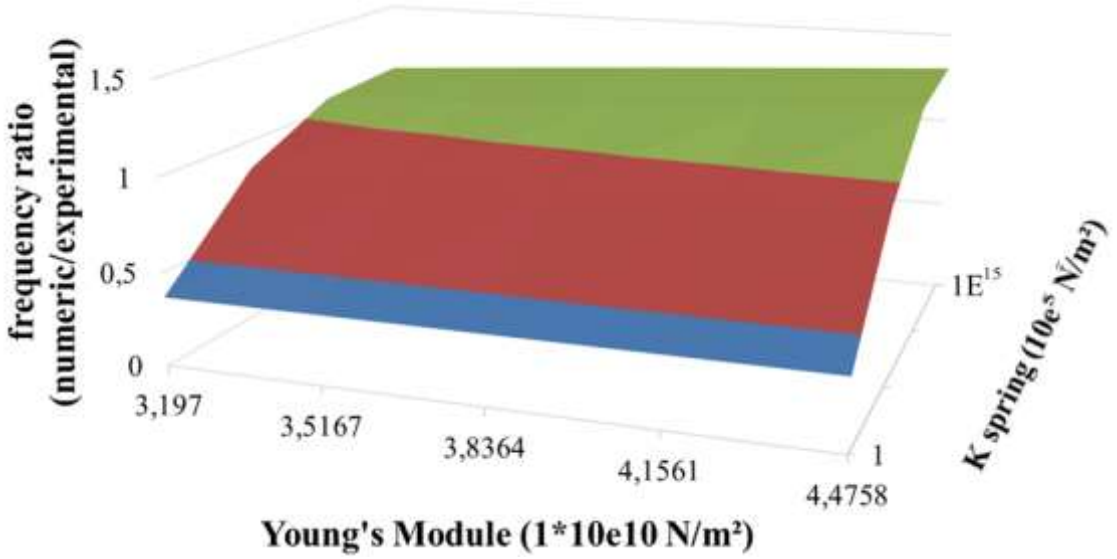

Figure 52 – S2 surface adjust of 1st natural frequency using 2nd mode shape.

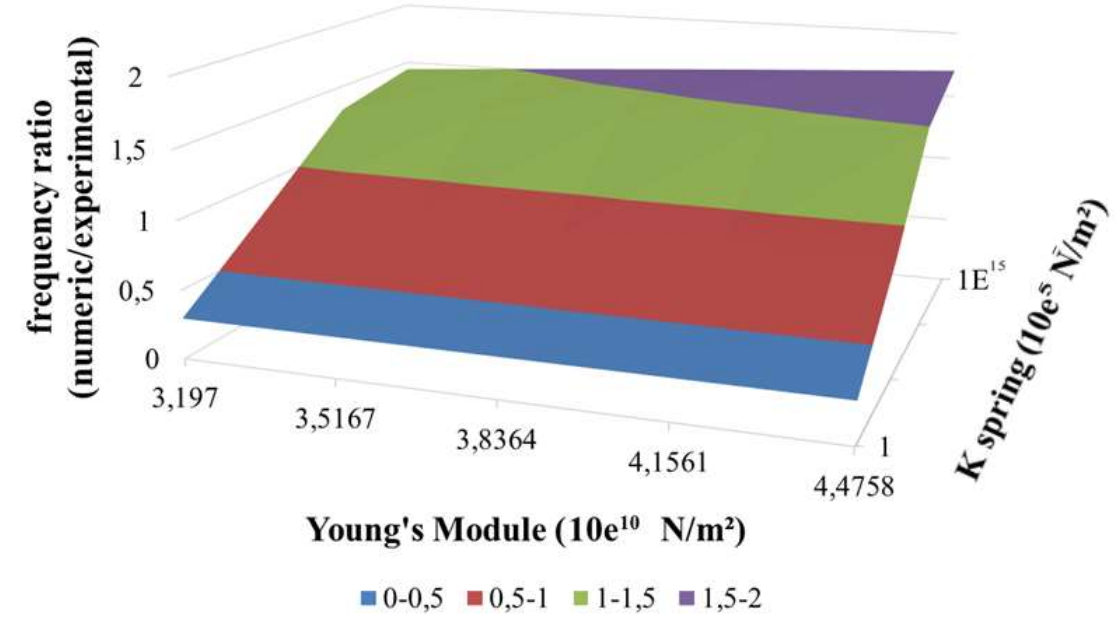

Figure 53 – S2 surface adjust of 2nd natural frequency using 2nd mode shape.

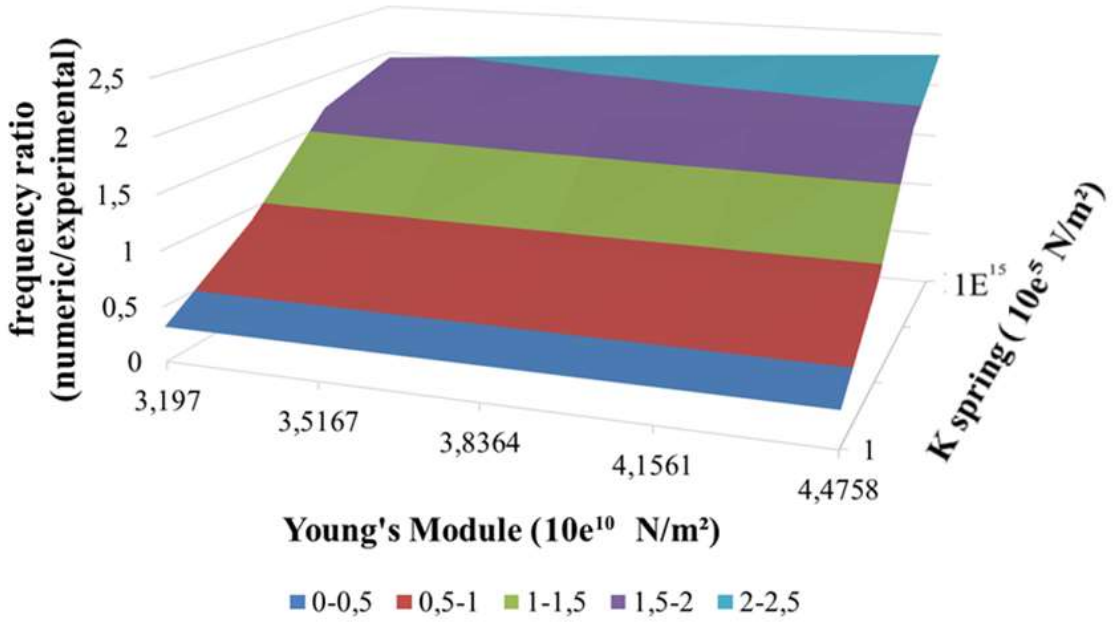

Figure 54 – S2 surface adjust of 3rd natural frequency using 2nd mode shape.

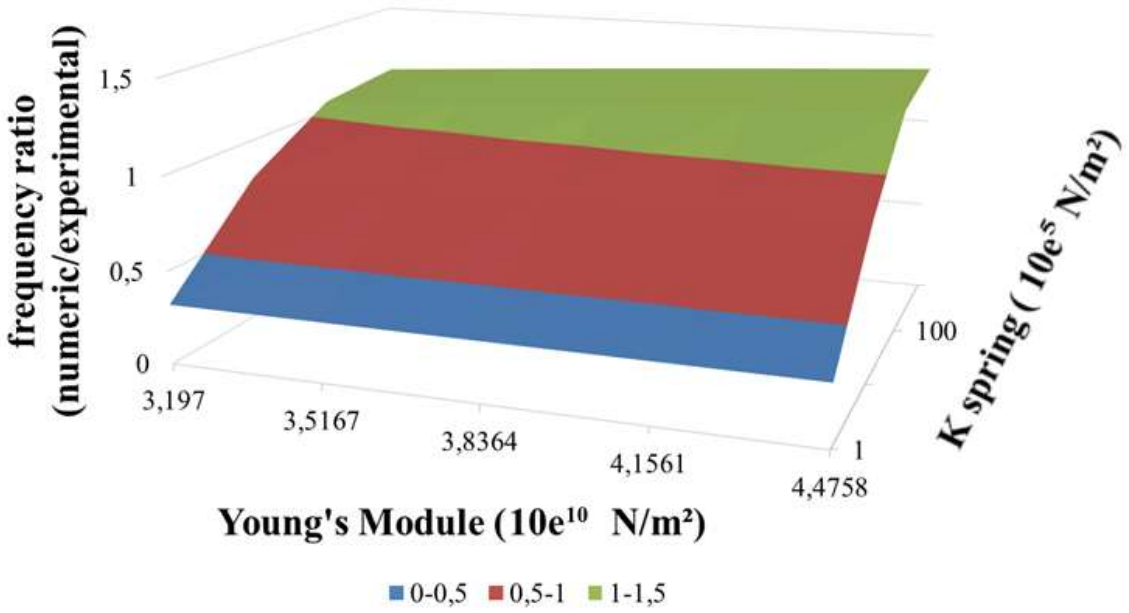

Figure 55 – S2 surface adjust of 1st natural frequency using 3rd mode shape.

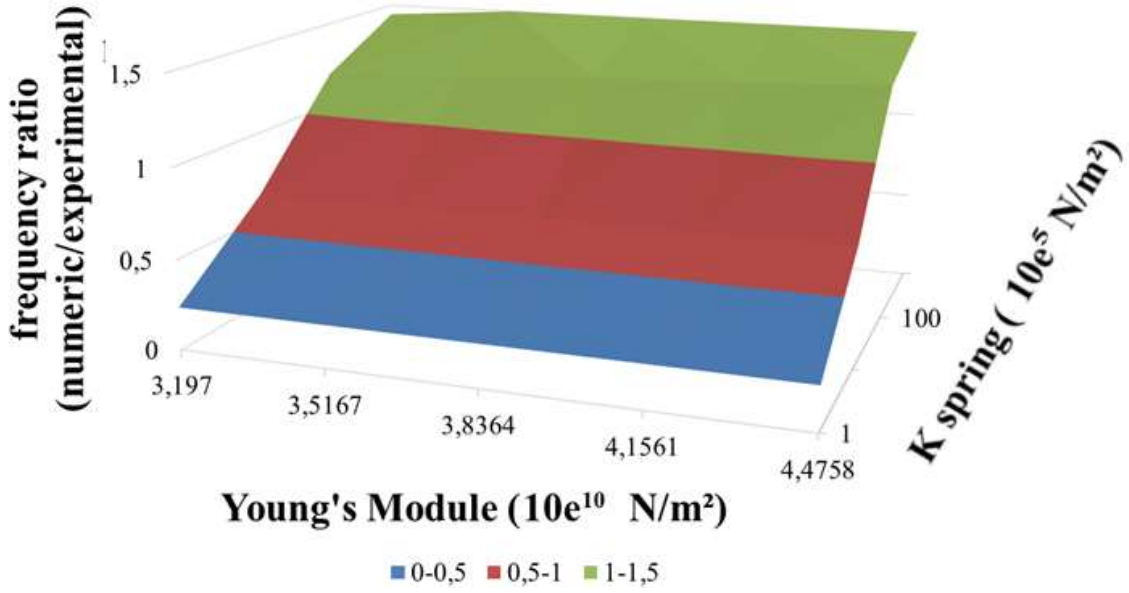

Figure 56 – S2 surface adjust of 2nd natural frequency using 3rd mode shape.

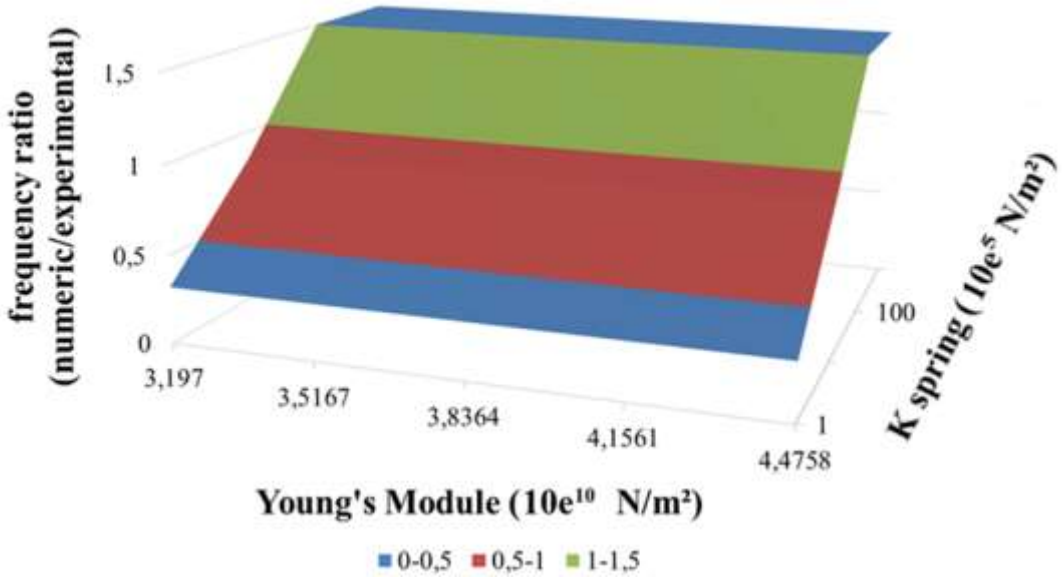

Figure 57 – S2 surface adjust of 3rd natural frequency using 3rd mode shape.

The adjusts seeking the best fitting considered two aspects: the difference of frequency values and the mode shapes from the reference ones (that is, experimental values). To evaluate the mode shape at the supports, the COMAC between the numerical and experimental values were compared in order to first identify problematic nodes (for which the experimental values did not seem reliable) and remove them from data set. In Tables 3 and 4, it is possible to see that the COMAC had poor values for node 73 considering the excitation at both driving points 18 and 62. After the final verification, the spring constants of both slabs supports were considered to remain constant until the collapse and the changes on frequency were obtained through changes in the Young's module of concrete. It must be mentioned that other support node conditions are available in the literature, as shown in the research of Freitas (2019).

COMAC VALUES - S2 - EXCITATION AT POINT 62					
	NODE	**COMAC**		**NODE**	**COMAC**
FRONT SUPPORT NODES	**1**	0,9686	BACK SUPPORT NODES	**71**	0,7643
	2	0,8822		**72**	0,4340
	3	0,6079		**73**	**0,0099**
	4	0,5162		**74**	0,2603
	5	0,6165		**75**	0,5950
	6	0,3141		**76**	0,7701
	7	0,6232		**77**	0,8521

Table 3 – COMAC values for S2 support nodes for excitation at node 62

COMAC VALUES - S2 - EXCITATION AT POINT 18					
	NODE	**COMAC**		**NODE**	**COMAC**
FRONT SUPPORT NODES	**1**	0,633799	BACK SUPPORT NODES	**71**	0,895816
	2	0,671302		**72**	0,737826
	3	0,22148		**73**	**0,05**
	4	0,515105		**74**	0,44449
	5	0,541705		**75**	0,285479
	6	0,525643		**76**	0,802916
	7	0,82411		**77**	0,930627

Table 4 – COMAC values for S2 support nodes for excitation at node 18

Once the spring constants of the support nodes were defined in each slab, the next step was a choice of numerical mesh. For the definition of the final computer model, an initial analysis was made evaluating the nodal displacement of both slabs for unitary load lines in the same position of the experimental setup (1/3 and 2/3 of main span). The comparison was made between the results from the numerical model with a mesh identical to the experimental mesh and a refined version (where the number of divisions in each edge was doubled). The displacement of nodes in the central line along the width of the slab is shown in Figure 58 for S1 with a "experimental" mesh and Figure 59 for S1 with a refined mesh.

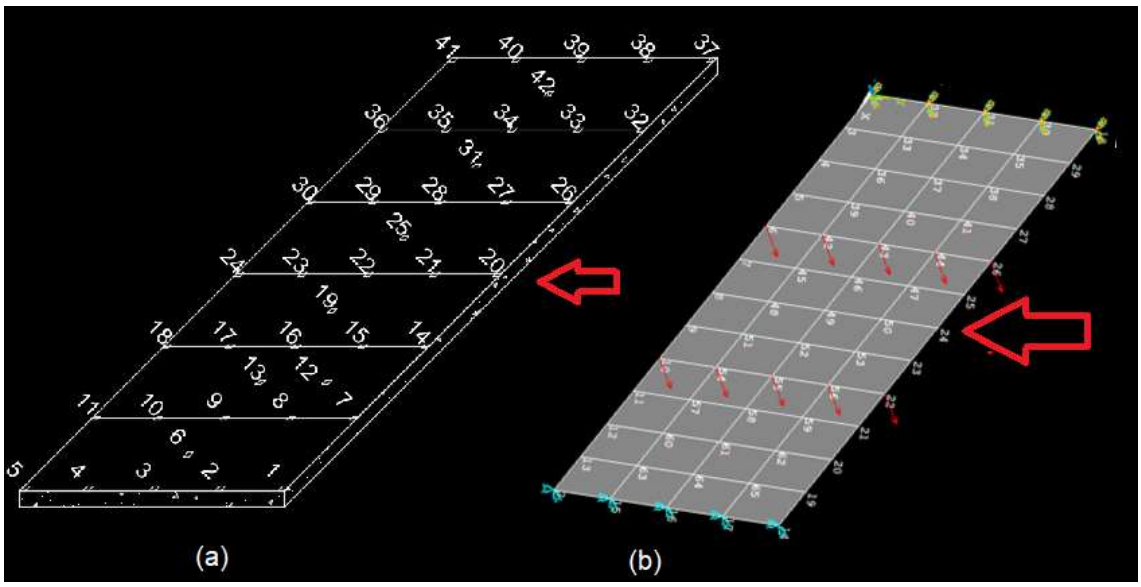

Figure 58 – S1 experimental model in (a) CAD version and (b) numerical analysis software with unitary load line and displacement measured at central node line (arrow highlights the central line).

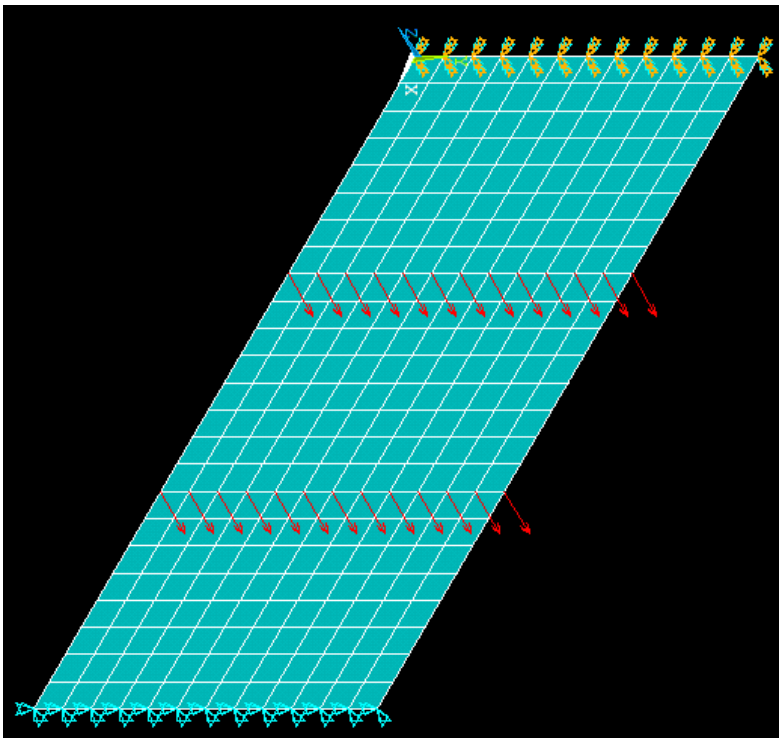

Figure 59 – S1 refined numerical model with unitary load line.

After model refinement, nodal displacements can be numerically evaluated to compare their changes. Figures 60 and 61 shows equivalent nodes (from the top to down direction). Comparing equivalent nodes from gross mesh to the refined mesh used (for example, nodes 8 in gross to node 14 in refined, node 49 in gross mesh to node 199 in the refined), it it is observed the the maximum difference in displacement is less the 0.3%. Although the evaluation of the model adequacy could have been made using experimental nodal displacements, there are some limitations. The first is that there are a low number of LVDTs available: only one was used in S1 and despite the fact that two where used in S2, only one was in fact trustful in the tests. The second is that the numerical model was created for an unloading situation while the real structures are subjected to several loading and unloading stages. Based on these facts, the evaluation of mesh refinement was based in frequencies and mode shapes (through MAC index), as will be discussed later on. The evaluation of adequacy of the model based on unloading condition for the loading condition is also discussed in results section.

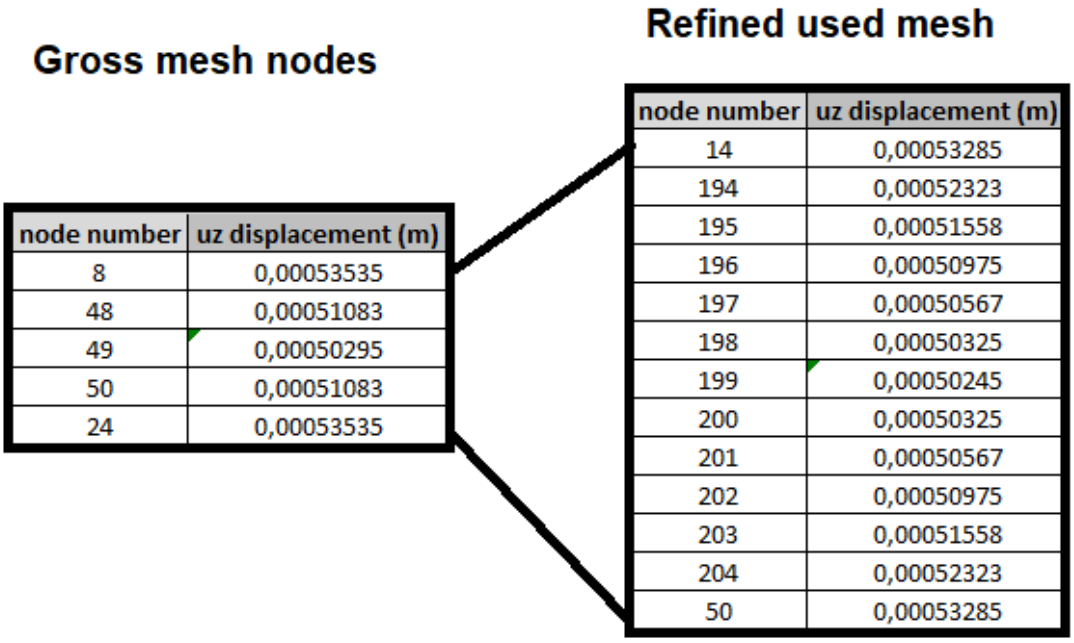

node number	uz displacement (m)
8	0,00053535
48	0,00051083
49	0,00050295
50	0,00051083
24	0,00053535

node number	uz displacement (m)
14	0,00053285
194	0,00052323
195	0,00051558
196	0,00050975
197	0,00050567
198	0,00050325
199	0,00050245
200	0,00050325
201	0,00050567
202	0,00050975
203	0,00051558
204	0,00052323
50	0,00053285

Figure 60 – S1 comparison of nodal displacement for unitary load line.

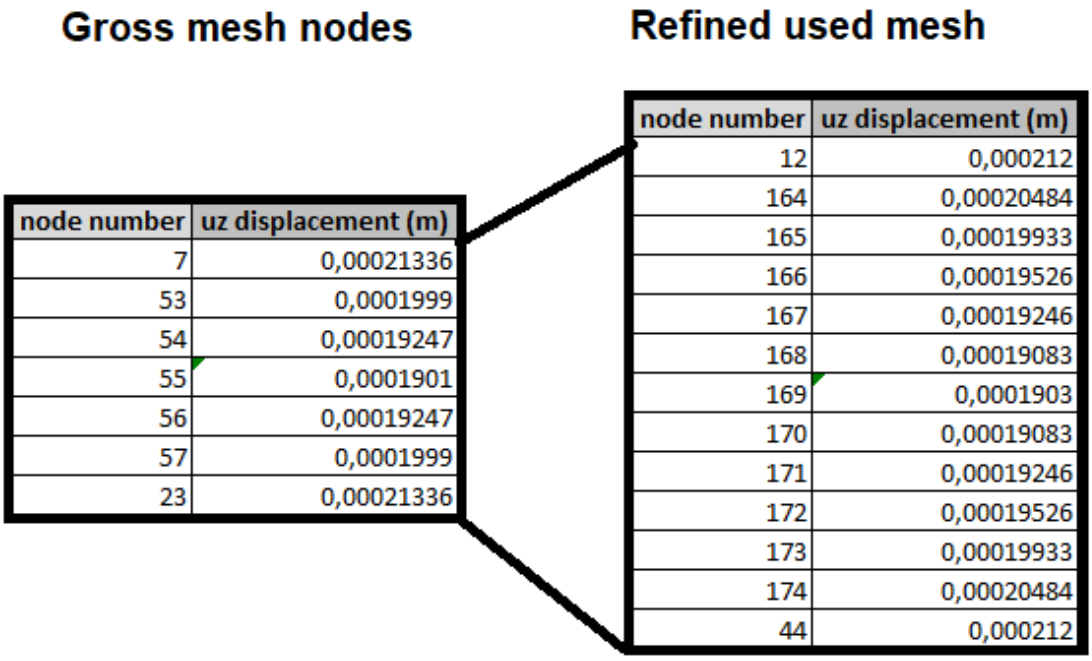

node number	uz displacement (m)
7	0,00021336
53	0,0001999
54	0,00019247
55	0,0001901
56	0,00019247
57	0,0001999
23	0,00021336

node number	uz displacement (m)
12	0,000212
164	0,00020484
165	0,00019933
166	0,00019526
167	0,00019246
168	0,00019083
169	0,0001903
170	0,00019083
171	0,00019246
172	0,00019526
173	0,00019933
174	0,00020484
44	0,000212

Figure 61 – S2 comparison of nodal displacement for unitary load line.

3.6. Crack modelling

Both slabs were designed as beam strips subjected to four-point loads (Figure 62). In fact, as Slabs 1 and 2 are one-way slabs, the bending moment diagram in this kind of structure is constant across the width of the element, what allows the design

procedure to employ a beam strip of unit width, using the same formulas and procedures for rectangular beams elements (Chen and Lui, 2004).

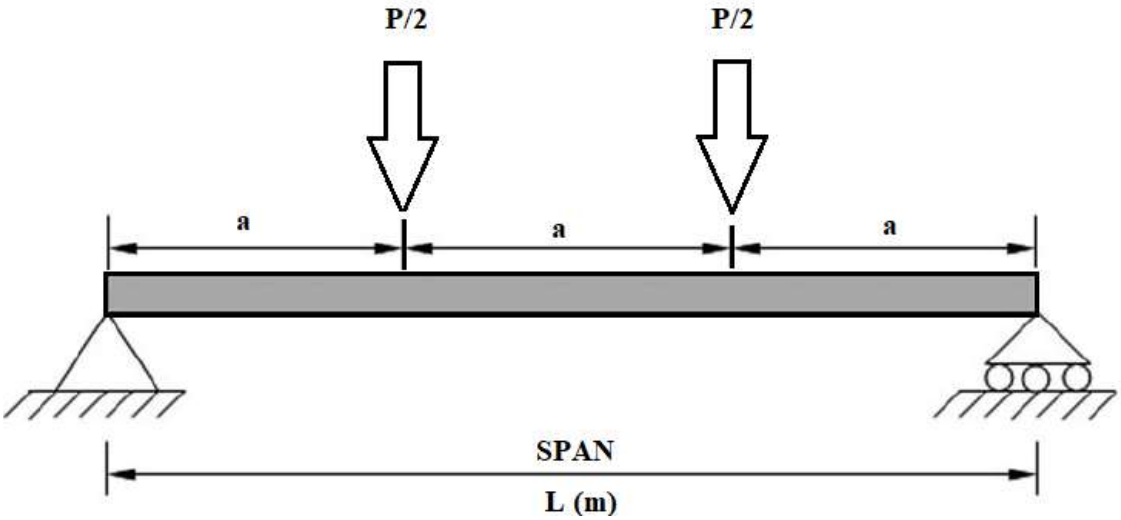

Figure 62 – Slab considered as simply supported beam.

The first visible crack in S1 appeared for the load of 8 kN while for S2 it occurred at 15 kN. It is possible to evaluate the correspondence of the phenomenon with the calculated cracking moment, which is the moment that causes the first crack to appear. According to brazilian concrete design standard NBR 6118/2014, the cracking moment of a concrete element is given by Equation 7:

$$M_{CR} = (\alpha * f_{CT} * I_G)/Y_t \quad (7)$$

where α is a factor that aproximately correlates concrete's tension strength in bending to direct tension strength. The value of α is 1.2 for T or double-T sections and 1.5 for rectangular sections. The value f_{CT} is the direct tension strength of concrete. For excessive crack formation, according to NBR 6118/2014 standard:

$$f_{CT} = 0.21 * f_{ck}^{\frac{2}{3}}, MPa \quad (8)$$

I_G is the gross moment of inertia (reinforcement is neglected)

Y_t is the distance from neutral axis to the most extreme fiber subjected to tension.

For both slabs:

$$I_G = (b * h^3)/12 \quad (9)$$

$$Y_t = (height\ of\ slab)/2 = 0.04\ m \quad (10)$$

Making the inverse way it is possible to find the load P that generates the cracking moment. Considering both rectangular sections (S1 having 1.35m x 0.08 m and S2 having 1.65m x 0.08 m), the cracking moments of slabs 1 and 2 were equivalent

to a load of, respectively, 7.69 kN and 13.62 kN. Considering that load tests, the first cracks appeared at 8 kN for S1 and 15 kN for S2; it is, thus, in accordance to the theoretical calculations.

In sequence, cracks produce changes in a section of concrete subjected to bending, as shown in Figure 63.

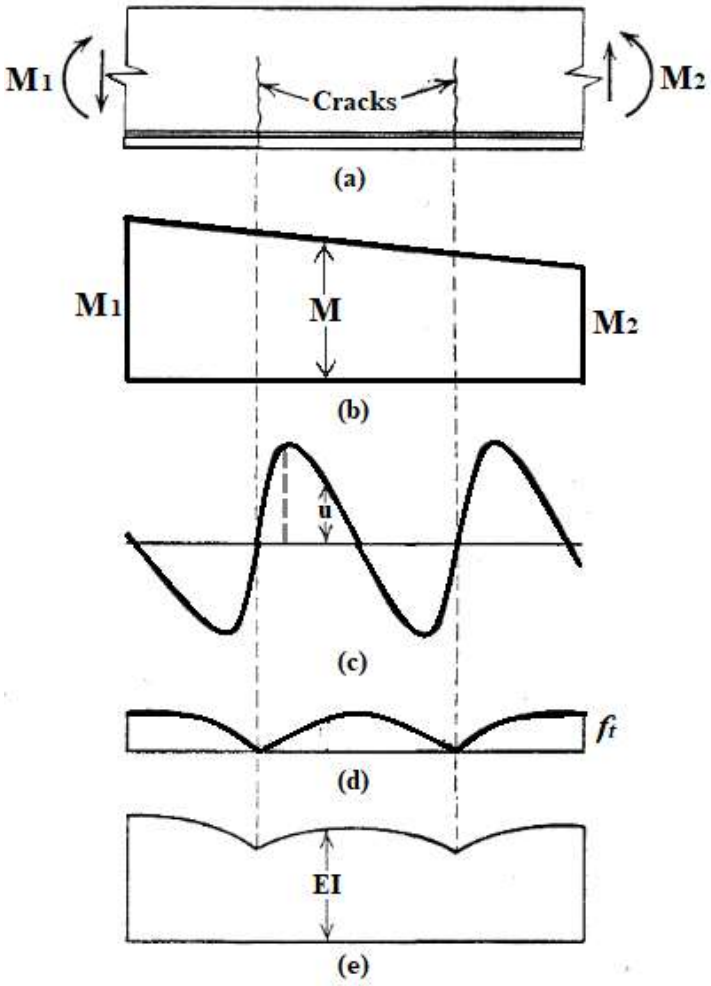

Figure 63 – Cracking in a reinforced concrete element subjected to flexure (a) produce changes in (b) bending moment distribution, (c) bond stress distribution, (d) concrete tensile stress distribution and (e) flexural rigidity distribution. (Source: Park and Paulay, 1975)

Considering the flexural stiffness EI, there is a reduction caused by cracking. Based on ACI 318 and NBR 6118, the moment of inertia of a cracked section of concrete (I_{cr}) in a stage where the contribution of cracked concrete is not considered (as shown in Figure 64) is:

$$I_{cr} = \frac{b*x^3}{12} + b * x * \left(\frac{x}{2}\right)^2 + \alpha_{eq} * \mathrm{A}_{steel} * (d - x)^2 \qquad (11)$$

The position of neutral axis *x* is given by:

$$\frac{b}{2} * x^2 + \alpha_{eq} * \mathrm{A}_{steel} * x - \alpha_{eq} * \mathrm{A}_{steel} * \mathrm{d} = 0 \qquad (12)$$

The value α_{eq} converts concrete into steel by dividing the elastic module of both materials ($\alpha_{eq} = E_{eteel} / E_{sc}$, where E_{steel} = 210 GPa according to NBR6118/2014 and E_{sc} comes from Equations 5 and 6). In Eq. (11), x stands for the position of neutral axis with respect to the top border of the section, and d is the distance between the center of gravity of reinforcement and the compressed edge. According to ACI 318 and NBR 6118/2014, the following approximation gives reasonable results for the equivalent moment of inertia of a cracked section as the applied moment increases:

$$I_{eq} = \left(\frac{M_{Cr}}{M_a}\right)^3 * I_G + \left[1 - \left(\frac{M_{Cr}}{M_a}\right)^3\right] * I_{cr} \leq I_G \qquad (13)$$

where M_a is the maximum service load moment (unfactored) in member at stage of deflection is computed (the moment in the section at that stage of load) and M_{CR} is the cracking moment. It can also be noticed that the equivalent moment of inertia I_{eq} is, at most, equal to the gross moment of intertia. Calculating the equivalent moment of intertia (that occurs after the section reaches the cracking moment) for both slabs and dividing by the gross moment of inertia, a factor of stiffness reduction can be found. The results are arranged in Table 5 for S1 and Table 6 for S2.

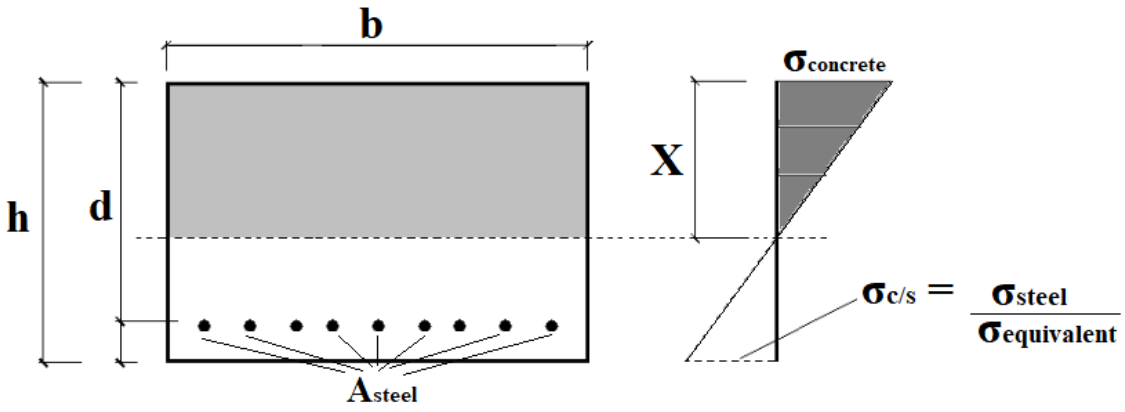

Figure 64 – Stress distribution in a concrete section in flexure with no contribution of concrete.

Load (kN)	$(M_{cr}/M_a)^3$	I_e (cm^4)	I_e/I_g
8	0,889678	5186,296	0,9004
16	0,111210	1138,030	0,1976
22	0,042779	782,172	0,1358
24	0,032951	731,062	0,1269

Table 5 – Ratio between moments of intertia for S1

Load (kN)	$(M_{cr}/M_a)^3$	I_e (cm^4)	I_e/I_g
15	0,742198	5467,241	0,7766
17	0,509855	4049,802	0,5753
18	0,412285	3454,564	0,4907
21	0,270480	2589,464	0,3678
24	0,181201	2044,802	0,2905
27	0,127263	1715,748	0,2437
42,5	0,032631	1138,430	0,1617
62,5	0,010260	1001,956	0,1423

Table 6 – Ratio between moments of intertia for S2

The ratios of moment of inertia confirms a decrease in stiffness due to cracking. As both slabs are simply supported structures, that is, statically determined (isostatic), the stiffness distribution keeps depending on load configuration even after reaching the cracking moment, as can be seen on moment-curvature curve shown in Figure 65. It can be concluded that there is a direct relationship between moment applied and curvature of section and the link between them is the stifness *EI* which is the slope of this graph. Based on this fact and considering that S2 presented a decrease in frequency until the the level of 12 kN (before cracking moment was reached), a linear decrease of stiffness is proposed, based on moment applied as shown in Figure 66. The moment distribution has a trapezoid shape. As the moment applied increases from M_1 to M_2, more regions reach the cracking moment. For a line of finite elements at the same distance *x* from the origin, the proportional stiffness reduction was the same. The ratio used to decrease the stiffness considered the position of the element at that level of load and the quotient between the moment generated by the applied load *P* and the ultimate load moment (caused by a force of 62.5 kN). This modeling has already been tested for reinforced concrete cracked beams by other authors as Castel *et al* (2012) or Xu *et al* (2018). As the bending stiffness is the product of Young's module *E* and moment of inertia *I*, the reduction of stifness was made by penalising *E*. The model was initially considered isotropic and then was evaluated considering an orthotropic aproach.

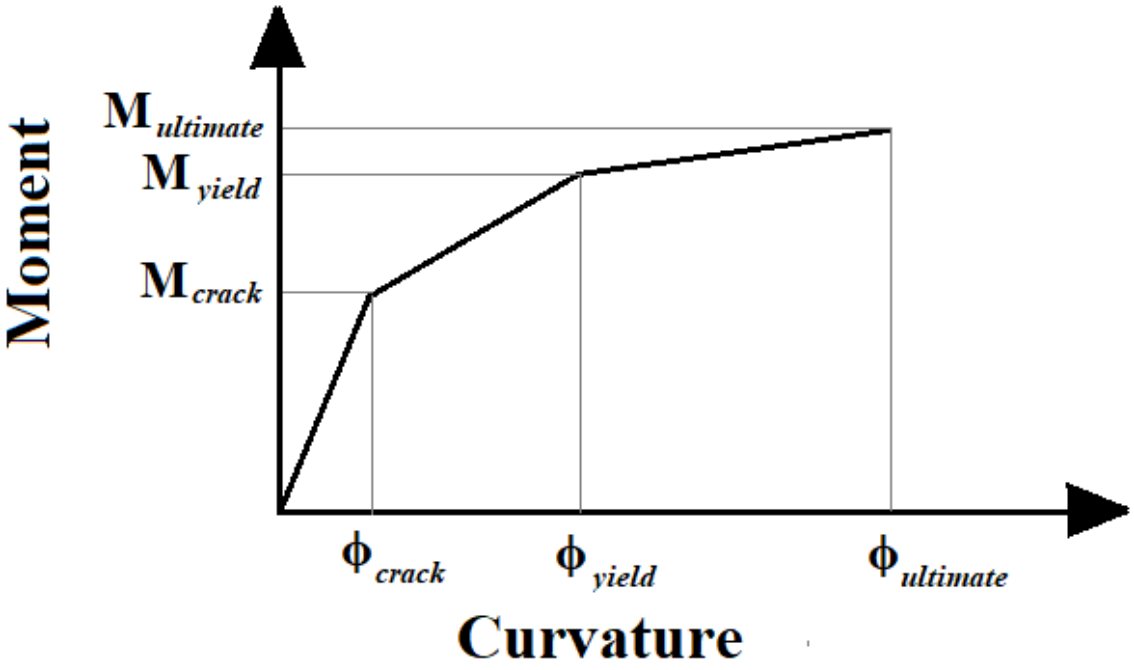

Figure 65 – Moment-curvature curve for a reinforced concrete section.

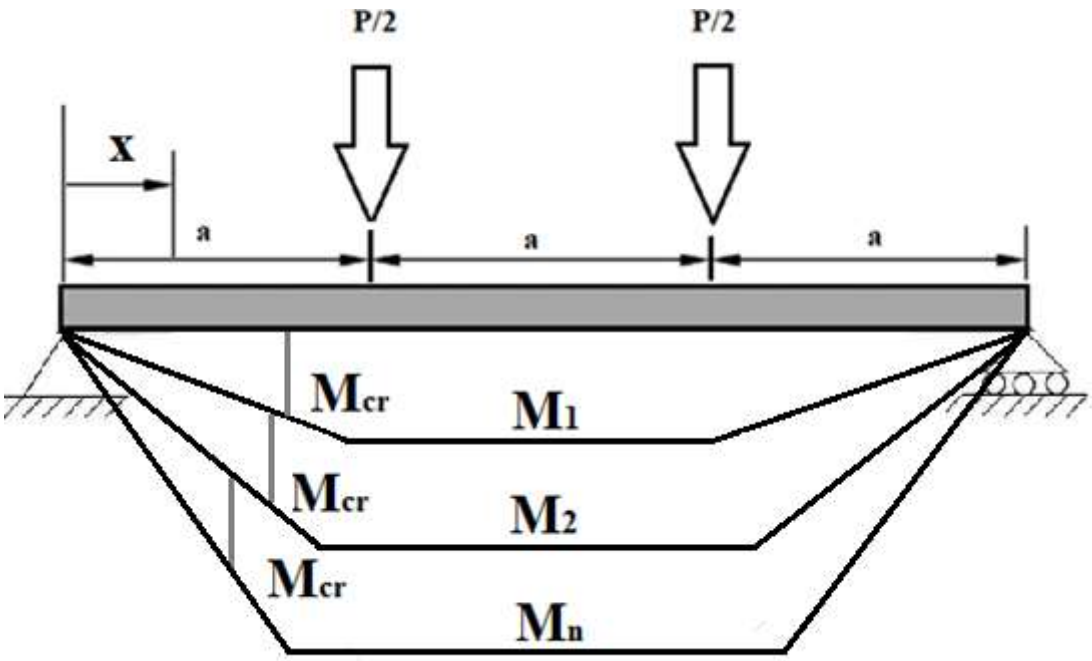

Figure 66 – Moment distribution for different levels of load.

Some visual indicators can corroborate the model adopted. For example, to the collapsed slab it is expected that the moment of cracking started at 33 cm from the support line. In an *in-situ* inspection it can be confirmed that this is the distance from the center line of support to the closer visible crack, as shown in Figure 67.

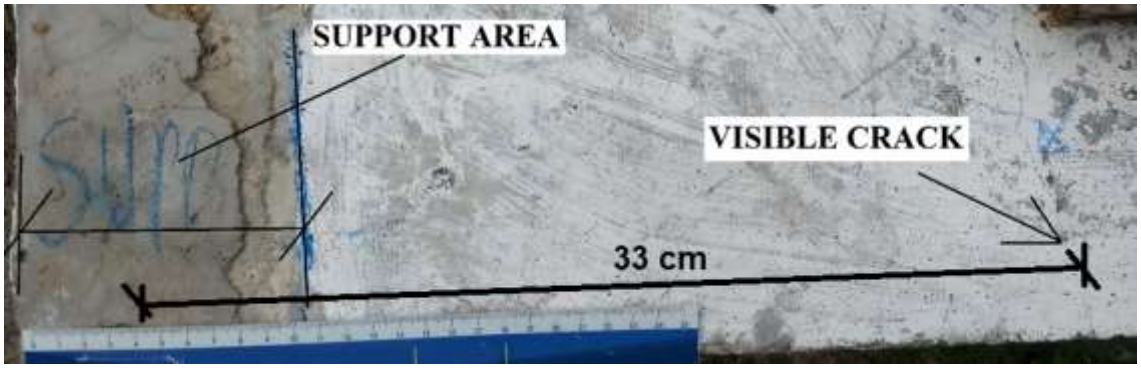

Figure 67 – Visual crack in the bottom of S2.

Another fact that agrees with the initial consideration of linear material is that, as shown in Equation 1, there is a direct relationship between frequency and stiffness, which is related to the load applied. Ploting frequency against square-root of load applied in Figure 68, it can be seen that there is a linear relation until 12 kN, followed by a change of slope in the next load level because the cracking moment was reached.

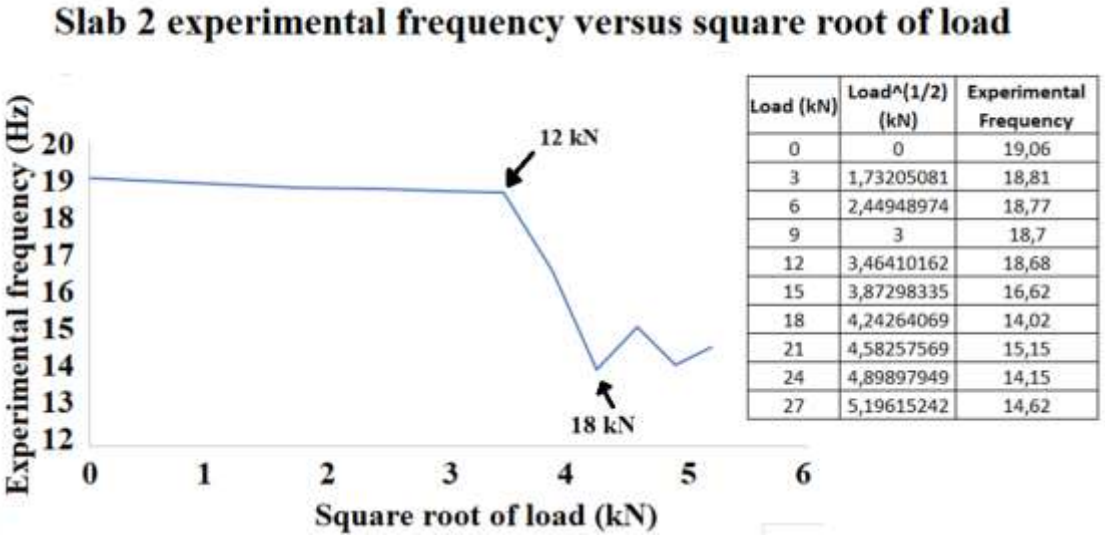

Load (kN)	Load^(1/2) (kN)	Experimental Frequency
0	0	19,06
3	1,73205081	18,81
6	2,44948974	18,77
9	3	18,7
12	3,46410162	18,68
15	3,87298335	16,62
18	4,24264069	14,02
21	4,58257569	15,15
24	4,89897949	14,15
27	5,19615242	14,62

Figure 68 – Frequency versus square-root of load for S2

In addition to the reduction of inertia for the region that overcome the cracking moment, the presence of a visible crack also produces local stiffness reduction. Christides and Barr (1984) considered the effect of a crack in a continuous beam and calculated the stiffness, EI, for a rectangular beam adopting an exponential function given by

$$\mathrm{EI(x)} = (\mathrm{EI_0})/(1 + \mathrm{C} * e\left(-2\alpha|\mathrm{y} - \mathrm{y_j}|/\mathrm{h}\right)) \qquad (14)$$

where $C = (I_0 - I_{cj})/I_{cj}$, $I_0 = w*h^3/12$ and $I_{cj} = w(h - h_{cj})^3/12$ are the second moment of areas of the undamaged beam and at the jth crack, w and h are the width and depth of the undamaged beam, and h_{cj} is the crack depth. y is the position along the beam and y_j

the position of the crack; finally, α is a constant that Christides and Barr estimated from experiments to be 0.667. Sinha et al (2002) used a simplified approach, where the stiffness reduction of Christides and Barr (1984) was approximated by a triangular reduction in stiffness. It should be mentioned that, based in this model of crack, nearby cracks causes superposition of stiffness loss. This approach was tested by Friswell and Penny (2002) for different crack depths in numerical modeling using the models of Sinha et al. (2002) and Christides and Barr (1984) and the crack effects of both models are illustrated in Figure 69. The squares represents the ares of influence of a crack where the peak of stifnness loss is located in the exact position of the crack. It is important to mention that a superposition of stiffness loss can happen for cracks close to other cracks.

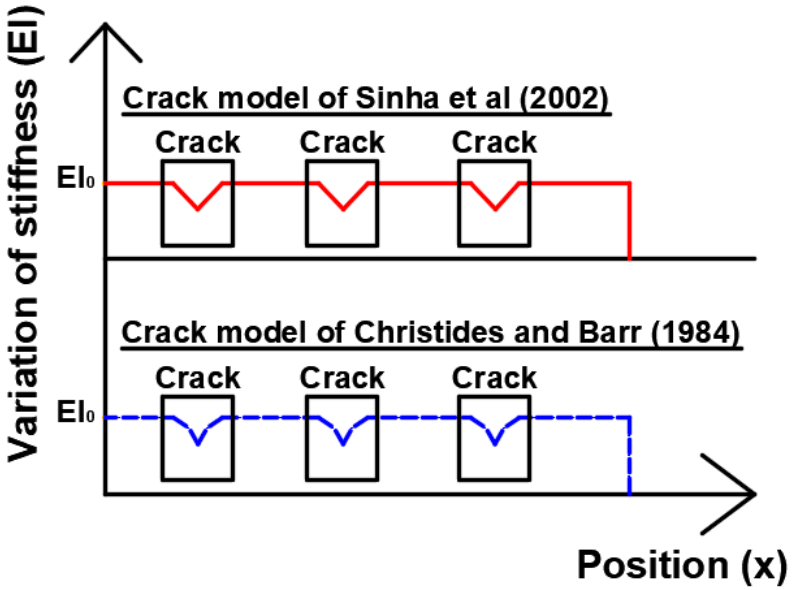

Figure 69 – Variation of stiffness using approaches of Christides and Barr (1984) (curved line) and Sinha *et al* (2002) (straight line) for crack depth of (a) 5% and (b) 25%.

For both slabs, two main models were used:

- In the named “Model 1”, for the region reaching crack moment of inertia, the elastic module was reduced through a factor obtained by the ratio of equivalent moment of intertia (I_{eq} in Equation 13) and the gross moment of inertia (I_g where the section was considered composed only by concrete and uncracked). As the load level increases, the reduction factors produded higher decrease of stiffness and more regions reaches cracking moment;
- In the named “Model 2, for the elements that contained cracks, an initial reduction of 0.85 was used to consider the local stiffness reduction caused by a crack with 5% depth based in Christides and Barr (1984), increasing this loss for higher load levels. This initial consideration of

crack deepness was made since no experimental measurement was available.

For “Model 2”, based on Christides and Barr (1984) and Sinha *et al* (2002), the area of incluence of new cracks was set as three times the slab thickness (3*8cm = 24 cm) for both slabs. Since no information about the crack’s depth was available, they were initially set as 5% of slab height (4.2 mm). The older the crack, the more intense was the local loss. Additionally, the elements with new cracks (for a given level of load) and already containing cracks of previous load levels had an additional loss of sitffness. In fact, for the load level of 15 kN in S2, for example, not only the first crack appeared because the moment of cracking was exceeded but also edge crack reaching more than half the slab thickness also appeared, as shown in Figure 70.

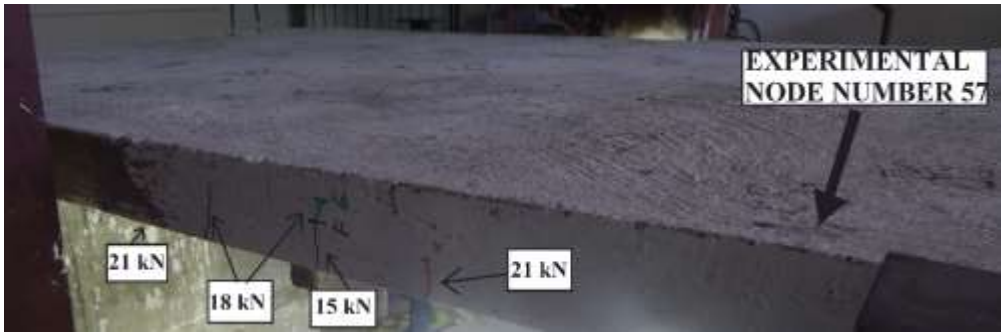

Figure 70 – Lateral cracks on S2 for different load levels.

For both models mentioned above, two constitutive relations were used: an isotropic and an orthotropic model. In a linear regime, the shear modulus of concrete is given by Equation 15, which was used in the isotropic model. In the isotropic model, the reduction of stiffness was the same in both directions.

$$G(xy) = (E_x)/2(1+\nu) \quad (15)$$

When the element used was orthotropic, due to the direction of cracks, the elastic modulus in *x-direction* was penalized in order to simulate a stiffness reduction, which was reduced only in the direction along the main span. The shear modulus of orthotropic linear material is given by Equation 16:

$$G(xy) = (E_x * E_y)/(E_x + E_y + 2 * \nu * E_y) \quad (16)$$

In order to illustrate the decrease of elastic modulus based on the distribution of moment at each stage of load, the position of the element and the final moment (at the

collapse load), Figure 71 shows a scheme of the adopted method. The reductions are made over the initial elastic module Ebeginning described in section 3.5. It can be seen that the higher the load level and the closer to the load line, the higher the elastic module decrease (what implies in stiffness “EI” reduction”). This method of reduction was used in Model 1 for the elements that did not reach the cracking moment and in Model 2 in the elements that did not show visible cracks. A basic fluxogram of the whole process os slab testing and modeling is shown in Figure 72.

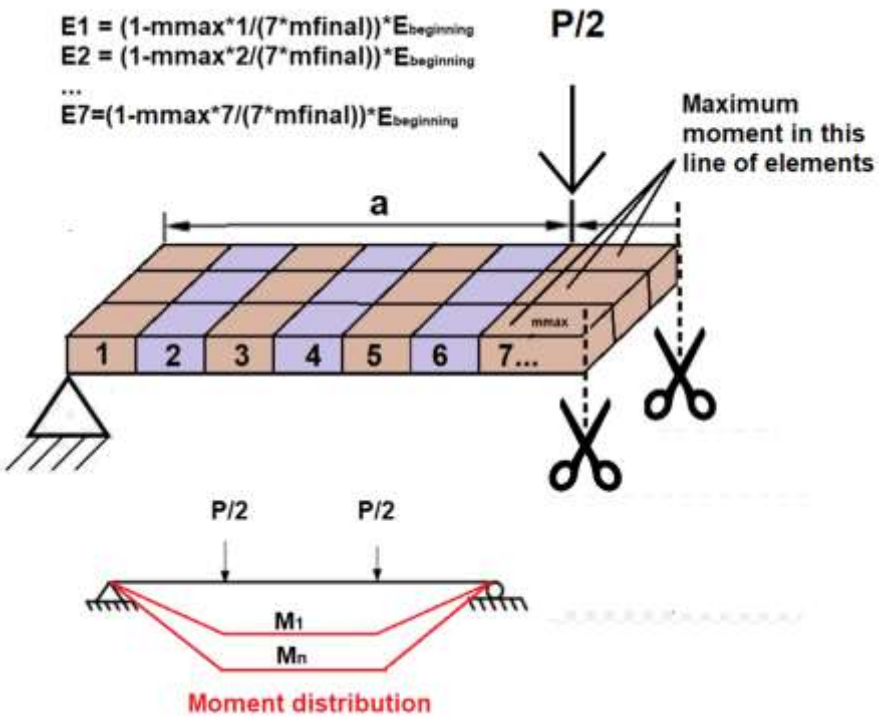

Figure 71 – Stiffness EI reduction based on moment distribution and element position.

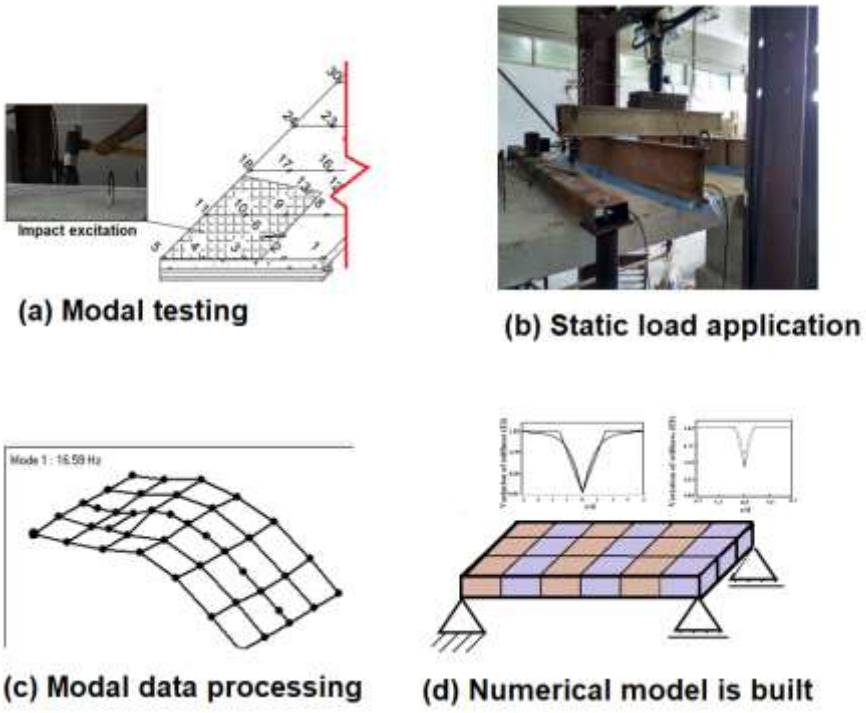

Figure 72 – Scheme of slabs testing and modeling.

4.RESULTS AND DISCUSSION

4.1. Static Load

a) S1

For S1, three load levels were used: 8 kN, 16 kN, 22 kN, that represented 33,33%, 66,67% and 91,67% of the collapse load, the latter being 24 kN. Although both slabs used the same loading system (beams at 1/3 and 2/3 of main span) and the measurement of displacement was made for all loading and unloading stages, measurements were made writing manually some points just for loading, what makes an evaluation of load versus displacement unable for S1.

b) S2

For S2, ten load stages were used in order to evaluate slab behavior about modal properties and cracking pattern. The stages were 3 kN, 6 kN, 9 kN, 12 kN, 15 kN, 18 kN, 21 kN, 24 kN, 27 kN and 42.5 kN, and the collapse was reached for a load of 62.5 kN. The displacement versus load is shown in Figure 74. An initial horizontal step is observed before deflection starts and it can be caused by an accommodation of the loading beams used for testing (the interface between loading beams and slab was filled

with plaster) or caused by an equipment error. For instance, for load level of 24 kN the graph shows that deflection starts only after 21 kN load level, what means that the data for this level is no longer trustworthy. For S2 the first visible crack began at the stage of 15 kN and this is the first loading level after cracking moment is reached, what can be observed in the change of loading slope shown in Figure 77. The changes in slopes at loading curves will be discussed later on.

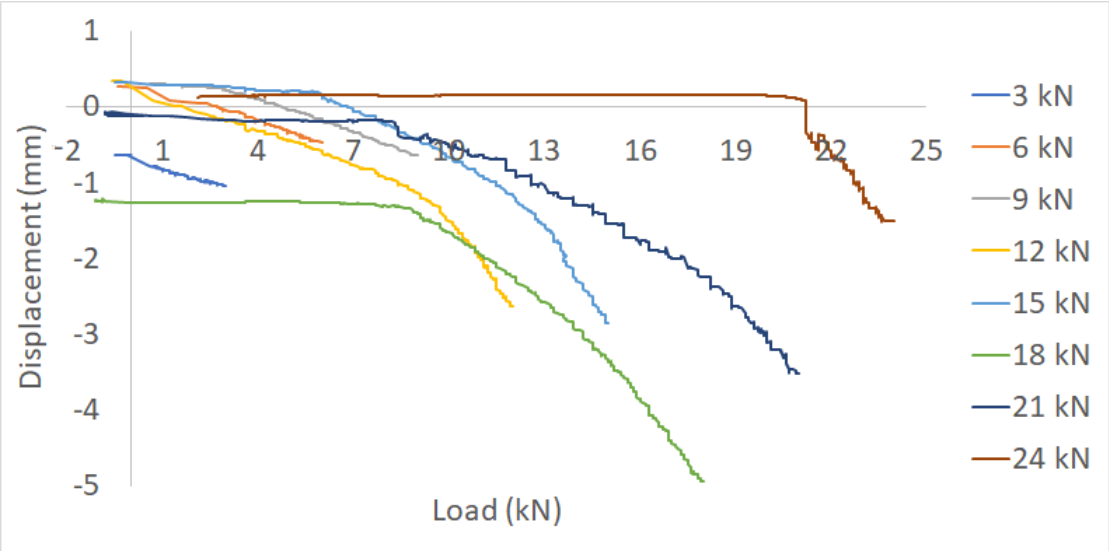

Figure 73 – Displacement of S2 along load.

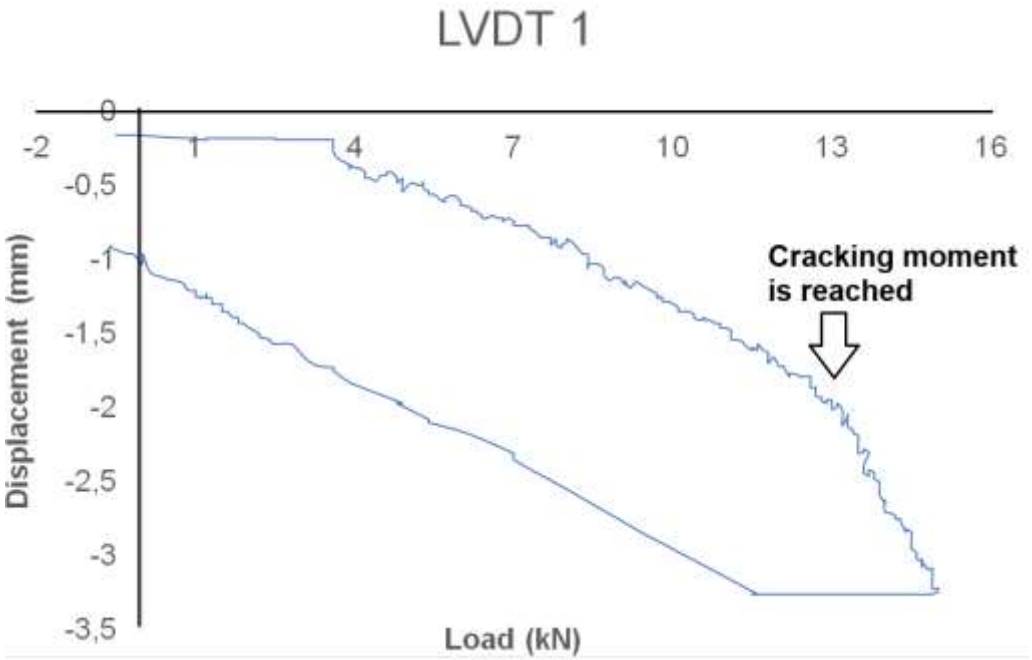

Figure 74 – Displacement of S2 along 15 kN load stage.

4.2. Impact tests on slabs

4.2.1. Evaluating sources of error

Prior to signal processing in time domain (particularly for evaluation of frequency along decay), it is important to have accuracy in determining the natural frequency in each vibration cycle. From the acquisition rate of 1/1024 s (1024 Hz) used in both slabs, one may think that the error in time domain are of aproximately +/- 0.001s. For the second slab, in special, the reduction in natural frequencies is related to a change in period of vibration around the error range previously mentioned. For S2, for example, the first experimental frequency is f_1 = 19.06 Hz, meaning a period of t_1= 0.05246 s for the undamaged state. When the error is added (+/- 0.001s), the frequency range from the error is (18.70 Hz; 19.43 Hz), meaning a difference of +/- 0.37 Hz.

In fact, the error in frequency is lower than the one previously mentioned. To evaluate it, a simple and undamped system ruled by and harmonic function will represent S2 vibrating in one of its modes, as shown in Equation 17:

$$X(t) = A_0 * \sin(\omega_0 t) \quad (17)$$

where A_0 is the amplitude of movement, ω_0 is the angular frequency and t is the time.

Consider, for instance, that this system has the same amplitude of a signal in time domain used for gradient obtainment in S2 (for instance, with a value of 0.02 V), and the same frequency f_1 =19.06 Hz of the first mode (which means that $\omega_0 = 2 * \pi * f_1$ = 119.697 rad/s). Plotting the graph of Equation 17 and making an interpolation between two consecutive points, as shown in Figure 75, the time Δt can be obtained. The time Δt is the difference between two consecutive points of the discrete time domain signal, the actual one and the interpolated, as shown in Figure 76. The maximum error that can occur when evaluating the period of the vibration cycle is twice Δt (at the beginning and the end of sine curve). In the most unfavourable situation, Δt=9.3578e-6 from the interpolation shown in Figure 76, and the maximum error is $t = 2*\Delta t$, which is not significant.

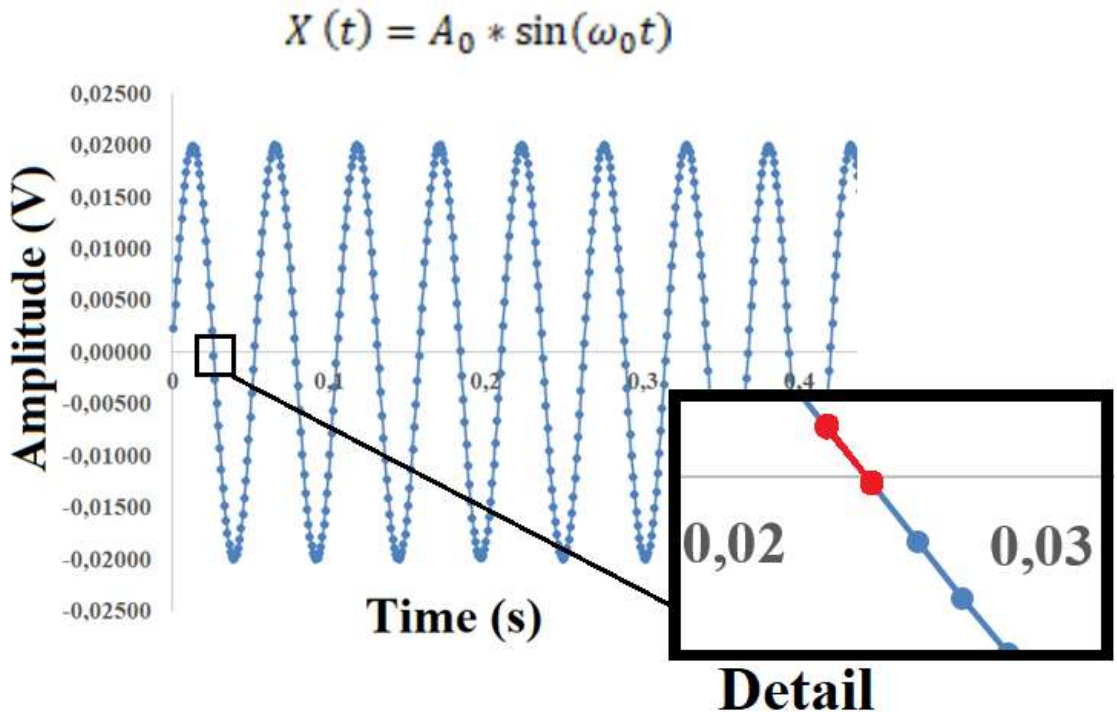

Figure 75 – Harmonic undamped system plot.

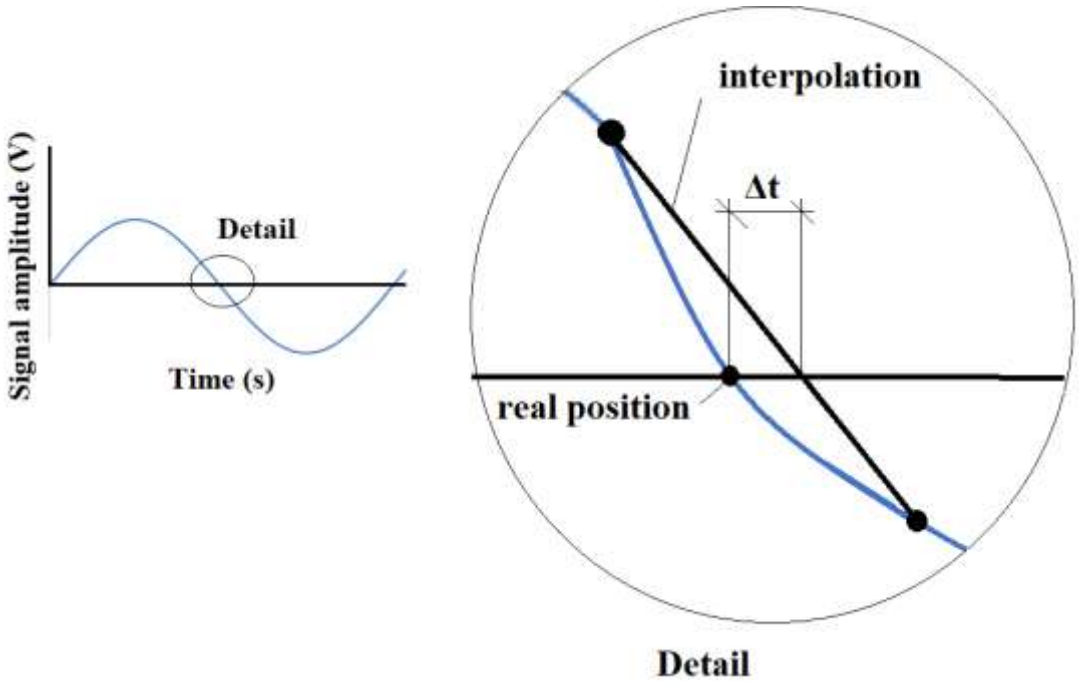

Figure 76 – Detail of maximum possible error.

Another possible source of error is the level of noise at which the structure is subjected. As can be seen in Figure 77 for S2 for the spectrum obtained by considering

the ambient excitation sources only, the noise level is significantly lower than the produced by an impact excitation, meaning that it it is negligible

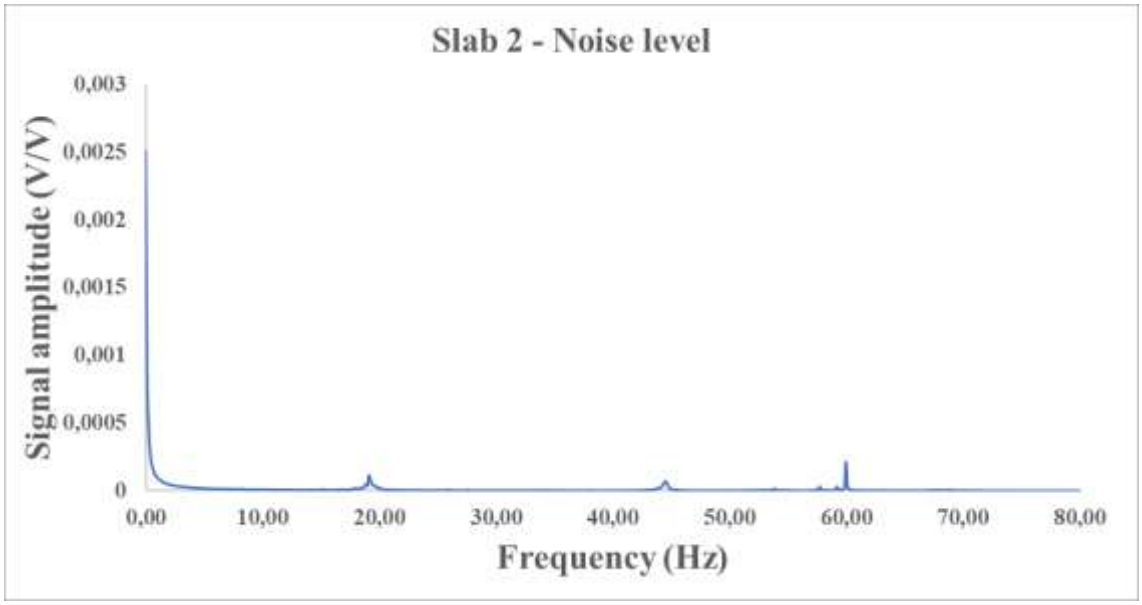

Figure 77 – Noise level in S2 at point 18.

4.2.2. Results from modal testing

As mentioned in the previous section, repeatability, reciprocity and linearity tests were performed in order to follow the behavior of slabs as damage increased (the result of a cracking process). The results of repeatability tests for S1 were processed by Guedes (2016) and are shown in Figures 78 to 85. Linearity tests indicate that, for increasing damage levels, less agreement is observed at the same excitation point. As the structure cracks, the opening and closing of the crack makes excitation at different nodes in reciprocity test excites much one frequency than other.

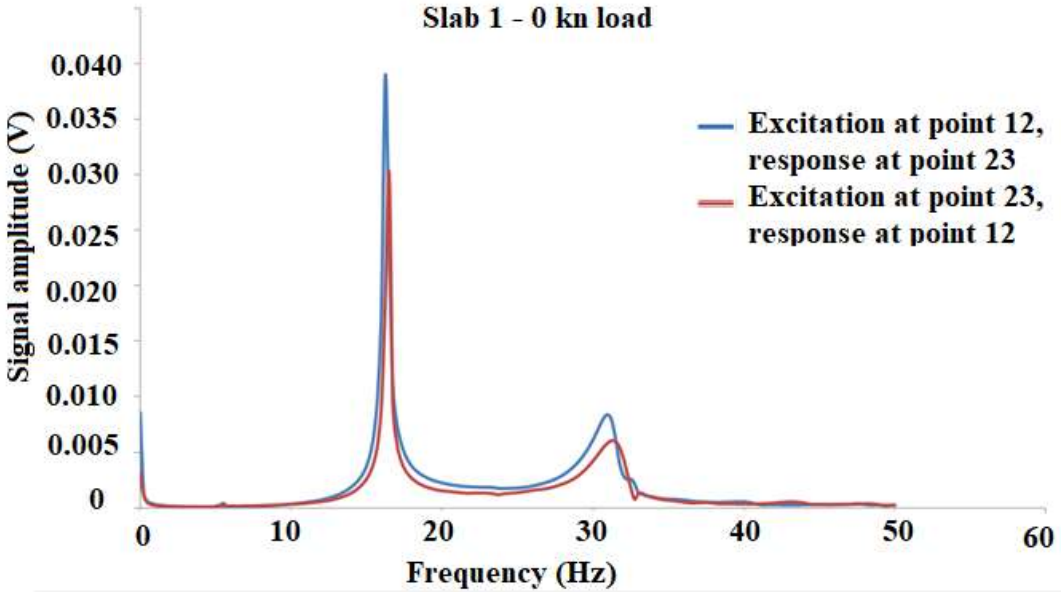

Figure 78 – Reciprocity test for S1 in 0 kN load level. (Guedes, 2016)

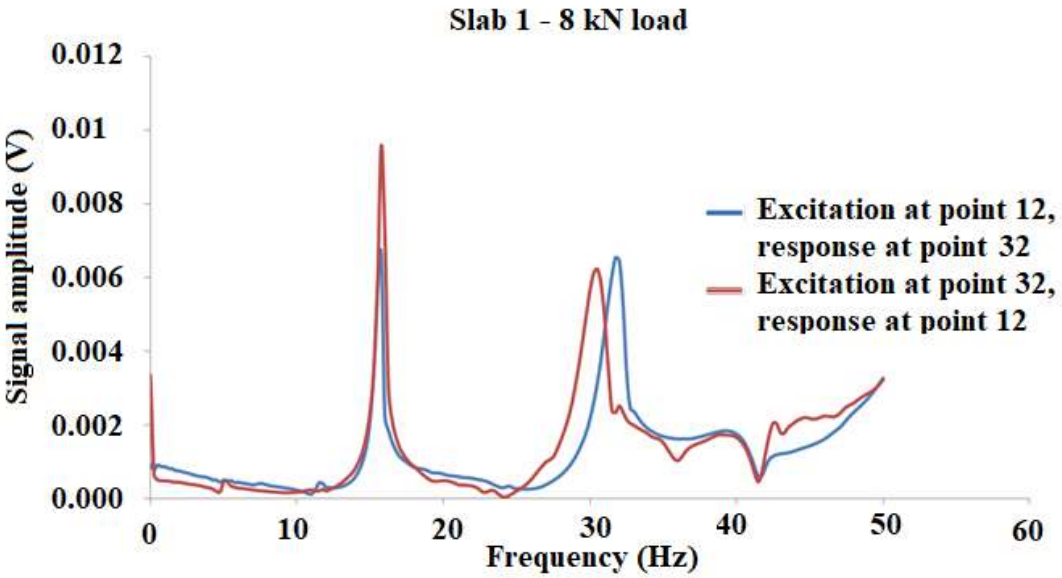

Figure 79 – Reciprocity test for S1 in 8 kN load level. (Guedes, 2016)

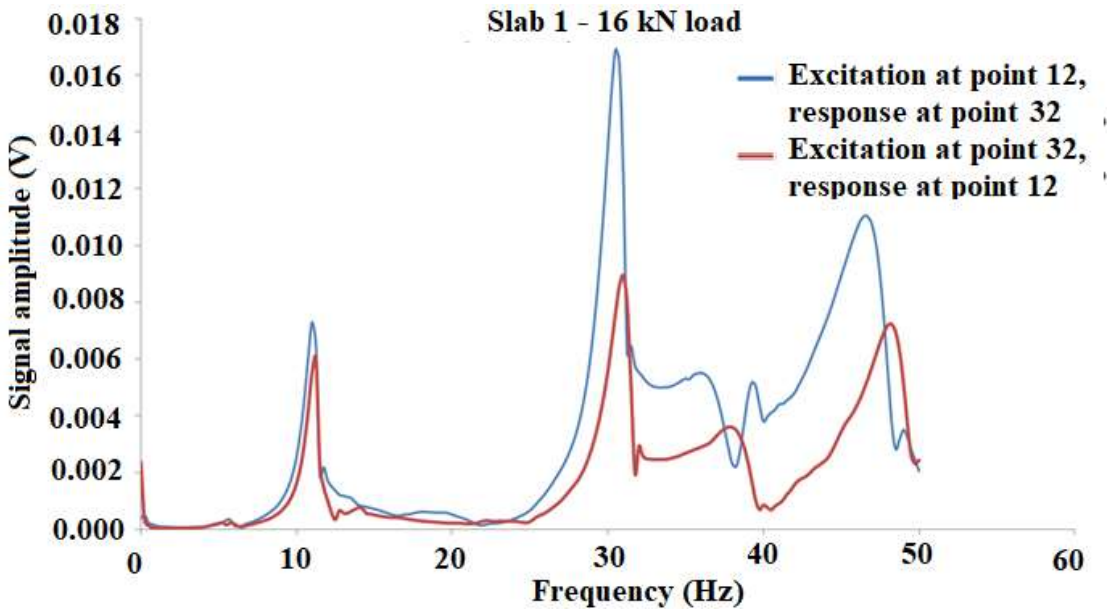

Figure 80 – Reciprocity test for S1 in 16 kN load level. (Guedes, 2016)

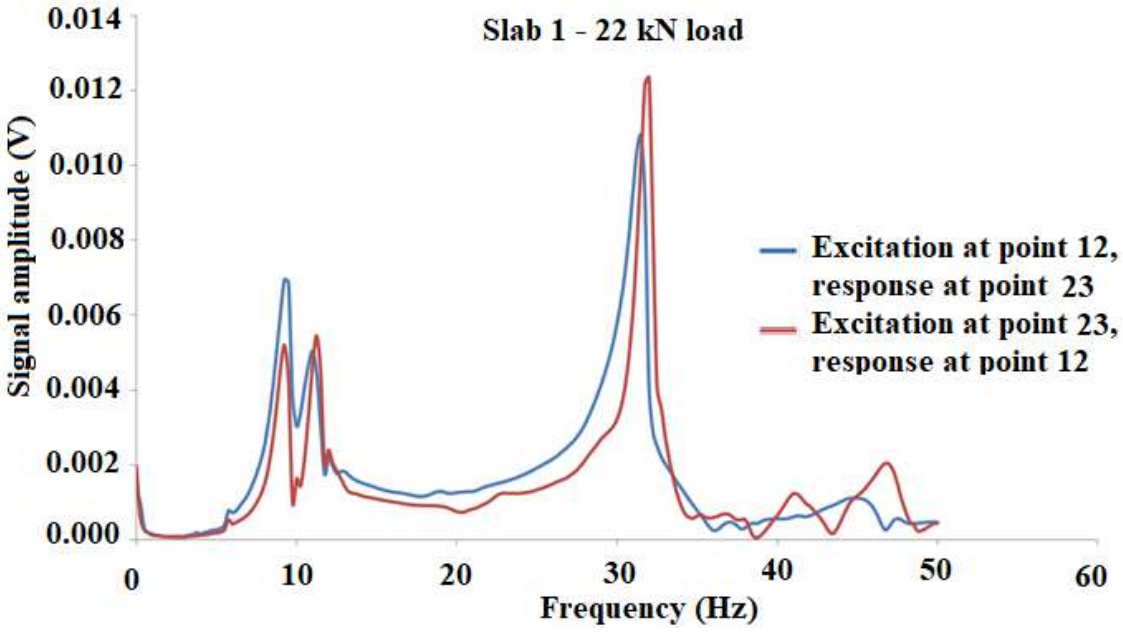

Figure 81 – Reciprocity test for S1 in 22 kN load level. (Guedes, 2016)

The results of linearity test in S1 (Figures 82 to 85) shows that, for increasing load levels, stronger impact excitations produced shift in frequency in comparison to normal impact excitation, an indicator of change in linear behavior.

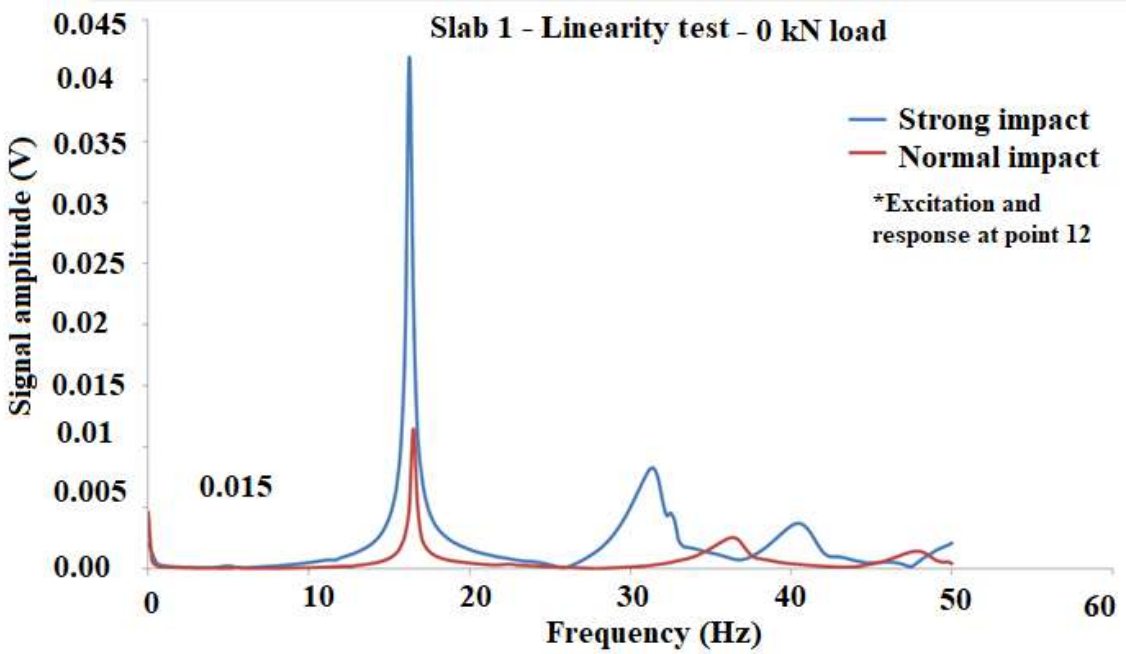

Figure 82 – Linearity test of S1 for undamaged state. (Guedes, 2016)

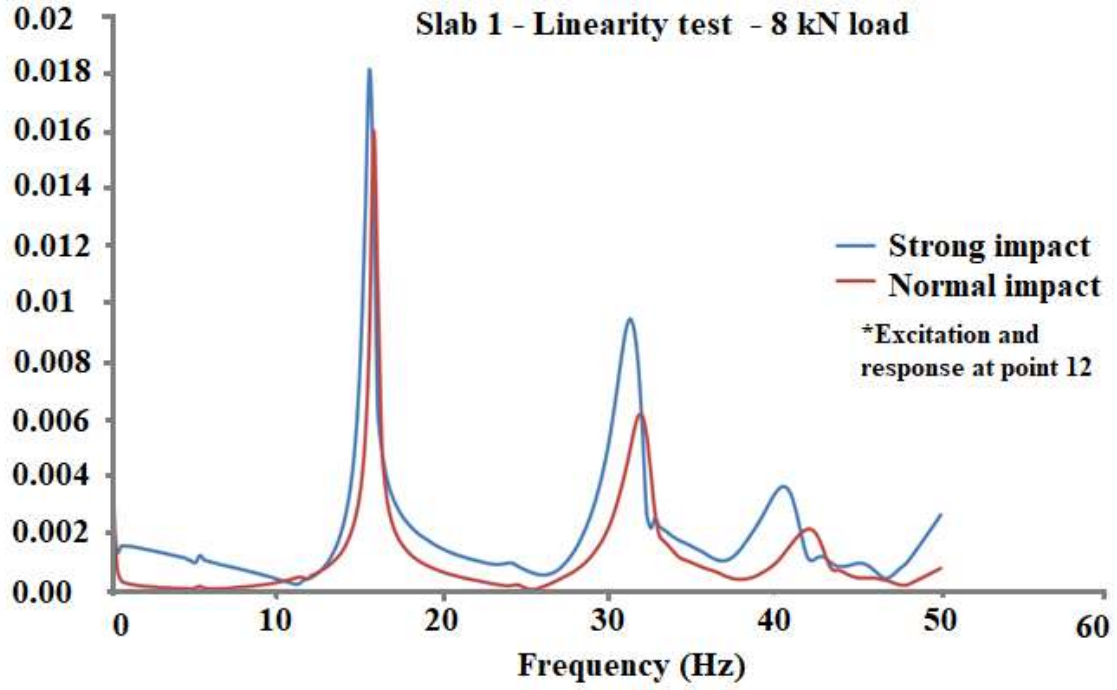

Figure 83 – Linearity test of S1 for loading level of 8 kN. (Guedes, 2016)

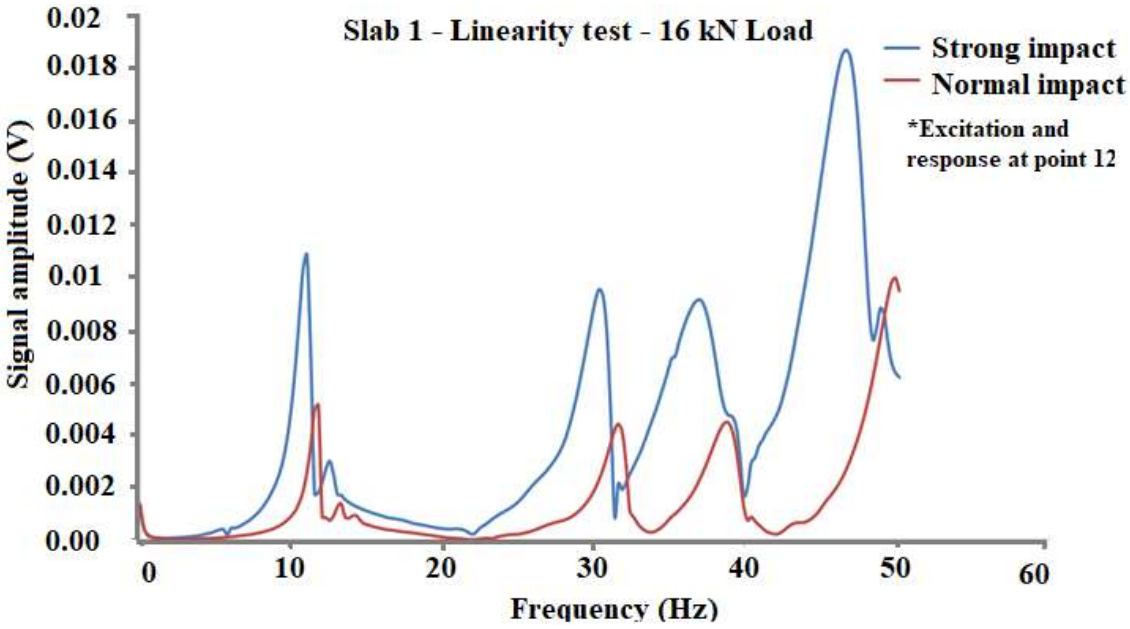

Figure 84 – Linearity test of S1 for loading level of 16 kN. (Guedes, 2016)

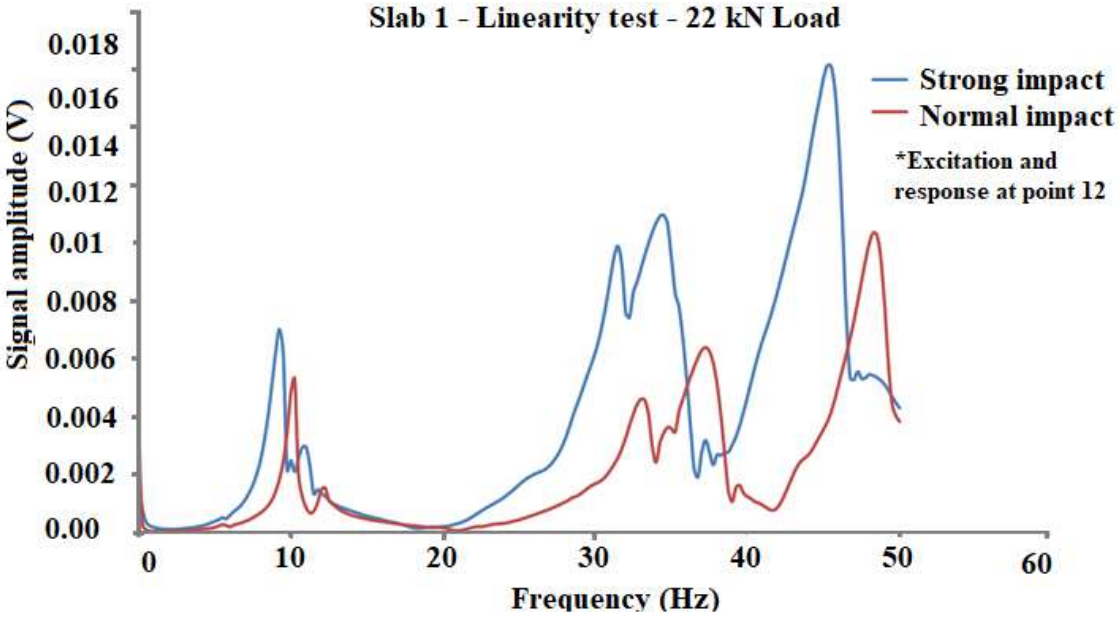

Figure 85 – Linearity test of S1 for loading level of 22 kN. (Guedes, 2016)

The test of repeatability of S2 for the undamaged (0 kN) state shows good agreement in the peaks of frequency of interest (the three initial peaks), what is an indicator of linear behavior for the undamaged structure, as shown in Figure 86 for one

of the driving points. As for the reciprocity test, it could be noticed that the supperposition of FRFs tends to decrease with the increase of load level, as shown in Figures 87 to 95. In agreement to the repetability test made in the undamaged structure (Figure 86), the reciprocity for the same load level of 0 kN shows supperposition in the peaks of frequency (Figure 87). When load level increases, the magnitude of the signal in the peaks change (Figures 89 to 95), in agreement to a reduction of stiffness due to cracking process. It is also noticed in the reciprotity test that the impact at different points produce different peaks of frequency as the damage increase. For load of 18 kN, for example, the excitation at node 18 excites more the first and third modes while the excitation at node 62 excites more the second mode.

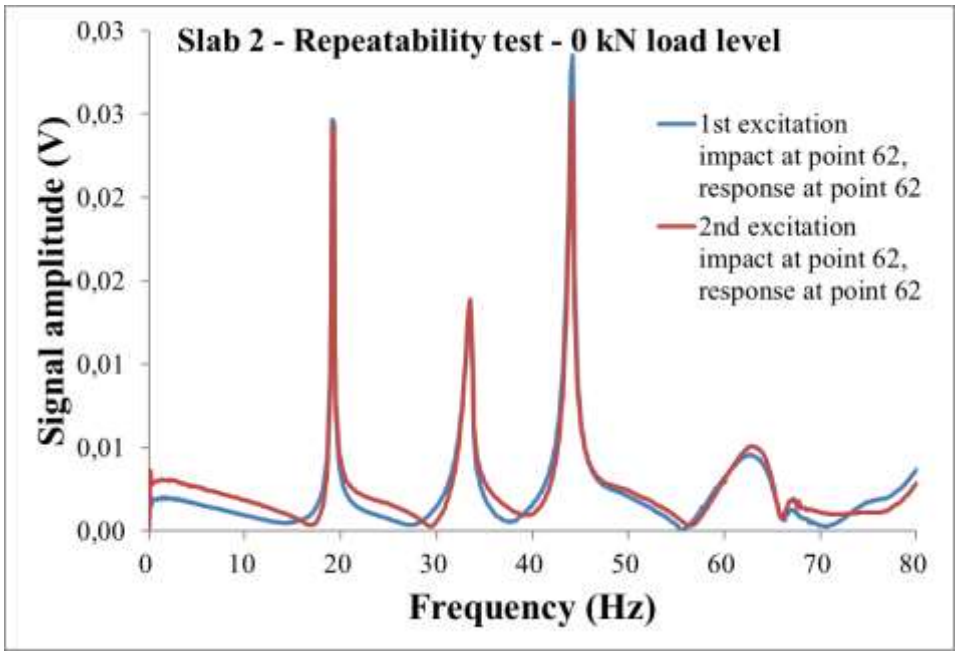

Figure 86 – Repeatability of S2 for 0 kN load level.

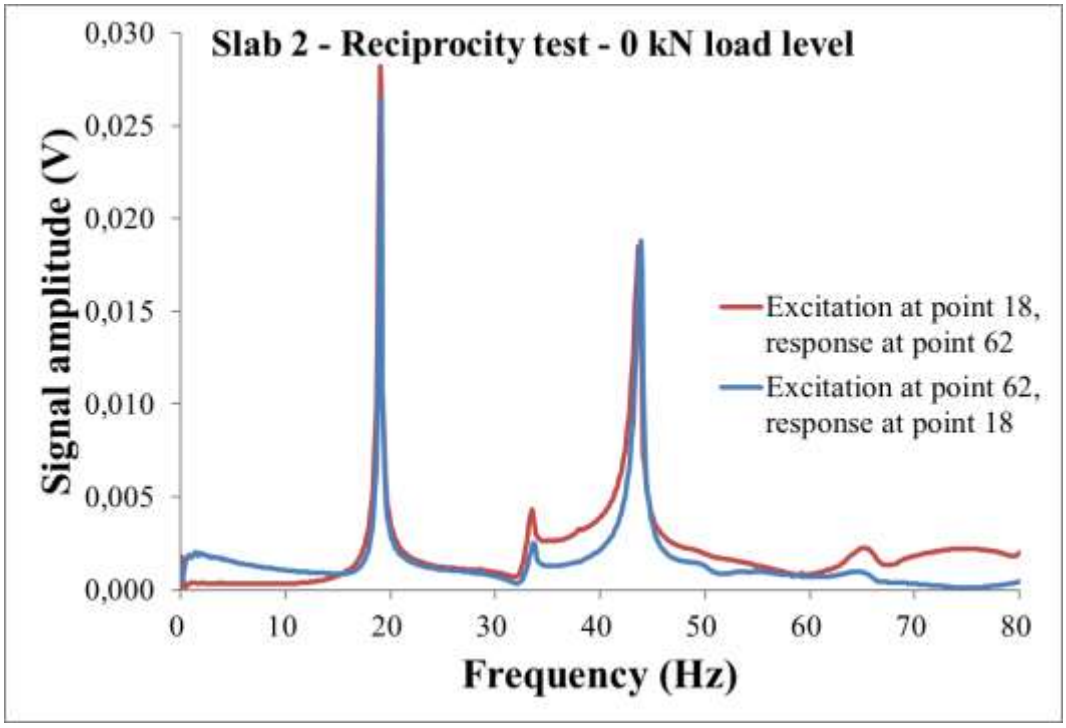

Figure 87 – Reciprocity test of S2 for 0 kN load level.

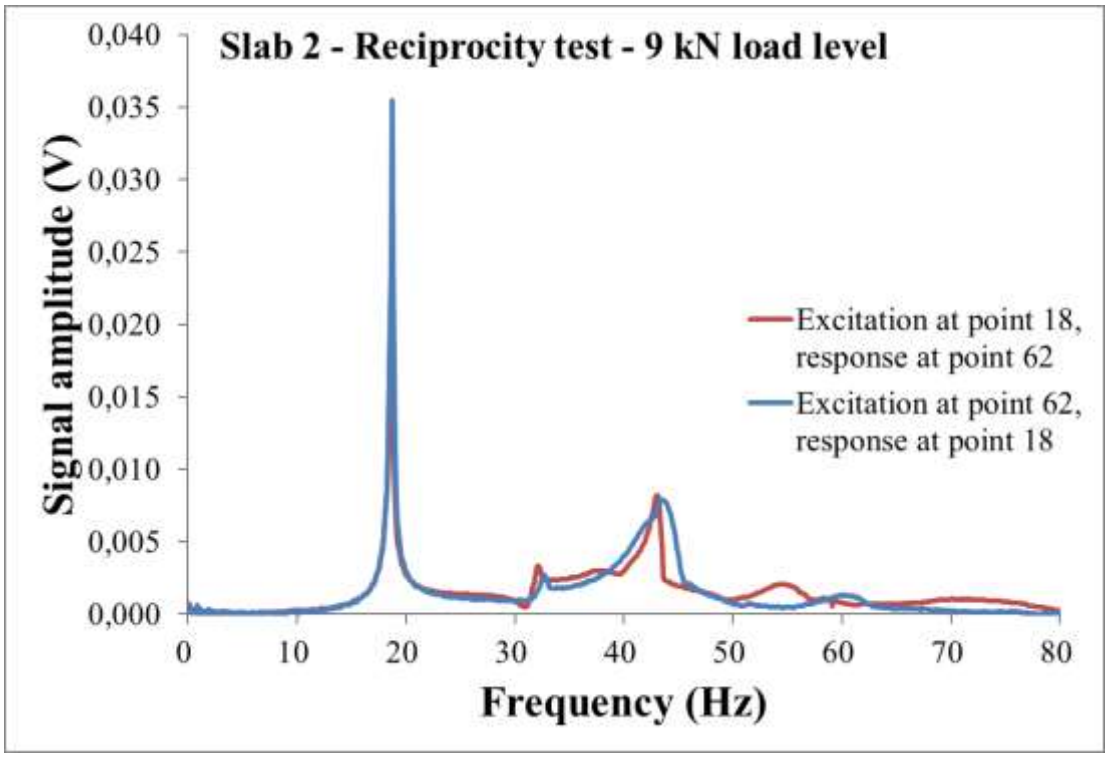

Figure 88 – Reciprocity test of S2 for 9 kN load level.

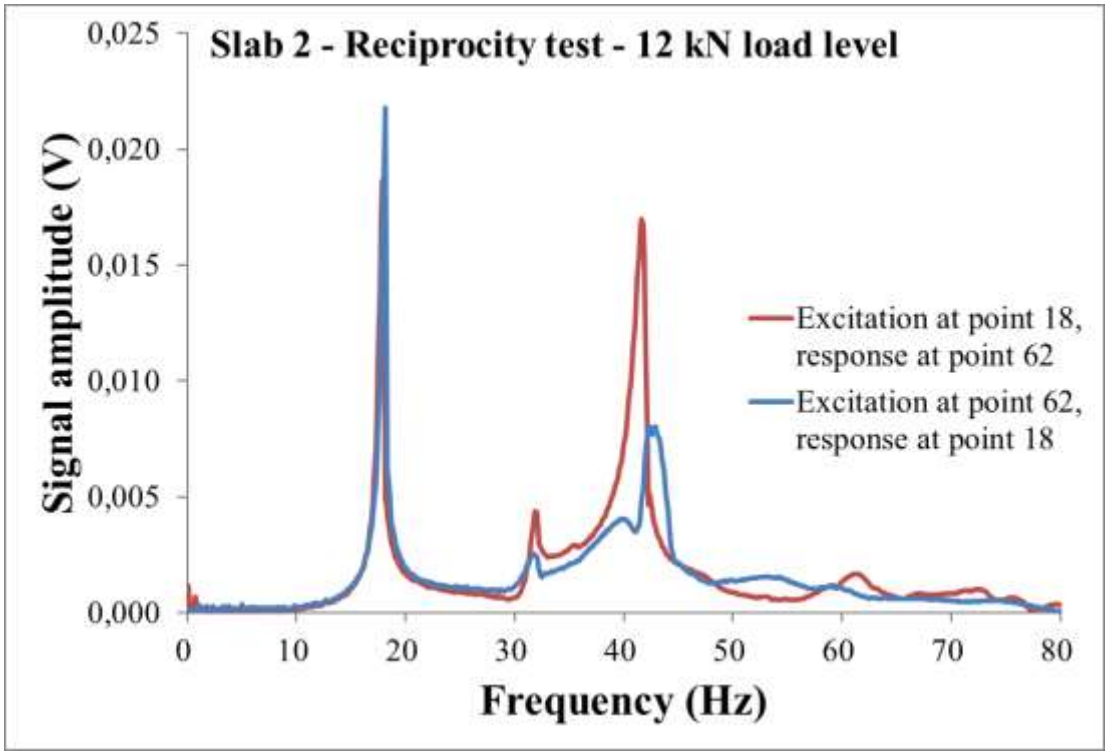

Figure 89 – Reciprocity test of S2 for 12 kN load level.

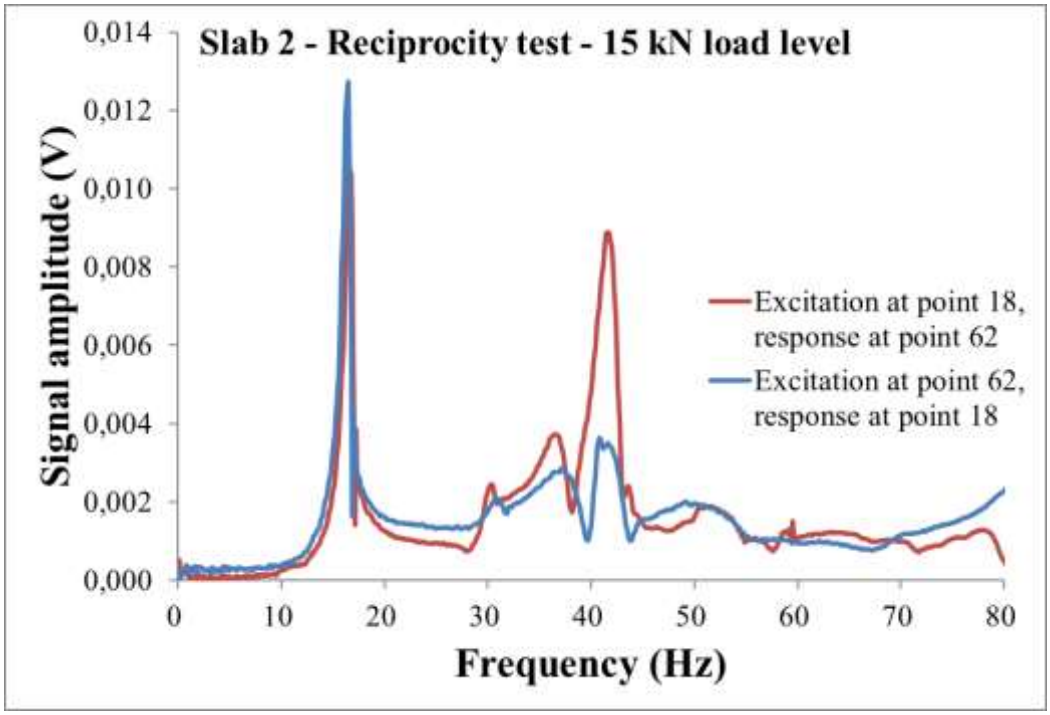

Figure 90 – Reciprocity test of S2 for 15 kN load level.

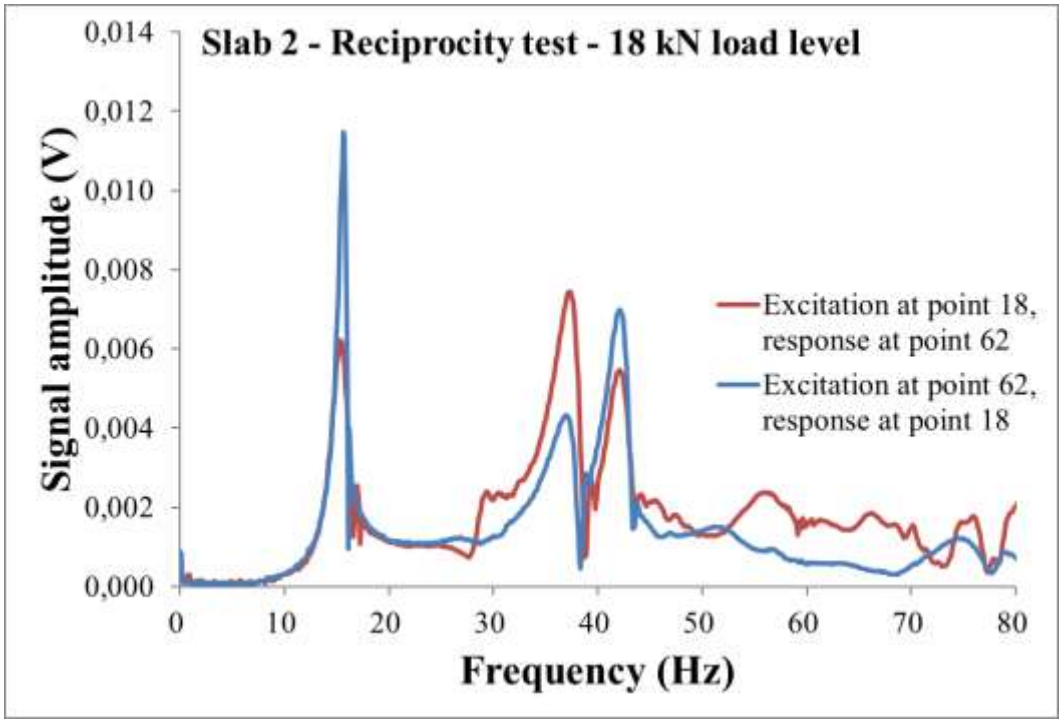

Figure 91 – Reciprocity test of S2 for 18 kN load level.

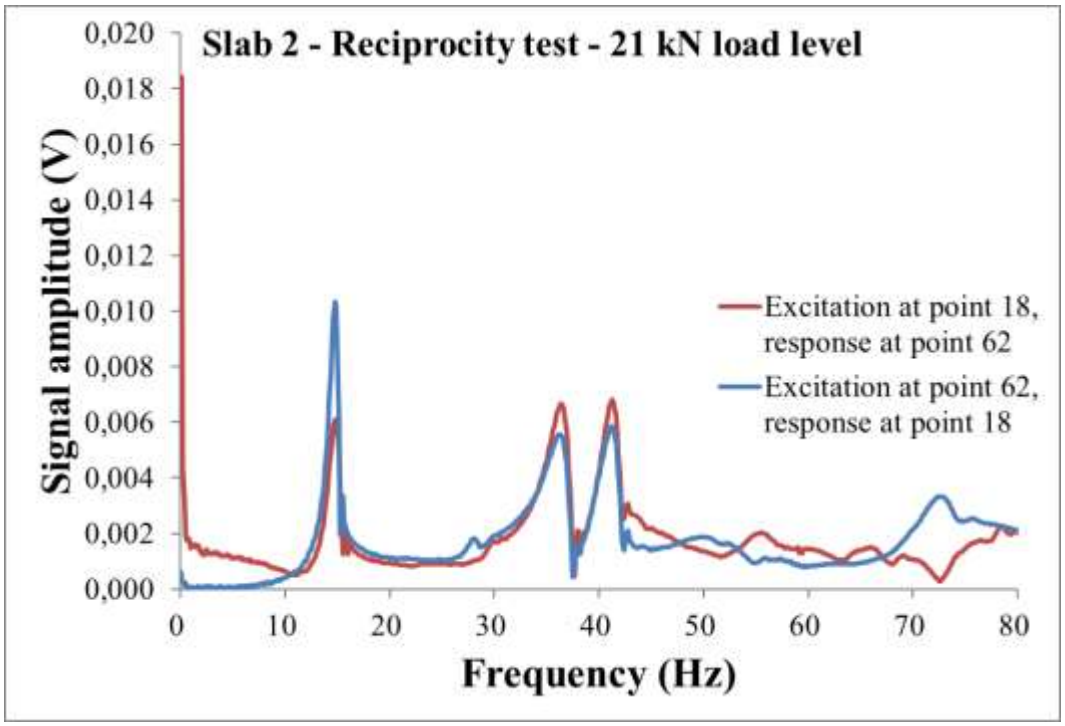

Figure 92 – Reciprocity test of S2 for 21 kN load level.

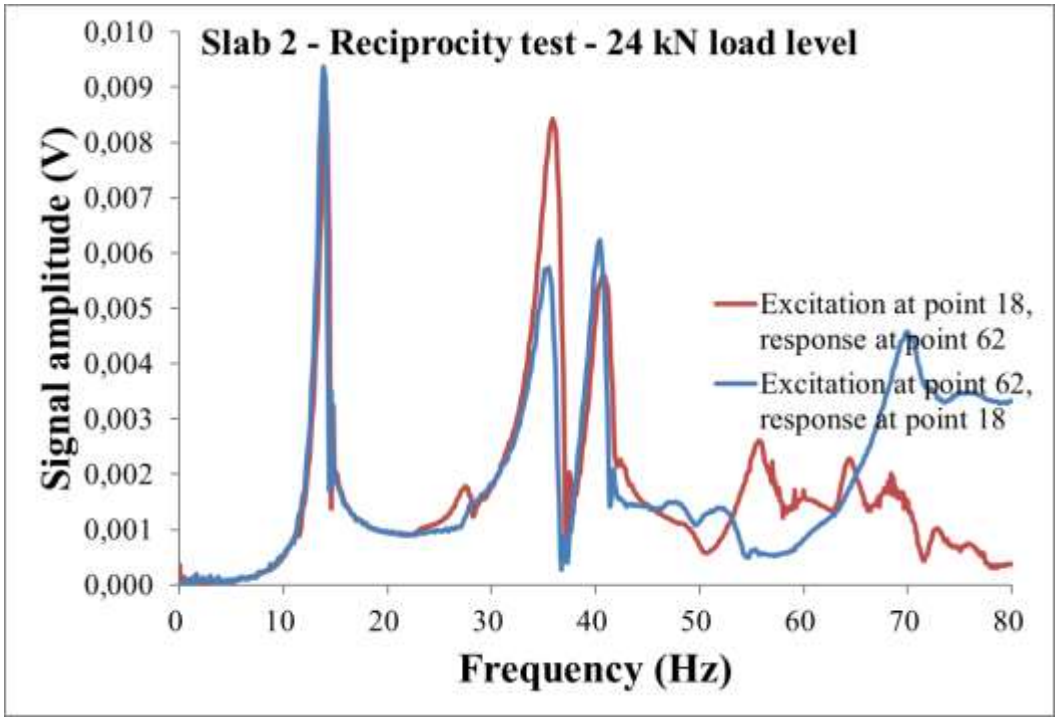

Figure 93 – Reciprocity test of S2 for 24 kN load level..

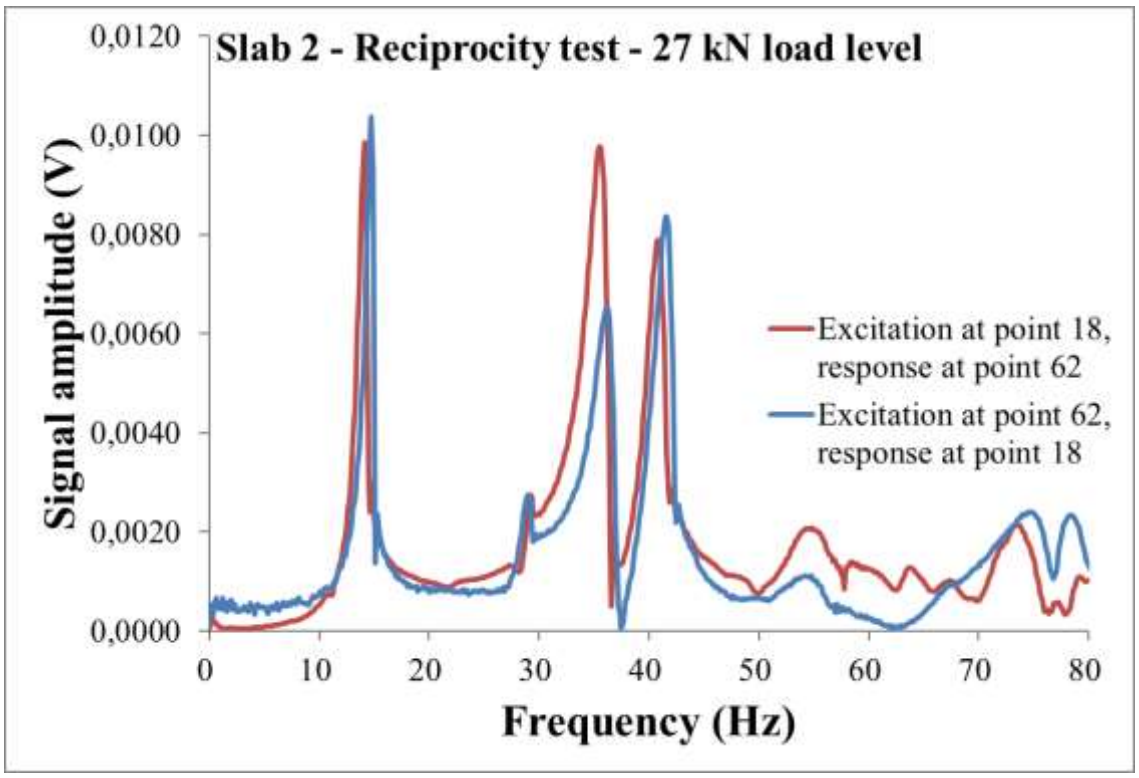

Figure 94 – Reciprocity test of S2 for 27 kN load level.

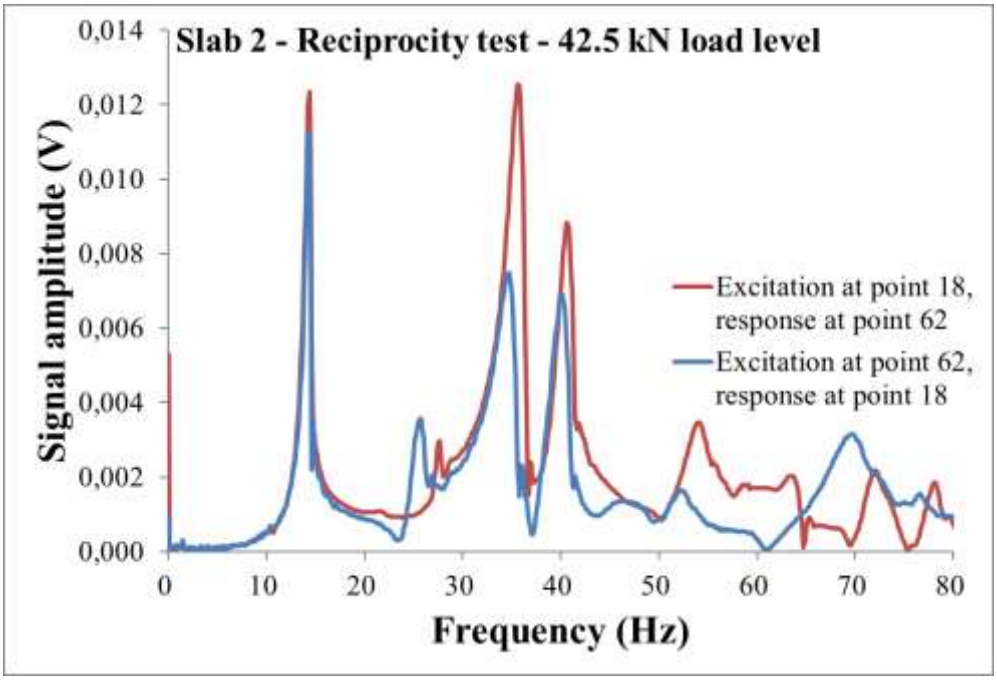

Figure 95 – Reciprocity test of S2 for 42.5 kN load level.

For linearity tests, it could be observed that an agreement at peaks of frequencies remained as damage increased but between peaks the divergence remained (Figures 96 to 98). For S2, linearity test showed that there was a better superposition of the signals in comparison to S1 (superposition in magnitude and frequency), while S1 had different peak magnitude and frequency shift.

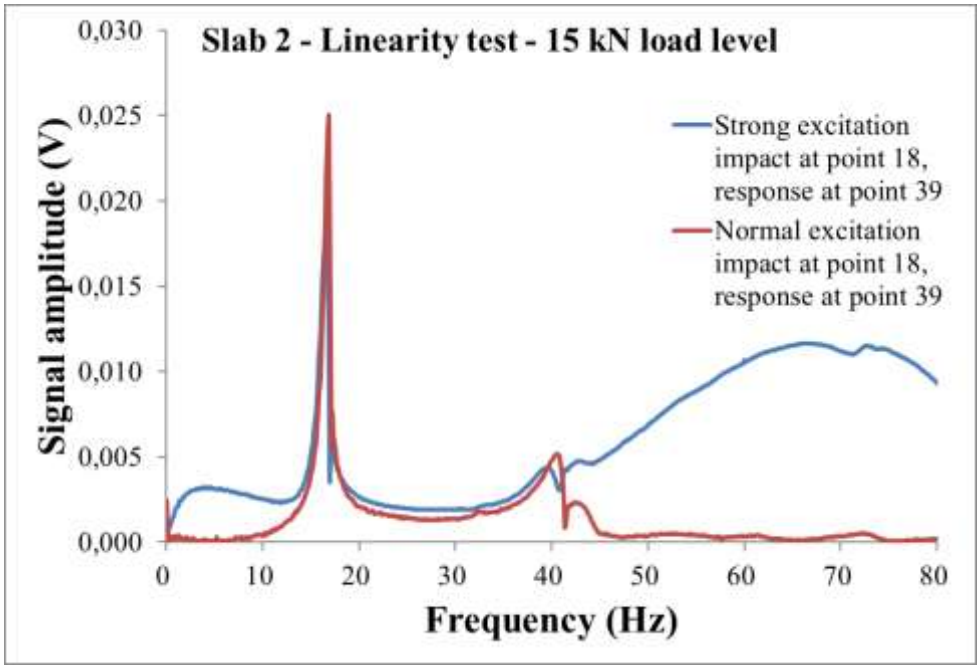

Figure 96 – Linearity test of S2 for 15 kN load level.

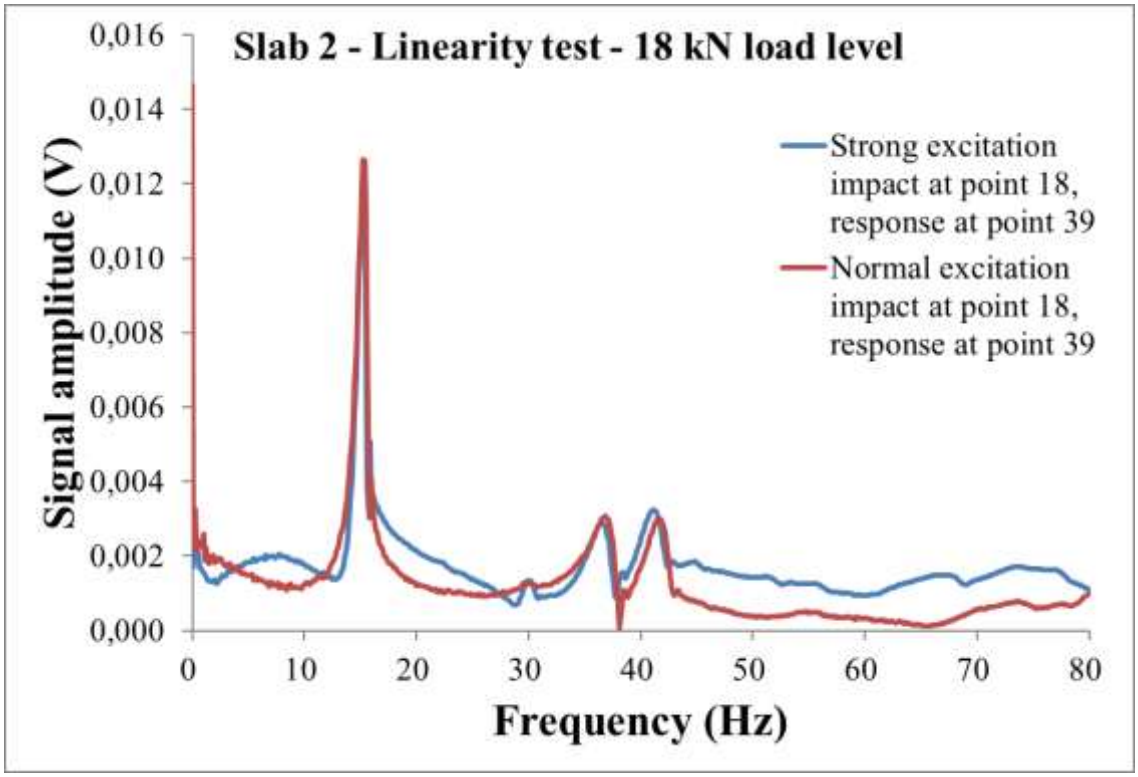

Figure 97 – Linearity test of S2 for 18 kN load level.

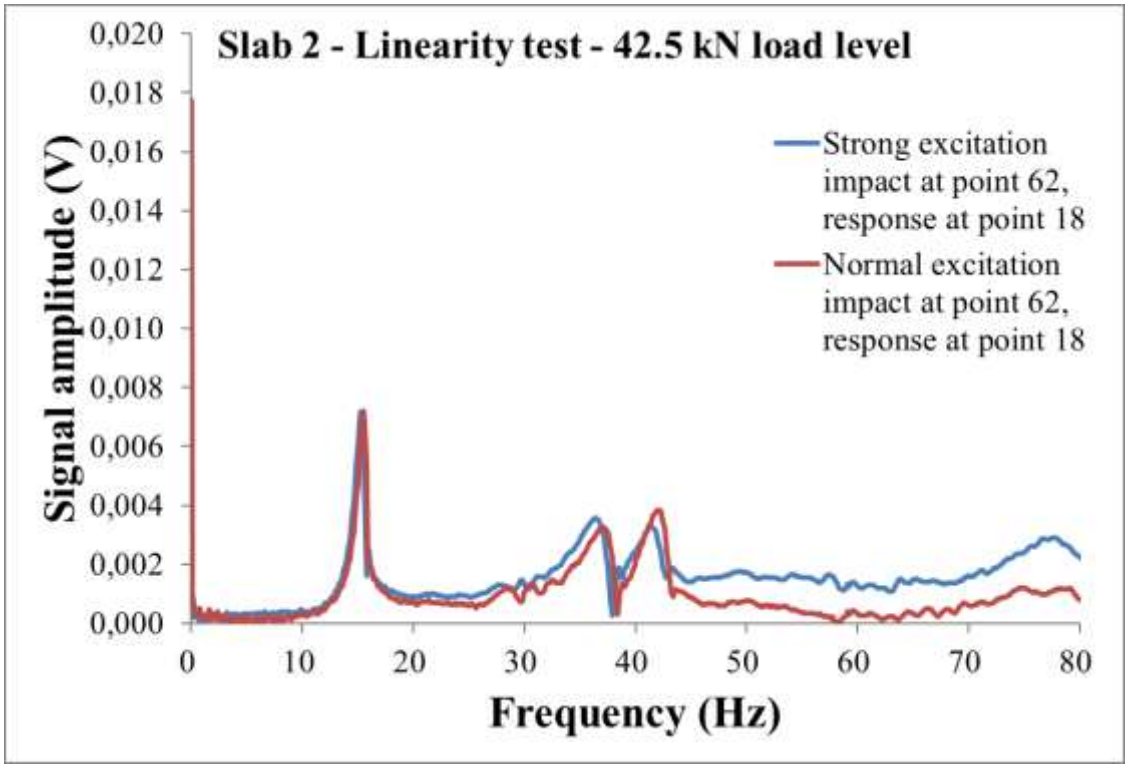

Figure 98 – Linearity test of S2 for 42.5 kN load level.

After the whole modal testing, the frequencies of interest were obtained. The three initial natural frequencies are listed in Tables 7 and 8. The results shown in Table 7 were initially obtained by Guedes (2016) but an incorrect frequency value was detected after data reprocessing, so Table 7 presents the correct values. In both slabs, the first and third experimental frequencies were the first and second of bending, respectively. The second experimental mode was the first torsional. This can be seen in Figures 99 and 100.

S1 - Evolution of frequencies to load level					
Frequency Mode (experimental)	**LOAD LEVEL (kN)**				
	0	**8**	**16**	**22**	**24**
1st	16.60	15.92	11.58	11.13	COLLAPSE
2nd	33.36	31.17	32.44	32.46	
3rd	58.63	55.53	49.33	47.87	

Table 7 – Evolution of natural frequencies in S1 from modal testing

S2 - Evolution of frequencies to load level (driving point 18)												
Frequency Mode (experimental)	**LOAD LEVEL (kN)**											
	0	**3**	**6**	**9**	**12**	**15**	**18**	**21**	**24**	**27**	**42,5**	**62,5**
1st	19,06	18,81	18,77	18,70	18,68	16,62	14,02	15,15	14,15	14,62	15,22	COLLAPSE
2nd	33,25	32,37	31,98	32,46	31,63	30,26	29,87	28,33	36,03	29,06	28,29	
3rd	43,92	43,50	43,32	42,74	42,69	42,50	39,72	38,32	40,57	36,97	37,58	

Table 8 – Evolution of natural frequencies in S2 from modal testing

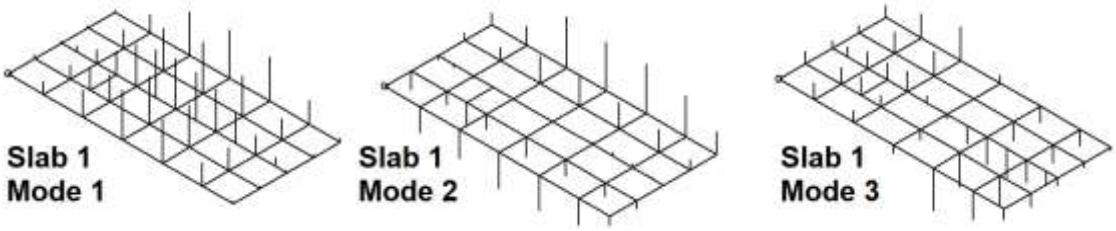

Figure 99 – Mode shapes of S1 for 0kN load level.

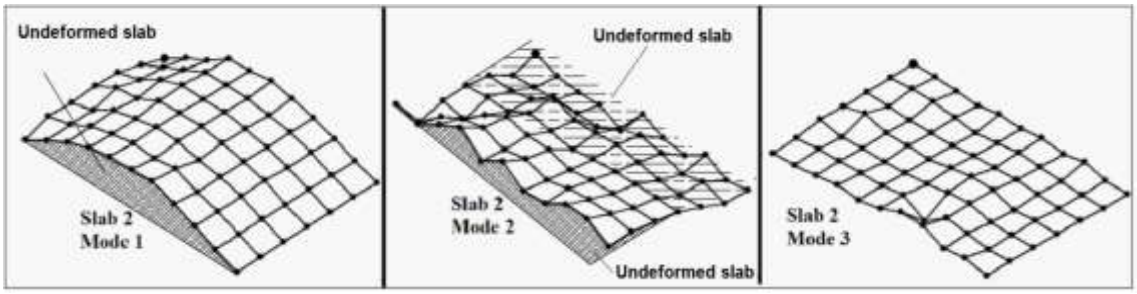

Figure 100 – Mode shapes of S2 for 0kN load level.

4.2.3. Cracking and natural frequency

The pattern of cracking for both slabs are shown in Figures 101 and 102, until near or at the collapse. In order to compare both slabs, the same applied load levels were adopted. A difference is observed in the crack intensity in early load levels (33% of collapse load), in which S2 showed a much severe crack rise. Both slabs S1 and S2 have transverse reinforcement, but with different ratio. As explained by Pillai and Menon (2005), while beams on bending moments tend to deform to a trapezoid (as exaggeratedly shown in Figura 103-a) due to Poisson effect (so the hypothesis of plane section is not strictly right), one-way slabs are restrained laterally, what generates secondary moments that are resisted by transverse reinforcement, as shown in Figure 103-b. The difference in the ratio used in both elements can be a cause for the difference in the cracking pattern. Change on reinforcement is a factor that can cause variation in cracking pattern. Han (2011) evaluated the influence of transverse reinforcement spacing on the cracking behavior in slab strips through a proposed model and compared it to the values predicted by standard DIN1045. Other evaluation of transverse reinforcement spacing effects on cracks in one-way and two-way slabs can be found in Han et al (2011). Gurutzeaga et al (2015) evaluated the influence of the bottom transverse reinforcement and longitudinal bar spacing in one-way slabs and beams subjected to shear and concluded that slabs with a large longitudinal bar spacing show a less rigid load-deformation behaviour.

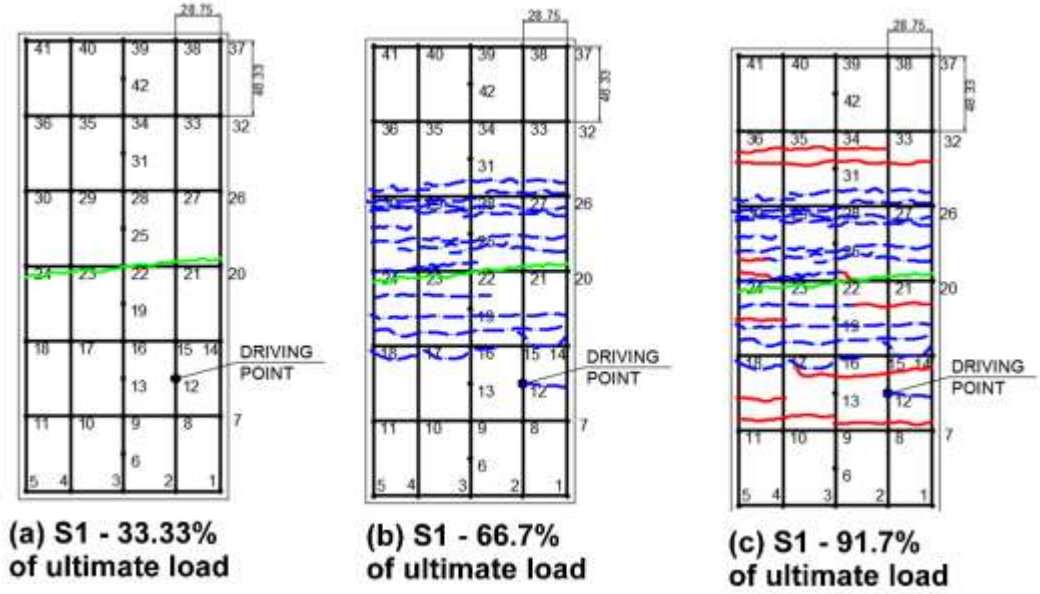

Figure 101 – Cracking evolution in S1 for (a) 33,3%, (b) 66,7% and (c) 91,7% of ultimate load

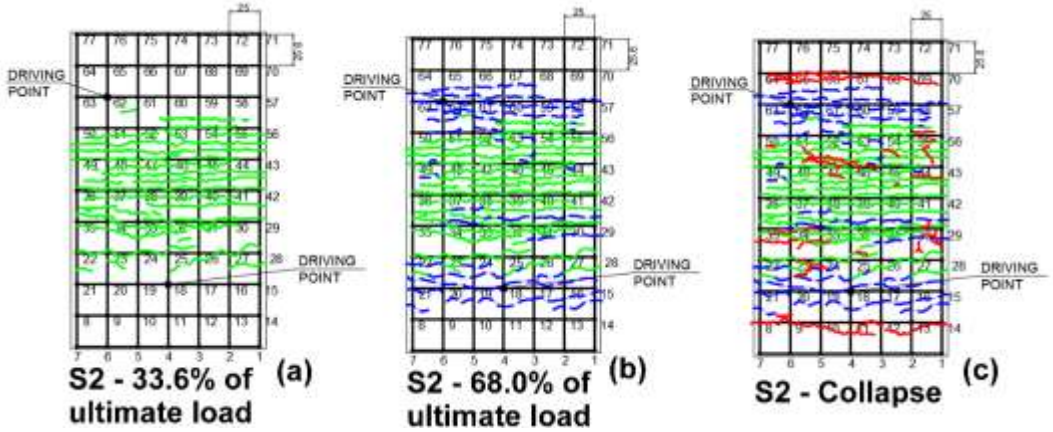

Figure 102 – Cracking evolution in S2 for (a) 33,6%, (b) 68% and (c) ultimate load

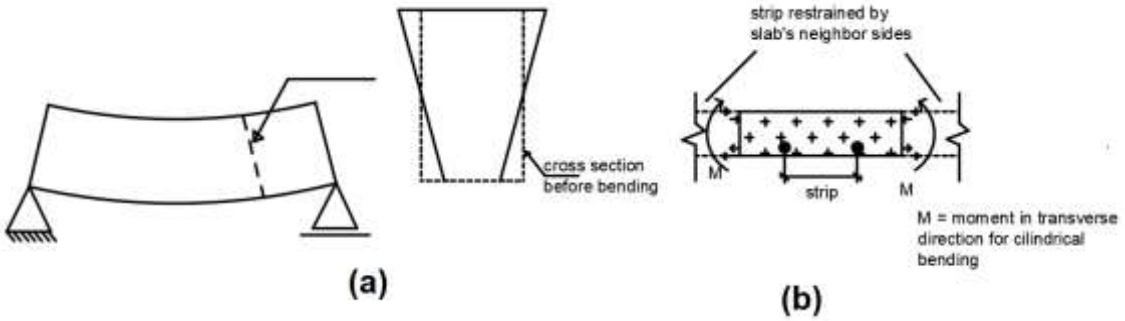

Figure 103 – Bending in (a) rectangular beam and (b) one-way slab.

The fundamental natural frequencies of uncracked and cracked slabs are shown in Figure 104 as a function of the percentage of collapse load, and thus, the crack level. There is a decrease in the first natural frequency of S1, as observed in several tested RC elements (Pesic et al., 2015). The behaviour of S2 is similar to S1 up to 40% of collapse load; after that, it showed an almost steady value of natural frequency until 70% of collapse load. It was not possible to carry on measurements at high levels of load for this slab due to a testing problem. However, since cracking reduces the stiffness of the slab and thus its natural frequency, it can be seen that the changes of natural frequency in each slab are consistent with its respective cracking pattern. This is because the cracking intensity is much higher in S2 than in S1 for low percentage levels of applied load. S2 also has a variation of natural frequency to damage that resembles the behaviour observed in Hamad et al. (2014), in which the fundamental natural frequency stabilized after 60% of collapse load.

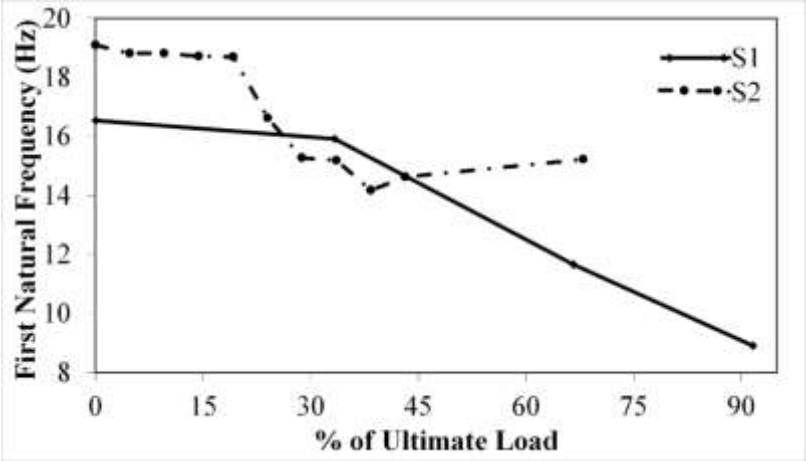

Figure 104 – Natural frequency versus percentage of ultimate load

4.2.4. Gradient of natural frequency

Natural frequencies grew along the decay of response after impact excitation, as the cracks initially opened tend to close with the reduction of vibration level. This made it possible to obtain curves of variation of natural frequency along the decay. For a given modal test, since the level of vibration differed among different test points, first each response signal had a decay interval selected for further processing, in order to keep constant the amplitude of the first cycle of vibration among the signals. In sequence, the natural frequency was calculated for each vibration cycle; a curve was then obtained when plotting the natural frequency against the cycle number. Linear regression was then applied, and a gradient was obtained from the curve. This procedure

was repeated for several test points in each cracking stage, and then an average regression line was produced for that stage of induced cracking. Finally, in order to better compare frequency regression lines from different cracking conditions, each average regression line was replotted employing relative frequency values, which were obtained by taking the ratio of the instantaneous natural frequency and the maximum natural frequency observed in that respective regression line. The value of the gradient of each final average regression line representative of a cracking condition was calculated and plotted in Figure 105, against the percentage of ultimate load applied to induce cracking in the respective slab.

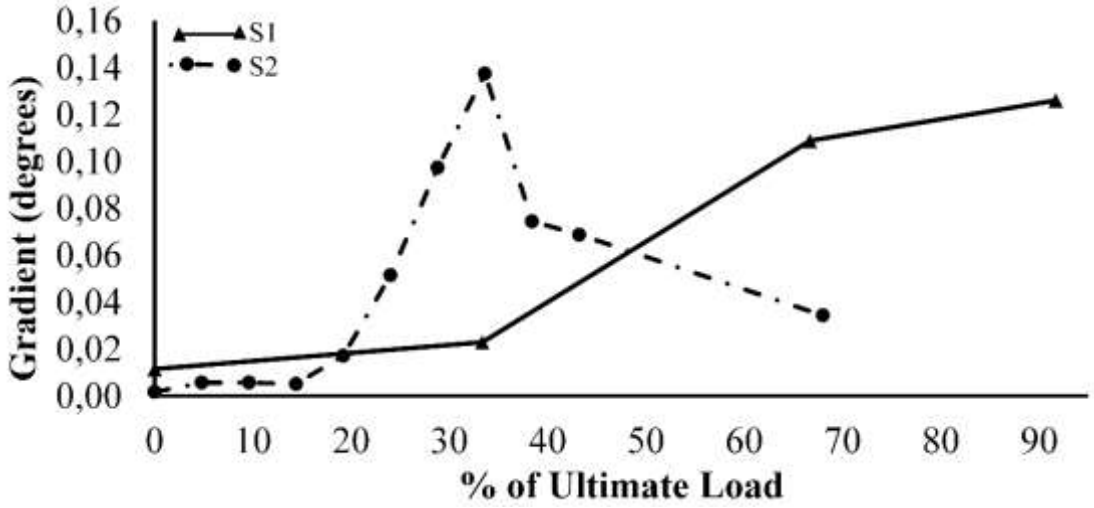

Figure 105 – Gradient of frequency regression lines versus percentage of ultimate load

The pattern of changes of the gradient in S2 is in accordance with results obtained for beams tested in similar conditions by Neild et al. (2003) and Wang et al. (2012), who observed that the gradient grew until an intermediate level of damage and then decreased. Herein, the growth of the gradient occurred for S2 until 33% of collapse load, and then reduced for the following load levels. However, for S1, there is growth of the gradient until near the collapse. A possible explanation for this difference would be a distinct balance between the existing breathing and open cracks in both slabs for a given percentage of collapse load, reminding that it is the breathing crack that causes the variation of natural frequency along the decay. Still regarding this, it could be argued that that amplitude dependent material behaviour would lead to changes in natural frequencies along the decay, independent of the cracking condition and even for

the uncracked state. This was already investigated (Pimentel et al., 2017) and it was shown that the gradient of time-frequency curves due to damage could be distinguished from other causes related to nonlinear behaviour of the tested slabs.

Reinforced concrete slabs can present a residual deflection after unloading and some of the cracks remain open, as noticed by Mahowald et al. (2010) in reinforced concrete slabs. However, it was not possible to quantify the number of open and breathing cracks for each cracking stage. On the other hand, a clue regarding the cracking behaviour could be made by plotting the total length of existing cracks versus the percentage of collapse load. This is shown in Figure 106 and it is possible to notice a difference in the behavior of the crack opening rate between the two slabs, from the slope of the curves. While S1 shows increasing slope (that is, crack rate) with damage level, S2 shows a decrease in crack rate. A probable cause of this difference in crack rate is that the S2 had more cracks for a lower percentage of collapse load when compared to S1. This can be visually confirmed (Figs. 101 and 102) from the different crack evolution pattern in both slabs. By considering that old cracks are wider than new cracks, the former tended to be of the open type, as opposite to new cracks that tended to be more of the breathing type. This way, S2 would have a greater incidence of open cracks for higher cracking levels than S1. This leads to a difference in nonlinear behavior between the two slabs, implying different behavior of the gradients of frequency, as seen in Figure 98. It should be noted that the behaviour of the gradient depicted in Figure 105 is consistent with the difference in cracking evolution between the two slabs shown in Figure 106.

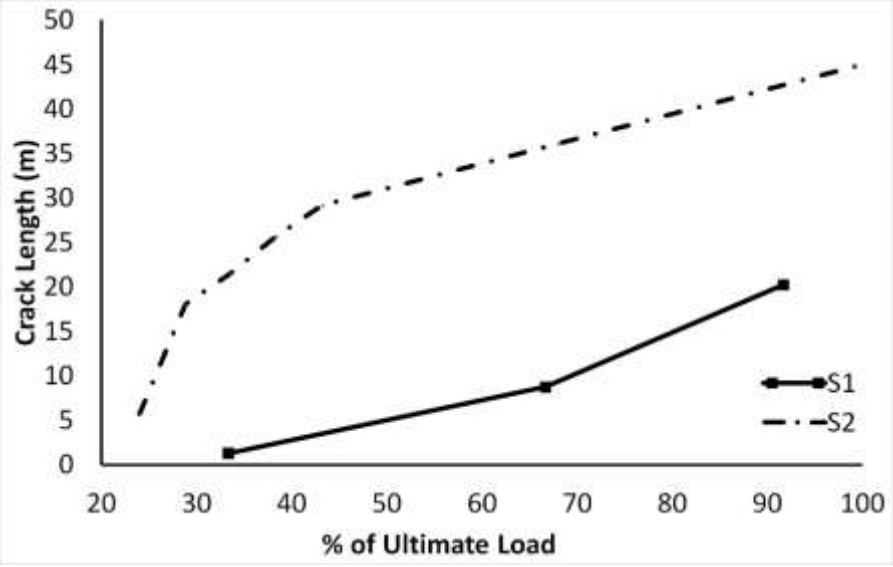

Figure 106 – Cracking evolution in S2 for (a) 33,6%, (b) 68% and (c) ultimate load

4.2.5. Gradient versus global damage index

It is possible to relate the gradient of the frequency-decay curves and a global damage index based on the variation of the fundamental natural frequency. Rodriguez-Gómes and Cakmak (1990) proposed a damage index based on the relationship between the changes of natural frequency at the beginning and ending of the decay. Pimentel et al. (2017) introduced a modification of this index (DI_m), shown in Equation 18, to make a comparison of the structural condition when cracked with its respective uncracked stage, by adopting the initial natural frequency w_o for the undamaged state, and the final natural frequency w_n as the natural frequency of damaged stage. These frequencies where obtained from processing the signals for each load stage, using StarModal software.

$$DI_m = 1 - (\frac{w_n}{w_0})^2 \quad (18)$$

The plot between the damage index DI_m and the gradient for both slabs is shown in Figure 107. While the index grows steadily with the increase of damage level for S1, the pattern on S2 is similar to S1 until a certain load level (corresponding to 33.6% of the collapse load), and after that the damage index stabilizes. Since natural frequencies did not show expressive change in S2 for higher levels of damage, there is no significant changes of its damage index, as expected, while the same natural frequencies decrease until the last load level for S1. On the other hand, for initial damage levels, the curves obtained for both slabs are very similar until a damage index DI_m around 0.3, what implies that both slabs had reduction of the frequency with the load level until this damage index value.

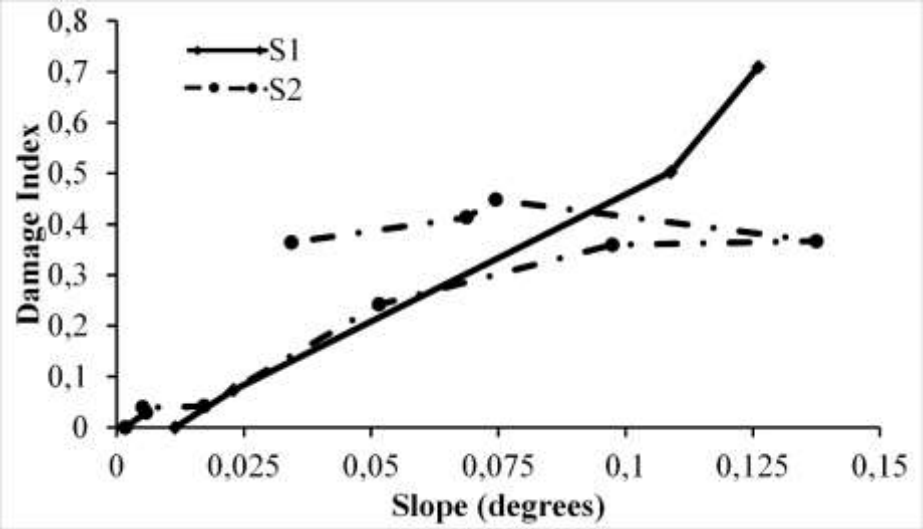

Figure 107 – Dim versus gradient for slabs 1 and 2

4.3. Numerical modeling: evaluation of numerical mesh

It can be argued the effect of the chosen mesh on MAC calculation since there is a direct relationship of both (Chen, Zhao and Makurat, 2000; Nefske and Sung, 1996). To investigate the effect of the mesh used in comparison to the experimental (gross) mesh, a new model was tested, were both frequencies and MAC were compared with the experimental data. In the new model named "R" (refined), each previous element of the current FE model was divided into 9 smaller elements. The results are shown in tables 9 to 12. In both slabs there is a numerical stabilization comparing the used mesh (U) to the refined mesh (R). For S1 the first frequency shows a decrease in the first frequency when the mesh is refined while the second and third frequencies remain stable. MAC values are not affected by refinement.

Load level (kN)	1st Frequency				2nd Frequency				3rd Frequency			
	M.A. (Hz)	E (Hz)	U (Hz)	R (Hz)	M.A. (Hz)	E (Hz)	U (Hz)	R (Hz)	M.A. (Hz)	E (Hz)	U (Hz)	R (Hz)
0	16,60	15,12	16,00	15,56	33,36	35,18	37,96	37,96	58,63	46,22	51,47	51,43
LEGEND	M.A. = modal analysis			Mesh	E = experimental mesh				U = used			
	N = numeric				R = refined mesh							

Table 9 – Comparison of frequencies of different model refinements for S1

Load level (kN)	MAC 1st Frequency			MAC 2nd Frequency			MAC 3rd Frequency		
	E	U	R	E	U	R	E	U	R
0	0,959	0,966	0,966	0,520	0,518	0,518	0,733	0,810	0,796
LEGEND	E = experimental mesh			U = used					
	R = refined mesh								

Table 10 – Comparison of MAC of different model refinements for S1

Load level (kN)	1st Frequency				2nd Frequency				3rd Frequency			
	M.A. (Hz)	E (Hz)	U (Hz)	R (Hz)	M.A. (Hz)	E (Hz)	U (Hz)	R (Hz)	M.A. (Hz)	E (Hz)	U (Hz)	R (Hz)
0	19,06	16,39	19,24	19,24	33,25	27,52	32,27	32,26	43,92	36,11	46,29	46,27
LEGEND	M.A. = modal analysis			Mesh	E = experimental mesh				U = used			
	N = numeric				R = refined mesh							

Table 11 – Comparison of frequencies of different model refinements for S2

Load level (kN)	MAC 1st Frequency			MAC 2nd Frequency			MAC 3rd Frequency		
	E	U	R	E	U	R	E	U	R
0	0,903	0,936	0,936	0,852	0,895	0,895	0,594	0,615	0,615
LEGEND	E = experimental mesh			U = used					
	R = refined mesh								

Table 12 – Comparison of MAC of different model refinements for S2

In the case of the cracked slabs, the effect of meshing refinement can be demonstrated in Figure 108, considering three adjacent elements in a slab with a crack in the center of the middle element. The area of influence of a crack, coming from its center, reach an area of three times the height of the slab (Figure 108-a). With refinement of mesh, the elements in the neighborhood of the element with crack can have a more realistic stifness variation based in Christides and Bar (1984) or Sinha (2002) models, as shown in Figure 108-b.

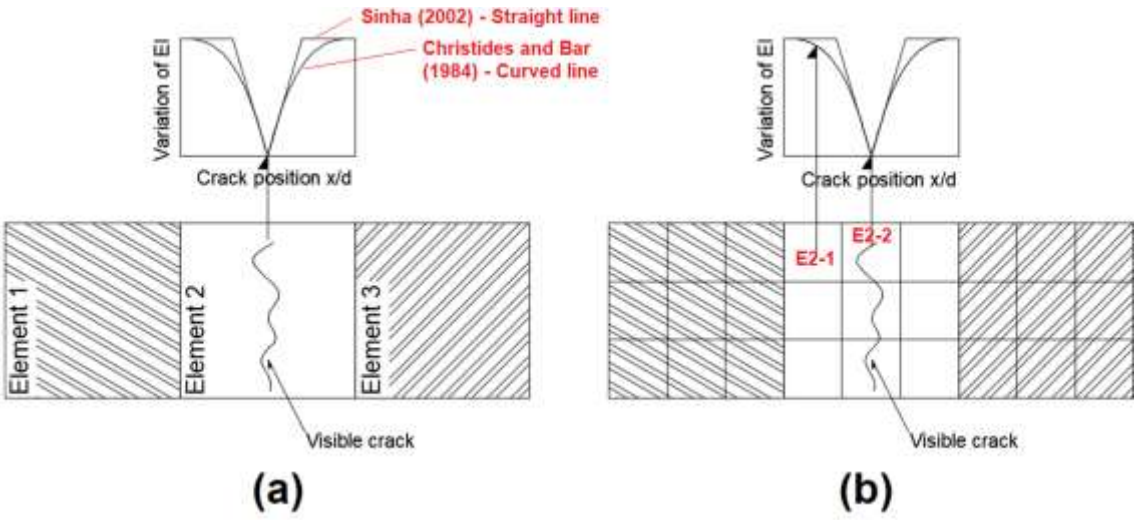

Figure 108 – Effect of mesh refinement in the use of stiffnes reduction rules

It must be mentioned that the used mesh was also tested for a load level with cracks and presented good results in frequency and mode shapes (through MAC indicator), what implies in an adequation of the adopted mesh.

4.4. Results from numerical modeling

For both the isotropic and orthotropic versions of Models 1 and 2, the frequencies, mode shapes and nodal displacement are obtained and compared with the experimental data. Reminding that in Model 1 the stiffness reduction was made based on the cracking moment and in Model 2 the stiffness reduction was made in the elements presenting cracks and the area of influence of these cracks. The first three frequencies were evaluated in both slabs, which were the first and third ones corresponding to the first and second modes in flexure, respectively, and the second frequency corresponding to the first torsional mode shape. Tables 13 to 18 shows the resulting frequencies obtained in both models for the two slabs. In the column named "% diff" it is shown the percentage of difference in frequency of that model to the reference value (experimental data). The frequencies of 0 kN are the same for Models 1 and 2 (isotropic and orthotropic) in both slabs because both considers the presence of load: Model 1 starts being applied after the cracking is reached (before this moment is achieved the stiffness reduction based on moment distribution is used, as illustrated in Figure 71) and Model 2 starts being applied for the first load level (8 kN in S1 and 15 kN in S2). It must be mentioned that the rule of trapezoid distribution of moment

(shown in Figure 71) remained in use for both models in the elements that did not reach the cracking moment (Model 1) or did not show visible cracks (Model 2). In S2 there was a frequency reduction until the first visible crack was seen and, to compute this decrease, the elastic module decrease (as Figure 70 shows) was applied in all the elements and remained in use even in the next load levels for the elements that did not show visible cracks. For Model 2, the same happened for the elements that did not have visible cracks or were not in the area of influence of a crack.

	S1								
1st Frequency	Load Level (kN)	Experimental results (Hz)	Model 1 (ACI)				Model 2 (Christides and Barr (1984))			
			ISO	% diff	ORTHO	% diff	ISO	% diff	ORTHO	% diff
	0	16,600	15,57	***6,23***	15,57	***6,23***	15,57	***6,23***	15,57	***6,23***
	8	15,920	12,97	***18,51***	*12,78*	***19,74***	13,62	***14,43***	13,58	***14,72***
	16	11,580	4,92	***57,50***	*4,82*	***58,40***	11,95	***-3,23***	11,87	***-2,51***
	22	11,130	4,05	***63,61***	*2,11*	***81,08***	10,34	***7,11***	10,24	***8,01***

Table 13 – First frequency in S1 for the two models

	S1								
2nd Frequency	Load Level (kN)	Experimental results (Hz)	Model 1 (ACI)				Model 2 (Christides and Barr (1984))			
			ISO	% diff	ORTHO	% diff	ISO	% diff	ORTHO	% diff
	0	33,360	37,97	***-13,81***	37,97	***-13,81***	37,97	***-13,81***	37,97	***-13,81***
	8	31,170	36,24	***-16,27***	37,00	***-18,70***	36,39	***-16,75***	37,12	***-19,10***
	16	32,440	24,76	***23,66***	24,21	***25,36***	34,82	***-7,34***	36,25	***-11,75***
	22	32,460	15,68	***51,69***	11,97	***63,13***	33,43	***-3,00***	35,36	***-8,93***

Table 14 – Second frequency in S1 for the two models

	S1								
3rd Frequency	Load Level (kN)	Experimental results (Hz)	Model 1 (ACI)				Model 2 (Christides and Barr (1984))			
			ISO	% diff	ORTHO	% diff	ISO	% diff	ORTHO	% diff
	0	58,630	51,475	***12,204***	51,475	***12,204***	51,475	***12,204***	51,475	***12,204***
	8	55,530	47,420	***14,605***	47,999	***13,562***	47,743	***14,023***	47,578	***14,320***
	16	49,660	28,055	***43,506***	31,626	***36,315***	43,893	***11,613***	43,596	***12,211***
	22	47,870	23,403	***51,111***	23,123	***51,696***	40,411	***15,582***	40,019	***16,401***

Table 15 – Third frequency in S1 for the two models

	S2									
	Load Level (kN)	Experimental results (Hz)	Model 1 (ACI)				Model 2 (Christides and Barr (1984))			
			ISO	% diff	ORTHO	% diff	ISO	% diff	ORTHO	% diff
1st Frequency	0	19,06	19,24	***-0,94***	19,24	***-0,94***	19,24	***-0,94***	19,24	***-0,94***
	3	18,81	19,01	***-1,05***	19,00	***-1,00***	19,01	***-1,05***	19,01	***-1,05***
	6	18,77	18,76	***0,07***	18,74	***0,17***	18,76	***0,07***	18,76	***0,07***
	9	18,70	18,49	***1,12***	18,46	***1,27***	18,49	***1,12***	18,49	***1,12***
	12	18,68	18,21	***2,54***	18,17	***2,74***	18,21	***2,54***	18,21	***2,54***
	15	16,62	17,00	***-2,26***	16,90	***-1,67***	17,37	***-4,49***	17,35	***4,39***
	18	14,02	14,95	***-6,63***	14,77	***-5,34***	16,33	***-16,50***	16,35	***16,60***
	21	15,15	14,84	***2,05***	14,64	***3,39***	15,89	***-4,90***	15,44	***1,88***
	24	14,15	12,34	***12,79***	12,07	***14,71***	15,36	***-8,52***	15,32	***8,29***
	27	14,65	11,24	***23,27***	10,87	***25,82***	14,61	***0,26***	14,58	***-0,46***
	42,5	15,22	9,12	***40,09***	8,96	***41,16***	13,70	***10,00***	13,71	***-9,95***

Table 16 – First frequency in S2 for the two models

	S2									
	Load Level (kN)	Experimental results (Hz)	Model 1 (ACI)				Model 2 (Christides and Barr (1984))			
			ISO	% diff	ORTHO	% diff	ISO	% diff	ORTHO	% diff
2nd Frequency	0	33,25	32,27	***2,95***	32,27	***2,95***	32,27	***2,95***	32,27	***2,95***
	3	32,37	32,41	***-0,14***	32,18	***0,57***	32,41	***-0,14***	32,18	***0,57***
	6	31,98	32,01	***-0,08***	32,09	***-0,35***	32,01	***-0,08***	32,09	***-0,35***
	9	32,46	31,86	***1,85***	32,00	***1,42***	31,86	***1,85***	32,00	***1,42***
	12	31,63	31,71	***-0,25***	31,90	***-0,84***	31,71	***-0,25***	31,90	***-0,84***
	15	30,26	31,42	***-3,82***	31,65	***-4,60***	31,43	***-3,87***	31,73	***4,84***
	18	29,87	30,62	***-2,52***	31,09	***-4,08***	31,10	***-4,10***	31,43	***5,23***
	21	28,33	30,52	***-7,73***	31,04	***-9,56***	30,77	***-8,62***	31,20	***10,13***
	24	36,03	29,56	***17,97***	30,40	***15,62***	30,36	***15,73***	30,94	***-14,12***
	27	29,06	28,68	***1,30***	29,71	***-2,24***	29,94	***-3,03***	30,68	***5,57***
	42,5	28,29	26,15	***7,58***	28,18	***0,39***	29,61	***-4,68***	30,25	***6,94***

Table 17 – Second frequency in S2 for the two models

	S2								
	Load Level (kN)	Experimental results (Hz)	Model 1 (ACI)				Model 2 (Christides and Barr (1984))			
			ISO	% diff	ORTHO	% diff	ISO	% diff	ORTHO	% diff
3rd Frequency	0	43,92	46,29	***-5,40***	46,29	***-5,40***	46,29	***-5,40***	46,29	***-5,40***
	3	43,50	46,13	***-6,03***	46,14	***-6,06***	46,13	***-6,03***	46,14	***-6,06***
	6	43,32	45,95	***-6,07***	45,98	***-6,13***	45,95	***-6,07***	45,98	***-6,13***
	9	42,74	45,76	***-7,07***	45,80	***-7,16***	45,76	***-7,07***	45,80	***-7,16***
	12	42,69	45,56	***-6,72***	45,61	***-6,84***	45,56	***-6,72***	45,61	***-6,84***
	15	42,50	44,97	***-5,80***	45,03	***-5,96***	45,17	***-6,28***	45,21	***6,39***
	18	39,72	43,71	***-10,04***	43,77	***-10,20***	44,56	***-12,18***	44,66	***12,43***
	21	38,32	43,61	***-13,80***	43,67	***-13,97***	44,01	***-14,85***	44,10	***15,09***
	24	40,57	41,54	***-2,39***	41,49	***-2,27***	43,55	***-7,35***	43,68	***7,66***
	27	36,97	39,57	***-7,03***	38,91	***-5,25***	42,77	***-15,67***	42,88	***15,98***
	42,5	37,58	34,19	***9,03***	34,30	***8,73***	42,68	***-13,58***	41,68	***10,92***

Table 18 – Third frequency in S2 for the two models

Plotting the results in frequency gives the reader a better overall view about the differences between the four models (isotropic for Models 1 and 2 and orthotropic for Models 1 and 2). For S1 (Figures 109 to 111), Model 2 produces better results than Model 1 for the first three modes. While there is a good visual correspondence for the first frequency in Model 2, there is a positive difference of frequency for the second one and a negative difference for the third frequency. The use of a higher reduction of local stiffness for Model 2 would decrease the difference for the second frequency but would increase it for the first and third modes. Model 1, on the other hand, produces growing discrepant results for higher load levels. For S2 (Figures 112 to 114), Model 2 produced better results than Model 1, similarly to what was observed in S1. The reason why Model 1 was not adequate is because it penalizes cracked and uncracked elements in the same way and do not considers that some elements can reach cracking moment without the presence of visible cracks. Model 2, in a different approach, considered the peculiarities given by each crack in the element it appeared and in its neighborhood. Finally, in both slabs, there was no considerable diference between isotropic and orthotropic elements for the same model.

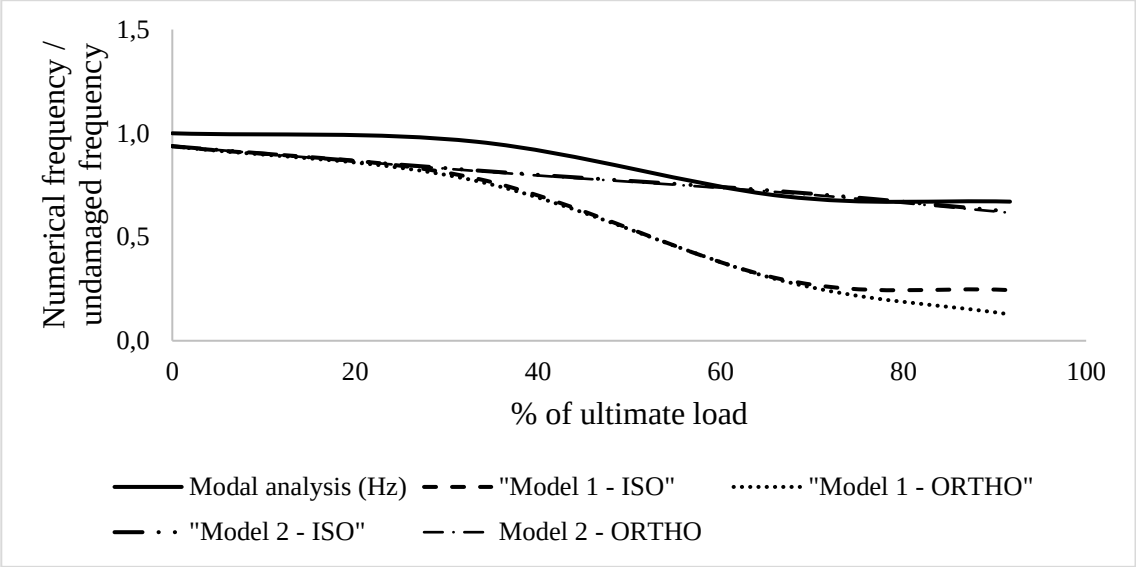

Figure 109 – Comparison of first frequency in S1 for the four numerical models used

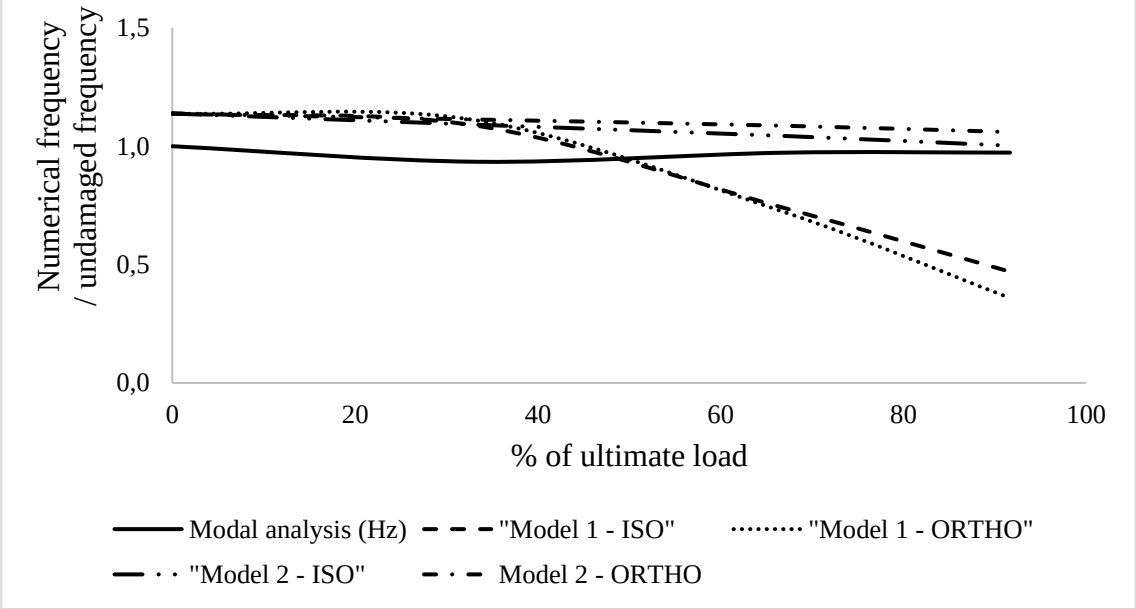

Figure 110 – Comparison of second frequency in S1 for the four numerical models used

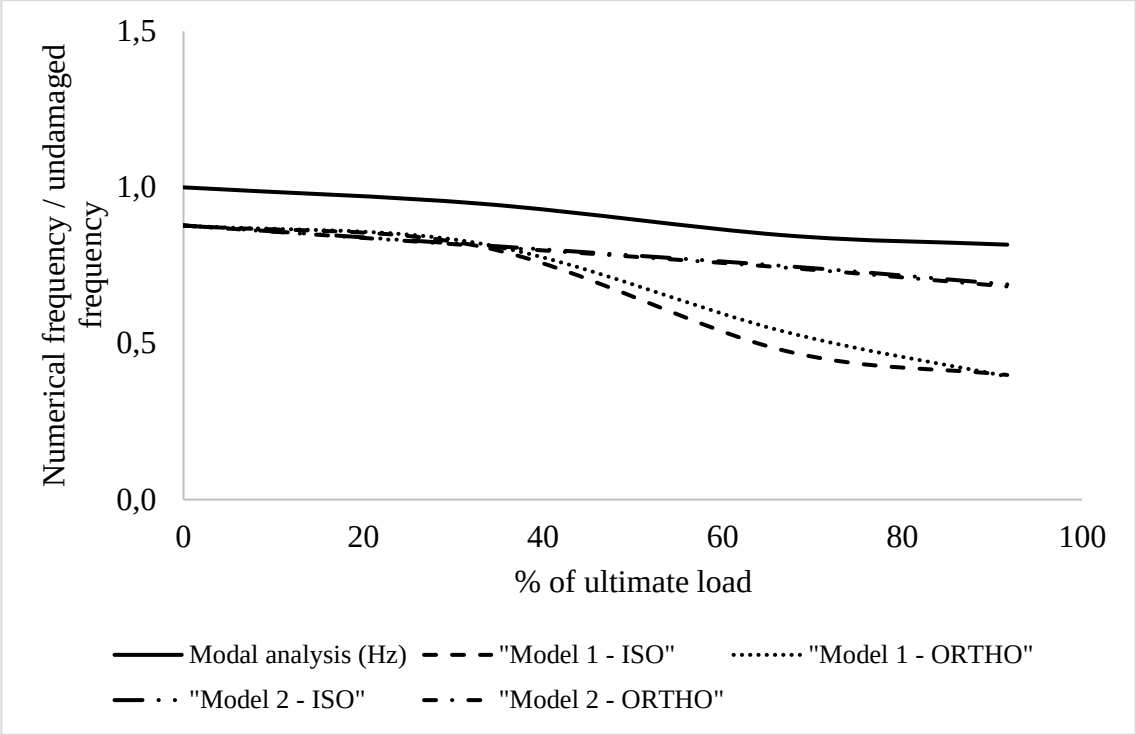

Figure 111 – Comparison of third frequency in S1 for the four numerical models used

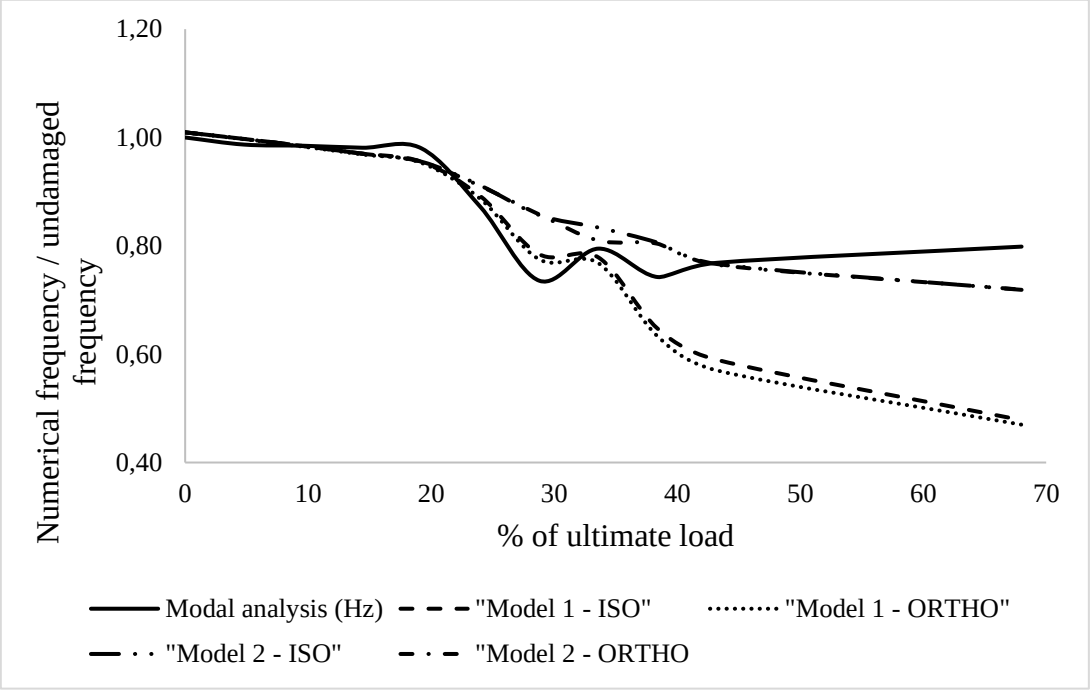

Figure 112 – Comparison of first frequency in S2 for the four numerical models used

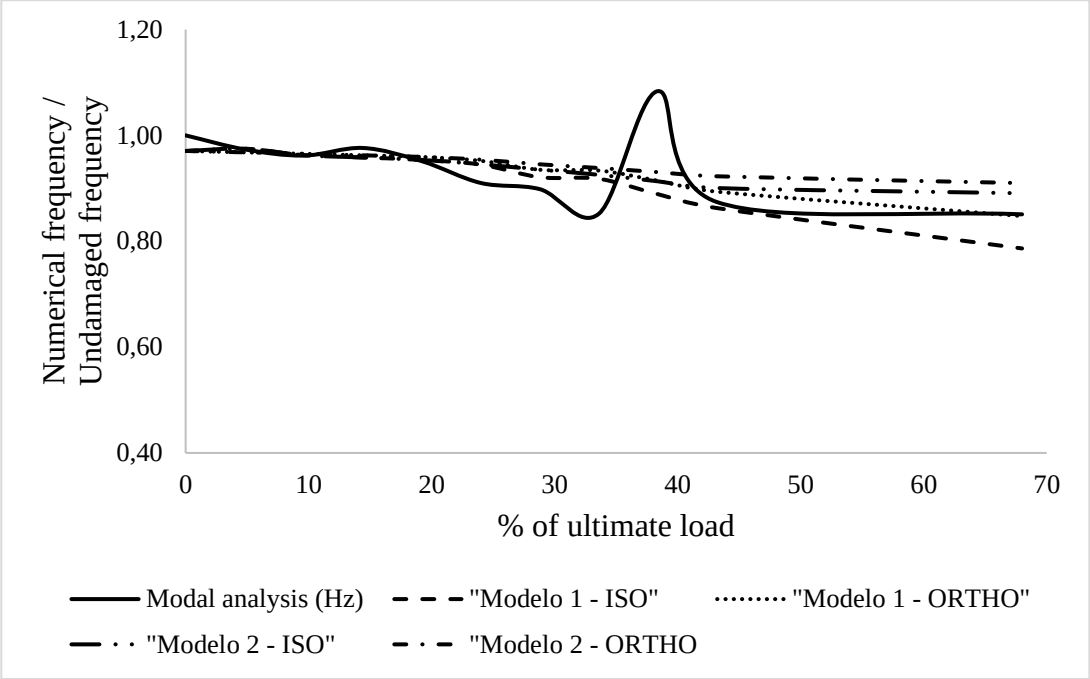

Figure 113 – Comparison of second frequency in S2 for the four numerical models used

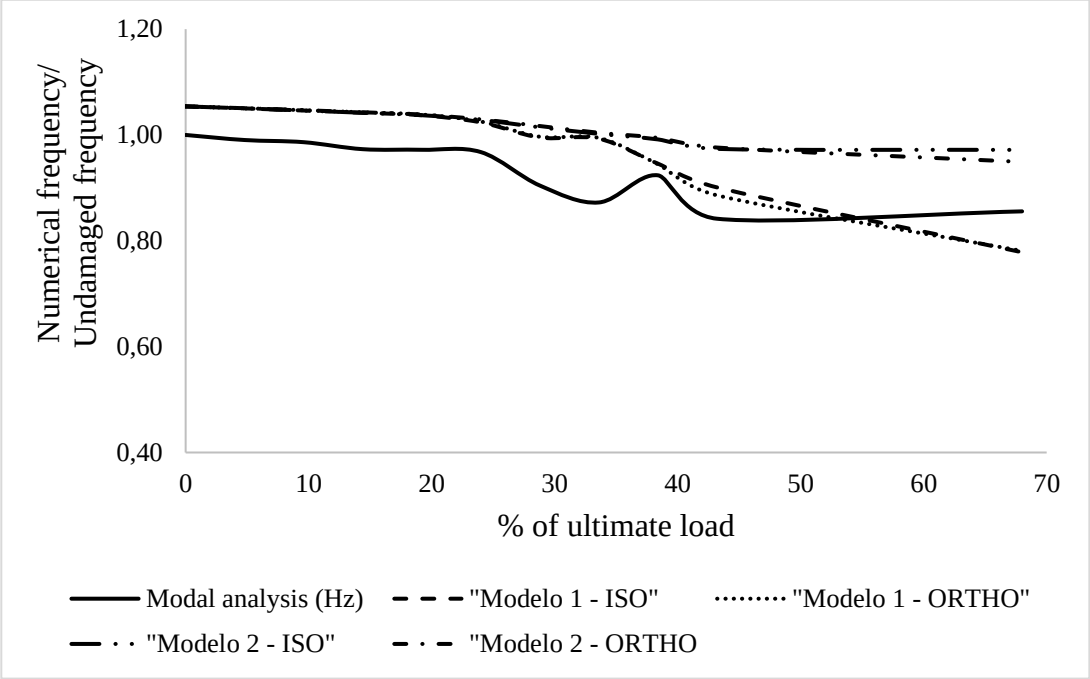

Figure 114 – Comparison of third frequency in S2 for the four numerical models used

The comparison of frequency can be associated with other modal properties. Since damage affects mode shapes, these can be used to evaluate the correlation between experimental and numerical models using MAC (Ngan, Caprani and Bai, 2019; Pérez and Serra-López, 2019). For S1, the MAC for the first mode remain similar in the four models tested (Figure 115) while MAC for second and third modes for Model 1 at

load levels of 16 kN and 22 kN are lower than respective levels for Model 2 (Figures 116 and 117), which is in agreement with was was observed for frequency results.

For S2 a first observation must be made: two driving points were used in this structure while only one was available for S1. Based on the position of these excitation points (nodes 18 and 62 in the experimental mesh as shown in Figure 13) and considering that the second frequency measured was the first of torsion (according to the modal testing), the experimental data of driving point 18 was used to evaluate the MAC of first and third modes while the data of driving point 62 was used to evaluate the second vertical mode shape. As the results shows (Figure 118) the compasiron of isotropic and orthotropic models shows no significant difference for the first frequency, as was observed in S1. For the second frequency (Figure 119), the most visible difference among modes occur in the two final load levels, what indicates that the model based on inertia changes (Model 1) can reproduce the mode of torsion in a similar way of Model 2. A decrease in MAC at the load level of 24 kN in the second frequency in comparison to the tendency observed in the previous and next load levels seems to be a problem in experimental data. For the third frequency (Figure 120), similar results are also seen between the four models and a reduction in the load level of 12 kN (in comparison to the observed tendency) indicates problem in experimental data. Although the correspondence in frequency was poor for Model 1 in S2, the MAC index had similar results for the three frequencies evaluates (differently from S1 results). This could be due to the influence of the different cracking pattern of both slabs (S2 had more cracks in the area between the load lines).

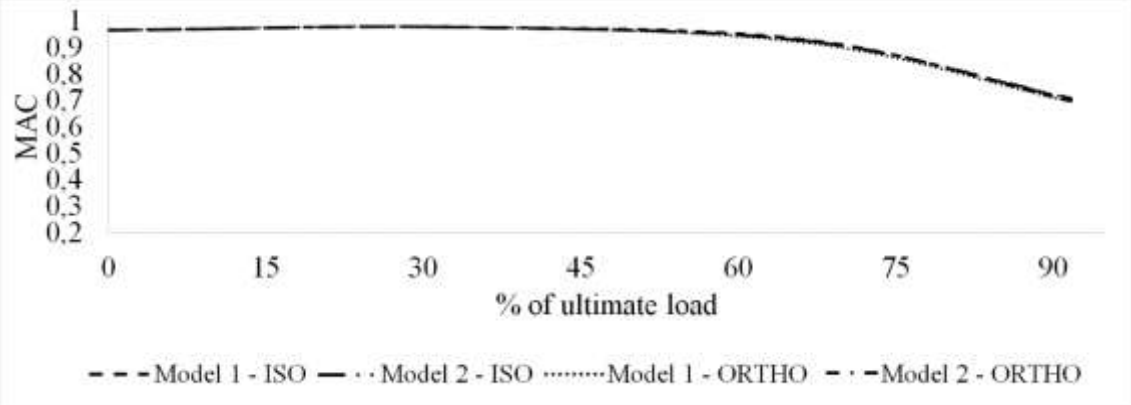

Figure 115 – MAC evolution for different models of S1 for the first frequency

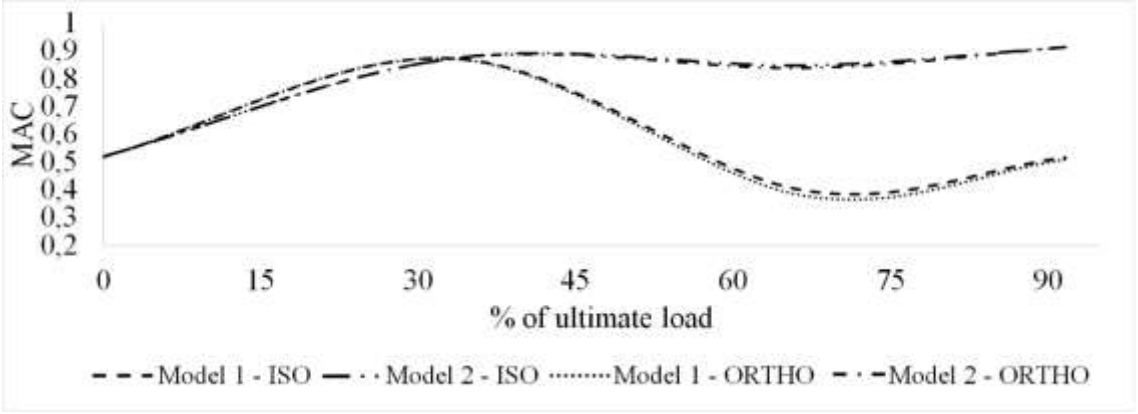

Figure 116 – MAC evolution for different models of S1 for the second frequency

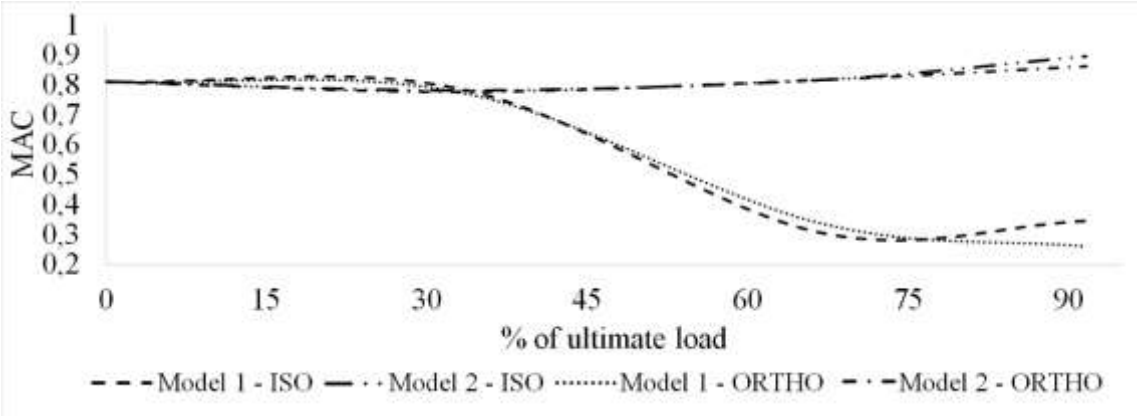

Figure 117 – MAC evolution for different models of S1 for the third frequency

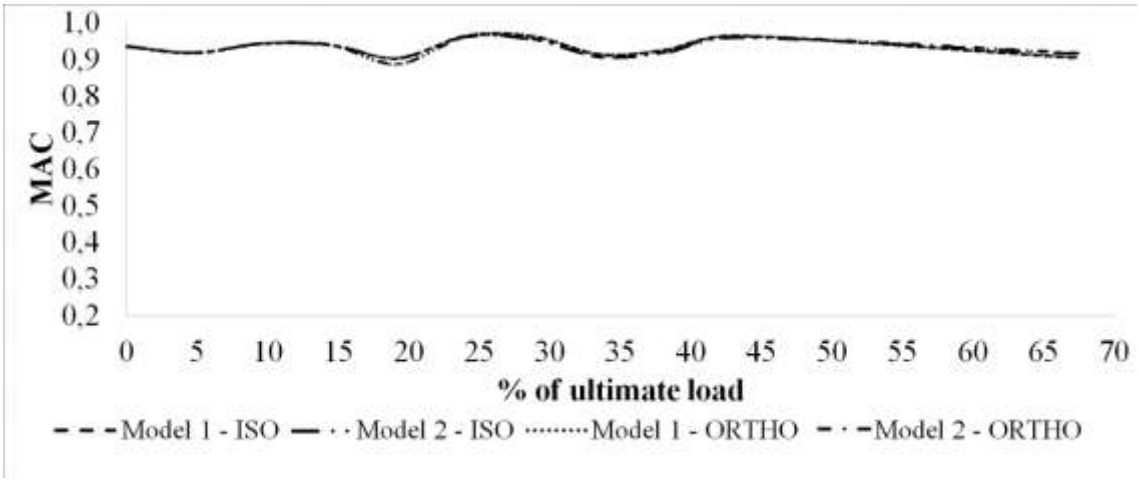

Figure 118 – MAC evolution for different models of S2 for the first frequency

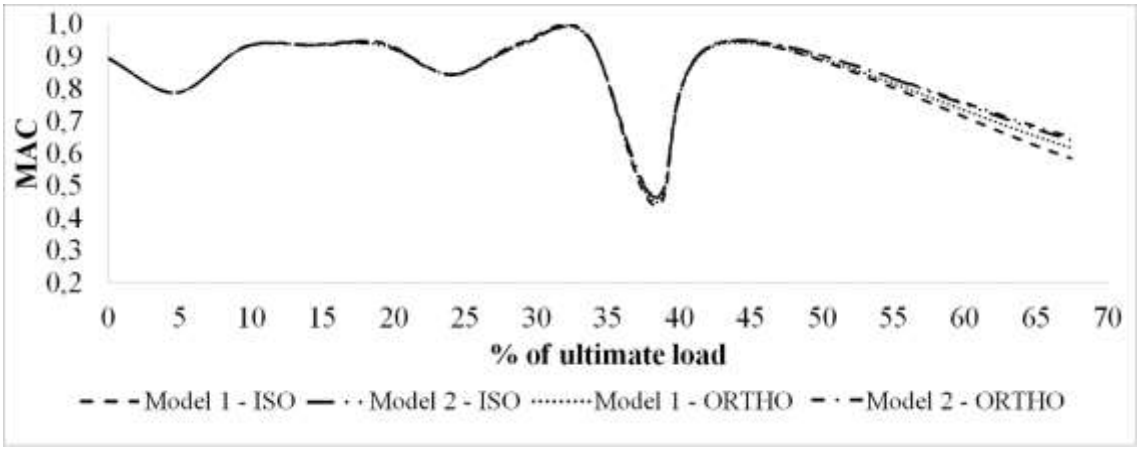

Figure 119 – MAC evolution for different models of S2 for the second frequency

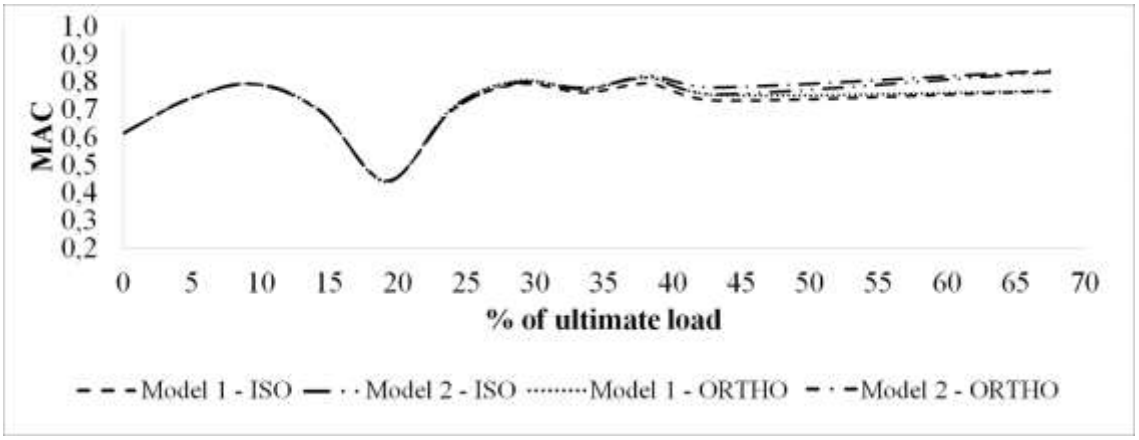

Figure 120 – MAC evolution for different models of S2 for the third frequency

4.5. Evaluation of slope of deflection

Reinforced concrete is a nonlinear material, what can be confirmed by the changes of slope in stress-strain curves due to several loading and unloading stages, leaving residual strain (ε_r), as shown in Figure 121. Taking, for example, the load-deflection curve for 15 kN load level of S2 (Figure 122), it is possible to see that there are two slopes in loading and one in unloading stage. Comparing the slopes of loading (m1-a) and unloading (m2) for the same loading level (Figures 123 to 129), the proximity of the values in an indication that, although the numerical models of both slabs were constructed for the unloading situation (m2 slope) (since the modal testing was applied after the removal of the load), it also applies for the loading case.

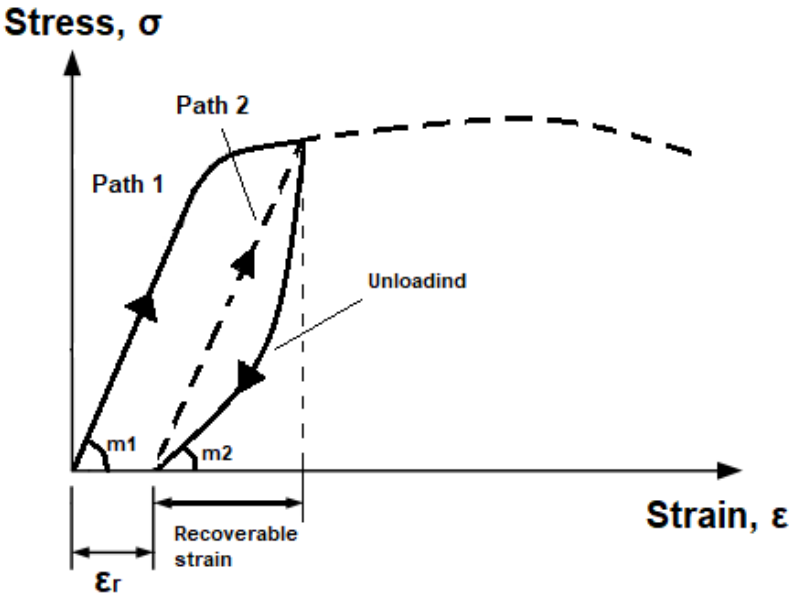

Figure 121 – Stress strain behavior for concrete at load-unload stages

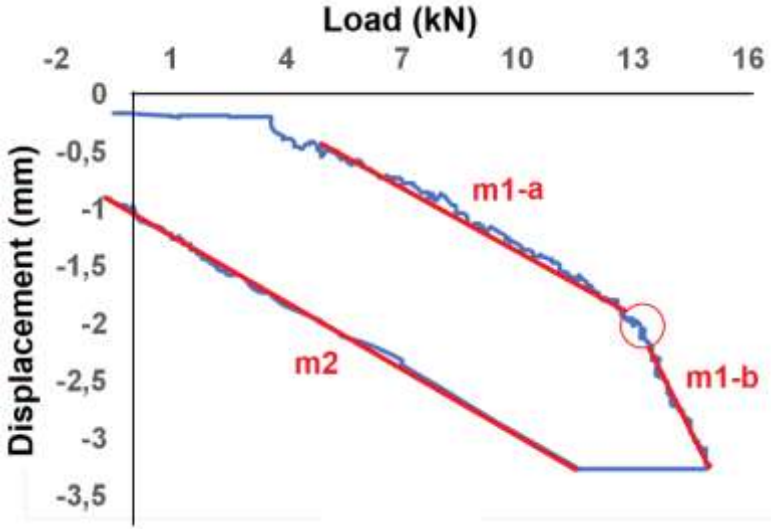

Figure 122 – Load versus displacement for S2 at 15 kN load level

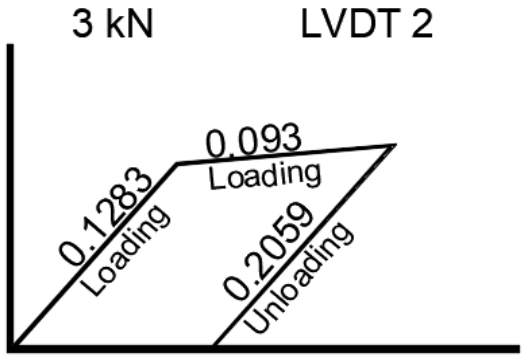

Figure 123 – Slopes for S2 loading-unloading at 3 kN load level

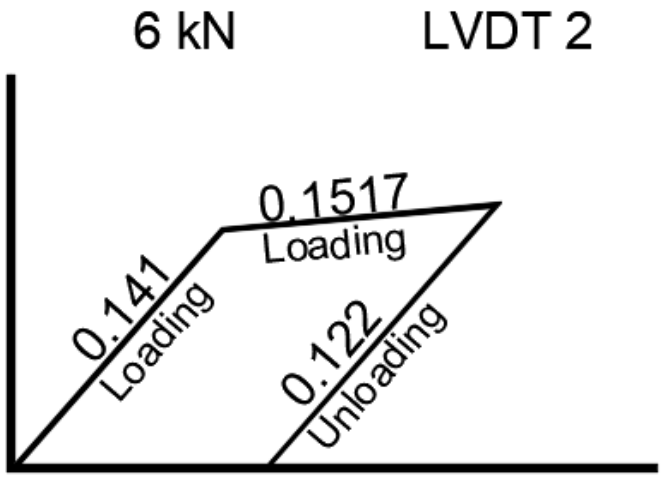

Figure 124 – Slopes for S2 loading-unloading at 6 kN load level

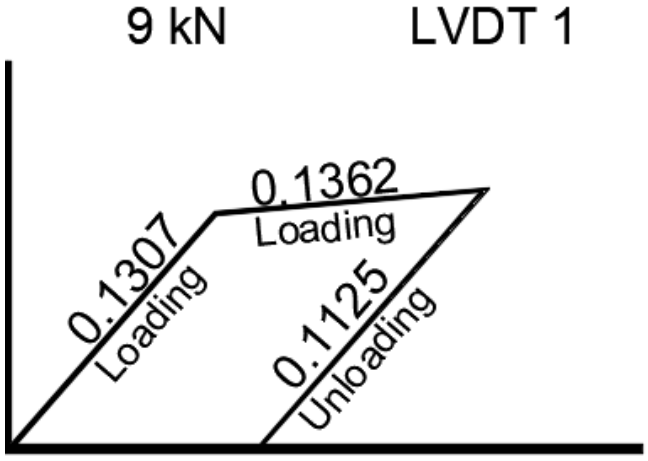

Figure 125 – Slopes for S2 loading-unloading at 9 kN load level

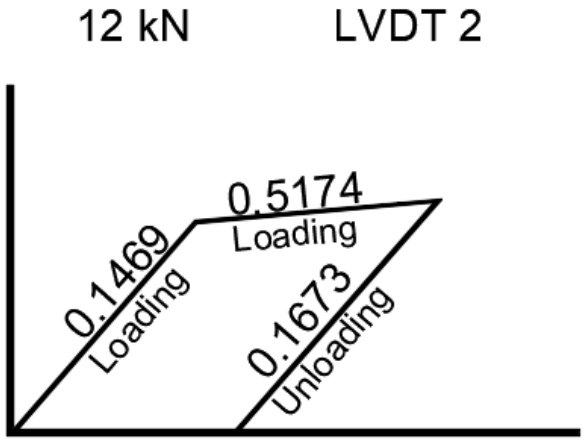

Figure 126 – Slopes for S2 loading-unloading at 12 kN load level

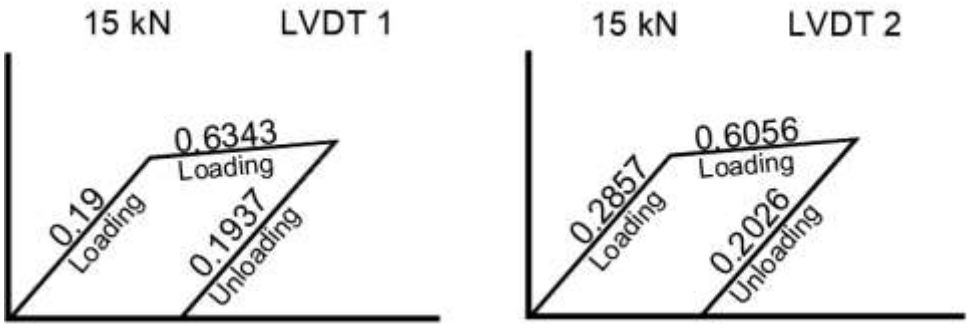

Figure 127 – Slopes for S2 loading-unloading at 15 kN load level

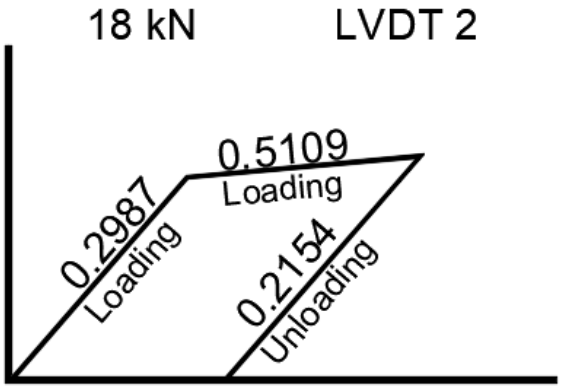

Figure 128 – Slopes for S2 loading-unloading at 18 kN load level

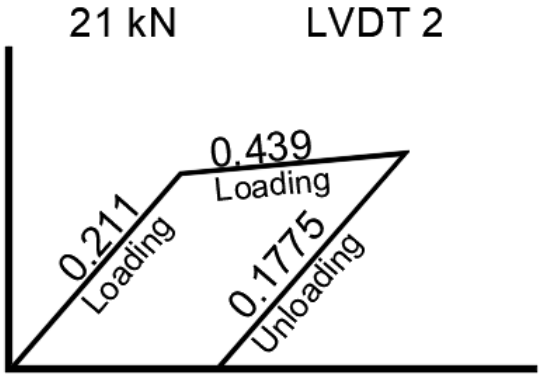

Figure 129 – Slopes for S2 loading-unloading at 21 kN load level

4.6. Mapping the crack depth

The use of Model 2, based in the works of Christides and Barr (1984) and Sinha et al. (2002) was made in a different form. Instead of assigning a crack depth and then find the corresponding loss of stiffness factor (Friswell and Penny, 2002), in this paper the loss of stiffness was first assigned and the models for two slabs S1 and S2 (isotropic

and orthotropic) were checked in frequency and mode shape with the experimental data from modal testing as a reference. With great correspondence from Model 2 to experimental data, it is possible to find the equivalent crack depth in each element using Equation 14. The crack is equivalent since each element can have a crack or can be in the area of influence produced by a crack. The results of crack depth mapping are shown in Figure 130 for S1 and Figure 131 for S2. A great advantage of the Model 2 it that it is possible to detect the areas more penalized by cracks or its influence.

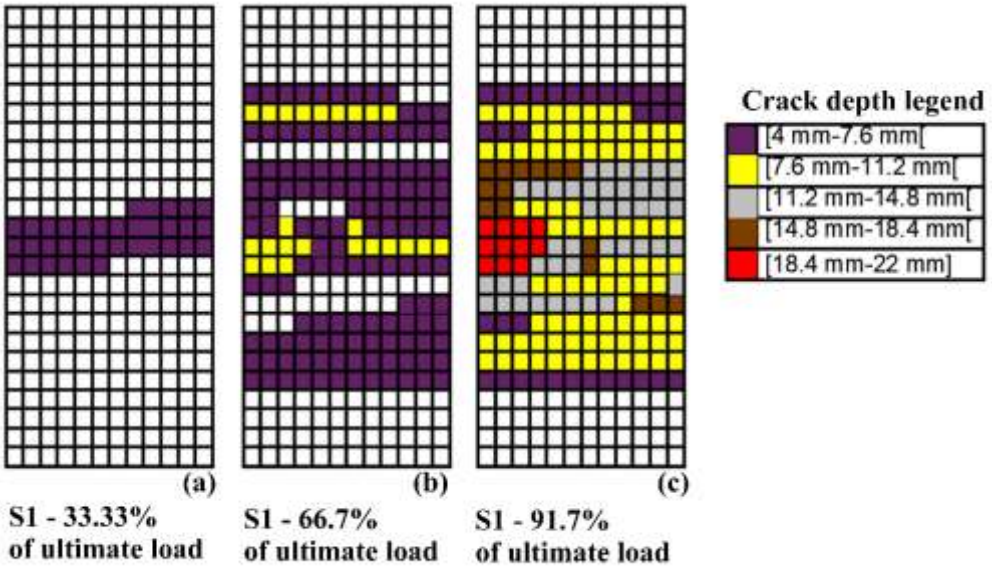

Figure 130 – Crack mapping for S1

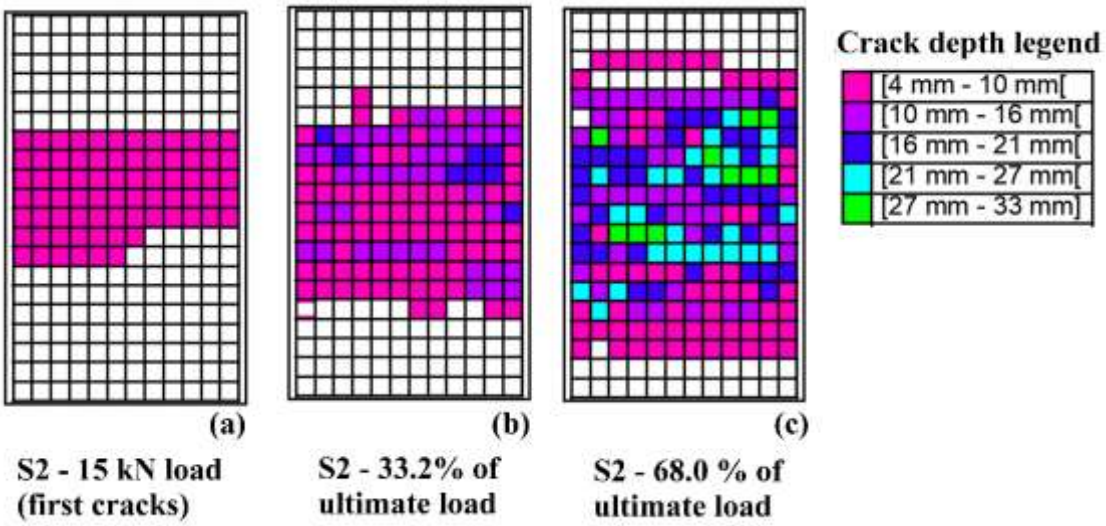

Figure 131 – Crack mapping for S2

5. CONCLUSIONS

Two reinforced simply supported concrete slabs, named S1 and S2, were tested. Although they had the same support conditions, dimensions and reinforcement ratios were distinct between them, highlighting that the reinforcement ratio of S2 was the highest. Different behaviour was observed from the results of the modal test between the slabs, that could be related to the differences in the cracking pattern. First, the variation of the first natural frequency for different damage levels was evaluated. The S1 presented monotonic decrease of the fundamental frequency as the static load increased (and so the induced crack). On the contrary, S2 presented a decrease of natural frequency until about 40% of collapse load and then it became steady until the last load level tested.

A global damage index based on a relationship between the fundamental natural frequency of each slab with respect to the natural frequency of the uncracked state was evaluated and both slabs showed similar behavior until a certain value of the damage (0.3); after that the slabs showed different pattern. This behavior of changes of the damage index followed the pattern of variation of the natural frequencies in both slabs, since the damage index was based on changes of the natural frequency. However, the rise of nonlinear effects for high levels of damage might cause the use of natural frequency not suitable in terms of identifying the level of damage, as it occurred in S2. On the other hand, the correlation between the damage index and the gradient was significant for low levels of damage, making it possible to relate the gradient to the intensity of damage.

Two numerical models were then elaborated for both slabs following the same rules, one based on a relationship of the inertia of the regions that reached the cracked moment (named Model 1) and the other based on the stiffness reduction caused by visible cracks (named Model 2). Isotropic and orthotropic elements were tested for both models. For S2, until the load of 12 kN, no cracks were visible and the cracking moment was not reached, but there was a frequency reduction (observed through modal testing), so the use of moment trapezoid distribution rules in order to proportionally reduce stiffness produced good results. A possible cause for this frequency decrease can be the existence of microcracks around reinforcement due to an acccommodation. This rule of trapezoid distribution was applied in both slabs in the elements that did not present visible cracks (Model 2) or haven’t reached the cracking moment (Model 1).

Comparing frequency results, Model 2 produced better adjustments in comparison to Model 1, for both slabs. The reason is that Model 1 penalizes all the elements the same way, not considering that uncracked elements have higher stiffness than a cracked one. Model 2, on the other hand, consider the effects of cracks in the element and its neighborhood using a triangular distribution but requiring a dense mesh to properly apply this distribution. When MAC indicator was used to evaluate both models it was shown that the four models in S2 produced similar results. For S1, Model 2 (iso and orthotropic) produced higher MAC values (what implies in a better correlation) in comparison to Model 1.

Although the models were checked for unloading stage (modal testing is performed after the load application and beams removal), the comparison of slopes for the same load level shows that the models can be used for loading stage. The changes of slope for different levels is expected since reinforced concrete is a nonlinear material when subjected to loading-unloading stages.

In general, the Model 2 was an inverse approach of what was proposed by their original authors. As the stiffness reduction factors for all load levels had great correspondence in frequency and mode shapes, it is possible to find the corresponding crack depth in each element to each load level, that can be useful in for future works. The proposed methodology can be associated to a cracking prediction algorithm that can apply reduction factors and, comparing the results with experimental data, find crack distribution and depth.

REFERENCES

ABNT (Associacao Brasileira de Normas Técnicas). NBR 6118:14. Projeto de estruturas de concreto – Procedimento. 2014

ACI (American Concrete Institute). Building Code Requeriments for Structural Concrete (ACI 318). 1995.

Allemang, RJ. (2003). The modal assurance criterion - Twenty years of use and abuse. Sound & vibration. 37(8):14-23.

Alves, H.; Diógenes, H.; Cossolino, L. C.; El Debs, M. K.; Debs, A.. (2011). Determination of modulus of elasticity of concrete from the acoustic response. IBRACON Structures and Materials Journal. 4. 792-813.

Andreaus U., Baragatti P. (2009). Fatigue crack growth, free vibrations, and breathing crack detection of aluminium alloy and steel beams. The Journal of Strain Analysis for Engineering Design, Vol. 44, No.7, pp. 595–608.

Andreaus, U., Casini, P. and Vestroni, F. (2007), "Non-linear dynamics of a cracked cantilever beam under harmonic excitation." International Journal of Non-Linear Mechanics, Vol 42, pp. 566–575.

Andreaus, U. and Baragatti, P. (2011), "Cracked beam identification by numerically analyzing the nonlinear behavior of the harmonically forced response." Journal of Sound and Vibration, Vol. 330, pp. 721-742.

Brechlin, E., Bendel, K., Keiper, W., (1998), "A New Scaled Modal Assurance Criterion for Eigenmodes Containing Rotational Degrees of Freedom", Proceedings, International Seminar on Modal Analysis,ISMA 23, Vol. 3, pp. 1175-1182

Bovsunovsky, A. P. (2004). The mechanisms of energy dissipation in the non-propagating fatigue cracks in metallic materials. Engineering Fracture Mechanics, 71(16–17), 2271–2281.

Bovsunovsky, A. P. and Surace, C. (2005), "Considerations regarding superharmonic vibrations of a cracked beam and the variation in damping caused by the presence of the crack." Journal of Sound and Vibration, Vol. 288, pp.865-886.

Cao, M.; Radzieński, M.; Xu, W.; Ostachowicz, W. (2014). Identification of multiple damage in beams based on robust curvature mode shapes, Mechanical Systems and Signal Processing, v. 46, n. 2, p. 468-480.

Cao MS, Sha GG, Gao YF, Ostachowicz W (2017) Structural damage identification using damping: a compendium of uses and features. Smart Materials and Structures 2017; 26(4): 43001.

Carneiro, S. H., Inman, D. J. (2002) Continuous model for the transverse vibration of cracked Timoshenko beams, Journal of Vibration and Acoustics, Vol. 124, Issue 2, pp. 310-320. https://doi.org/10.1115/1.1452744

Castel, A.; Vidal, T.; Francois, R. (2012), Finite-Element Modeling to Calculate the Overall Stiffness of Cracked Reinforced Concrete Beams. Journal of Structural Engineering-Asce. 138. 889-898..

Capozucca, R., Magagnini, E. (2017), "Analysis of cracked RC beams under vibration." 12th International Conference on Damage Assessment of Structures. Journal of Physics: Conference Series 842:012076.

Cawley, P., Adams, R. D. (1979) The location of defects in structures from measurements of natural frequencies.Journal of Strain Analysis,Vol. 14, Issue 2, pp. 49–57.

Cheng, S. M., Swamidas, A. S. J., Wu, X. J. and Wallace, W. (1999), "Vibrational response of a beam with a breathing crack." Journal of Sound and Vibration, Vol. 225, No. 1, pp. 201–208.

Chen, S. G., Zhao, J., Makurat, A., et al. (2000) "Mesh size influence on dynamic modeling," Fragblast, V. 4, Issue. 2, pp. 164–74.

Chen, W.; Lui, E. M., (2004) Handbook of structural engineering. Second Edition, CRC Press.

Christides, S., Barr, A.D.S (1984) One-dimensional theory of cracked Bernoulli-Euler beams. International Journal of Mechanical Science, Vol. 26, Issue 11/12, pp. 639–648. https://doi.org/10.1016/0020-7403(84)90017-1

Chondros, T. G., Dimarogonas, A. D. and Yao, J. (2001), "Vibration of a beam with a breathing crack." Journal of Sound and Vibration, Vol. 239, No. 1, pp. 57–67.

Cole, A. (1975), On-line failure detection and damping measurement of aerospace structures by random decrement signature. NASA CR 2205.

Das, S.; Saha, P.; Patro, S.K. (2016) Vibration-based damage detection techniques used for health monitoring of structures: A review. J. Civ. Struct. Health Monit, Vol. 6, pp. 477–507.

Dessi, D.; Camerlengo, G.. (2015). Damage identification techniques via modal curvature analysis: Overview and comparison. Mechanical Systems and Signal Processing, v. 52-53, p. 181-205.

Dixit, A., Hanagud, S. (2011) Single beam analysis of damaged beams verified using a strain energy based damage measure, International Journal of Solids and Structures, Vol. 48, Issue 3-4, pp. 592-602. https://doi.org/10.1016/j.ijsolstr.2010.10.025

Doebling, S.W.; Farrar, C.R.; Prime, M.B.; Shevitz, D.W. (1996) Damage Identification and Health Monitoring of Structural and Mechanical Systems from Changes in their Vibration Characteristics: A Literature Review; Los Alamos National Laboratory Report, LA-13070-MS; Los Alamos National Laboratory: Los Alamos, NM, USA.

Ebrahimian H, Astroza R, Conte JP, Callafon RA (2017) Nonlinear finite element model updating for damage identification of civil structures using batch Bayesian estimation. Mechanical Systems and Signal Processing, 84:194-222 part B.

Ewins, D., (1985). Modal Testing: Theory and Practice. New York: Wiley

Fan, W. and Quiao, P. (2010), "Vibration-based Damage Identification Methods: A Review and Comparative Study." Structural Health Monitoring, Vol. 10, No. 1, pp. 83–111.

Frans, R.; Arfiadi, Y.; Parung, H.. (2017). Comparative Study of Mode Shapes Curvature and Damage Locating Vector Methods for Damage Detection of Structures. Procedia Engineering, v. 171, p.1263-1271.

Fregolent, A., D'Ambroglo, W., (1997), "Evaluation of Different Strategies in the Parametric Identification of Dynamic Models," ASME Conference on Mechanical Vibration and Noise, Paper DETC97VIB4154

Freitas, M. L. (2019) Um modelo computacional para simulação do comportamento mecânico de lajes lissuradas. Dissertacao de Mestrado. PEC/UFJF.

Friswell, M. I., and Penny, J. E. T. (2002), "Crack Modeling for Structural Health Monitoring," Structural Health Monitoring: An International Journal, V. 1, No. 2, pp. 139–48.

Frizzarin, M., Feng, M. Q., Franchetti, P., Soyoz, S., & Modena, C. (2008). Damage detection based on damping analysis of ambient vibration data. Structural Control and Health Monitoring, n/a-n/a. https://doi.org/10.1002/stc.296

Gianninni, O., Casini, P., Vestroni, F. (2003). Nonlinear harmonic identification of breathing cracks in beams. Computers & Structures, Vol. 129, pp. 166-177.

Guedes, T. O. (2016), Avaliação do estado de fissuração de lajes convencionais utilizando testes modais. Dissertação de mestrado. PPGECAM/UFPB..

Gurutzeaga, M. Oller, E., Ribas, C., Cladera, A., Marí, A. (2015), "Influence of the longitudinal reinforcement on the shear strength of one-way concrete slabs. Materials and Structures/Materiaux et Constructions, vol. 48, issue 8, pp. 2597–2612.

Hamad, W., Owen, J. S., Hussein, M. F. M. (2010) Modelling the nonlinear behaviour of a cracked reinforced concrete beam". International Conference on Computing in Civil and Building Engineering, 2010.

Han, D. (2011), Experimental and theoretical investigation of the crack behavior of RC-slabs subjected to biaxial bending, Ph.D. Thesis, Universität der Bundeswehr München, Neubiberg, Germany.

Han, D., Keuser, M., Zhao, X. and Langer, B. (2011), "Influence of transverse reinforcing bar spacing on flexural crack spacing on reinforced concrete." Procedia Engineering, Vol. 14, pp. 2238-2245.

Heylen, W., (1990), "Extensions of the Modal Assurance Criterion," Journal of Vibrations and Acoustics, Vol. 112, pp. 468-472.

Heylen, W., Lammens, S., (1996) "FRAC: A Consistent way of Comparing Frequency Response Functions", Proceedings, International Conference on Identification in Engineering, Swansea, pp. 48-57.

Hsu TY, Shiao SY, Liao WI, Loh CH (2014) The Pseudo Local Flexibility Method for Hyper-static Beams: An Experimental Study. Procedia Engineering 2014; 79:550–554..

Hunt, D. L., (1992)"Application of an Enhanced Coordinate Modal Assurance Criterion (ECOMAC)," Proceedings, International Modal Analysis Conference, pp. 66-71.

Hunt DL, Weiss SP, West WM, Dunlap TA, Freemeyer SR. (1990)"Development and implementation of a shuttle modal inspection system". Journal of Sound and Vibration, Vol. 24, issue 9, pp. 34–42.

Jassim, Z.A.; Ali, N.N.; Mustapha, F.; Abdul Jalil, N.A. (2013) A review on the vibration analysis for a damage occurrence of a cantilever beam. Eng. Fail. Anal. Vol. 31, pp. 442–461.

Jiao, Y.; Liu, H.-B.; Cheng, Y.-C.; Gong, Y.. (2015). Damage Identification of Bridge Based on Chebyshev Polynomial Fitting and Fuzzy Logic without Considering Baseline Model Parameters. Shock and Vibration, v. 2015, pp. 1-10.

Lee, Y. and Chung, M. (2000). A study on crackdetection using eigenfrequency test data. Computers and Structures, Vol. 77, pp. 327–342.

Lantsoght, E. O. L., Veen, C. and Walraven, J. C. (2013), "Shear in one-way slabs under concentrated load close to support." ACI Structural Journal, Vol. 110, pp. 275-284.

Lieven, N., and Ewins, D., 1988. "Spatial correlation of mode shapes: The coordinate modal assurance criterion (COMAC)".Proceedings of the 6th International Modal Analysis Conference, Kissimmee, Florida, USA,1, p. 690-695

Lifshitzand, J.M.; Rotem, A. (1969) "Determination of Reinforcement Unbonding of Composites by a Vibration Technique". J. Compos. Mater. 1969, 3, 412–423.

Limongelli MP, Carvelli V (2015) Damage localization in a glass fiber reinforced composite plate via the surface interpolation method. Journal of Physics: Conference Series 2015; 628:12095.

Meruane, V. N. (2016) Damage Assessment Algorithms for Structural Health Monitoring, Structural Health Monitoring Technologies and Next-Generation Smart Composite Structures, Chapter 7, (2016), 225-286. https://doi.org/10.1201/9781315373492-8

Metha, P.K.; Monteiro, P.J.M. (1994). Concreto: estrutura, propriedades e materiais. São Paulo: Pini.

Milecek, S., (1994) "The Use of Modal Assurance Criterion Extended," Proceedings, International Modal Analysis Conference, pp. 363-369.

Mitchell, L. D., (2001) "Increasing the Sensitivity of the Modal Assurance Criteria to Small Mode Shape Changes: The IMAC," Proceedings, International Modal Analysis Conference, pp. 64-69.

Modena C, Sonda D, Zonta D. (1999) "Damage localisation in reinforced concrete structures by using damping measurements". Key Engineering Materials, Vol. 167–168, pp. 132–141.

Nandi, A. K., Neogy, S. (2002) Modelling of a Beam with a Breathing Edge Crack and Some Observations for Crack Detection, Journal of Vibration and Control, Vol. 8, Issue 5, pp. 673-693. https://doi.org/10.1177/1077546029296

Nefske, D.J., and Sung, S.H., (1996) "Correlation of a coarse-mesh finite element model using structural system identification and a frequency response assurance criterion," Proc. the 14th International Modal Analysis Conference, pp. 597-602.

Neild, S. A., Williams, M. S. and McFadden, P. D. (2003), "Nonlinear vibration characteristics of damaged concrete beams." Journal of Structural Engineering, Vol. 129, No. 2, pp. 260–268.

Ngan, J. W., Caprani, C. C., and Bai, Y. (2019) "Full-field finite element model updating using Zernike moment descriptors for structures exhibiting localized mode shapes," Mechanical Systems and Signal Processing, Vol. 121 , pp. 373–88

Nguyen, K. V. (2013), "Comparison studies of open and breathing crack detections of a beam-like bridge subjected to a moving vehicle." Engineering Structures, Vol. 51, pp. 306–314.

O'Callahan, J., (1998) "Correlation Considerations – Part 4 (Modal Vector Correlation Techniques)," Proceedings, International Modal Analysis Conference, pp. 197-206.

Pan, J., Zhang, Z., Wu, J., Ramakrishnan, K. R., & Singh, H. K. (2019). A novel method of vibration modes selection for improving accuracy of frequency-based

damage detection. Composites Part B: Engineering, 159, 437–446. https://doi.org/10.1016/j.compositesb.2018.08.134

Pandey, A. K., & Biswas, M. (1994). Damage Detection in Structures Using Changes in Flexibility. Journal of Sound and Vibration, 169(1), 3–17. https://doi.org/10.1006/jsvi.1994.1002

Pandey A K, Biswas M, and Samman M M (1991). Damage detection from changes in curvature mode shapes. Journal of Sound and Vibration , 145(2): 321-332.

Paolo C., Fabrizio V., Oliviero G. (2014). Crack detection in beam-like structures by nonlinear harmonic identification. Fracture and Structural Integrity 29. DOI: 10.3221/IGF-ESIS.29.27.

Park, L.; Paulay, T. (1975) Reinforced Concrete Structures. Wiley.

Pastor, M., Binda, M., & Harčarik, T. (2012). Modal Assurance Criterion. Procedia Engineering, 48, 543–548. https://doi.org/10.1016/j.proeng.2012.09.551

Patil, D. P., Maiti, S. K. (2003) Detection of multiple cracks using frequency measurements. Engineering Fracture Mechanics, Vol. 70, Issue 12, pp. 1553–1572. https://doi.org/10.1016/S0013-7944(02)00121-2

Pérez, M. A., and Serra-López, R. (2019) "A frequency domain-based correlation approach for structural assessment and damage identification," Mechanical Systems and Signal Processing, V. 119, pp. 432–56.

Pešić N, Živanović S, Dennis J, Hargreaves J (2015) Experimental and finite element dynamic analysis of incrementally loaded reinforced concrete structures. Engineering Structures;103: 15–27. https://doi.org/10.1016/j.engstruct.2015.07.037.

Pillai, S. U.; Menon, D. (2005) Reinforced concrete design. Second Edition, McGraw-Hill.

Qiao, P.; Lestari, W.; Shah, M.; Wang, J. (2007). Dynamics-based damage detection of composite laminated beams using contact and noncontact measurement systems, J. Comput. Math., v. 41, n. 10, p. 1217–1252

Ratcliffe, C.P. (1997). Damage detection using a modified Laplacian operator on mode shape data, J. Sound Vibration, v. 204, n. 3, p. 505–517.

Ratcliffe, C. P. (2000). A Frequency and Curvature Based Experimental Method for Locating Damage in Structures. Journal of Vibration and Acoustics, Vol. 122, Issue 3, pag. 324-329.

Roy, K.. (2017). Structural Damage Identification Using Mode Shape Slope and Curvature. Journal of Engineering Mechanics, v.143, n. 9, p. 1-12.

Romanchenko, I. V., Ulmaskulov, M. R., Sharypov, K. A., Shunailov, S. A., Shpak, V. G., Yalandin, M. I., … Rostov, V. V. (2017). Four channel high power rf source with beam steering based on gyromagnetic nonlinear transmission lines. Review of Scientific Instruments, Vol. 88, Issue 5, 54703. https://doi.org/10.1063/1.4983803

Rytter A (1993) Vibration based inspection of civil engineering structures, PhD Thesis, Department of Building Technology and Structural Engineering, Aalborg University, Denmark.

Rucevskis, S., Janeliukstis, R., Akishin, P. and Chate, A. (2016), "Mode shape-based damage detection in plate structure without baseline data." Structural Control and Health Monitoring, Vol. 23, No. 9, pp. 1180–1193

Saadat, S., Noori, M. N., Buckner, G. D., Furukawa, T., Suzuki, Y. (2004). Structural health monitoring and damage detection using an intelligent parameter varying (IPV) technique. International Journal of Non-Linear Mechanics, Vol. 39, No. 10, pp. 1687-2697. DOI: 10.1016/j.ijnonlinmec.2004.03.001

Shen, M.-H. H., Pierre, C. (1990) Natural modes of Bernoulli–Euler beams with symmetric cracks. Journal of Sound and Vibration, Vol. 138, Issue 1, pp. 115–134. https://doi.org/10.1016/0022-460X(90)90707-7

Sinha, J.K., Friswell, M.I, Edwards, S. (2002) Simplified models for the location of cracks in beam structures using measured vibration data. Journal of Sound and Vibration, 251(1) (2002), 13–38. https://doi.org/10.1006/jsvi.2001.3978

Sinou, J.-J. (2009). A Review of Damage Detection and Health Monitoring of Mechanical Systems from Changes in the Measurement of Linear and Non-linear Vibrations. Mechanical Vibrations: Measurement, Effects and Control, Nova Science Publishers, pp. 643-702.

Springer W T, Lawrence K L, Lawley T J (1988). Damage assessment based on the structural frequency-response function.Experimental Mechanics, 28(1): 34-37.

Wahab, M.M. A.; G. DE Roeck, G. (1999). Damage detection in bridges using modal curvatures: application to a real damage scenario, Journal of Sound and Vibration, v. 226, n. 2, p. 217-235.

Waltering, M., Bungard, V., Maas, S., De Roeck, G. (2008). Damage assessment of a gradually damaged prestressed concrete bridge using static load tests and non-linear vibration characteristic. International Conference on Noise and Vibration Engineering, Vol. 6, pp. 3383-3397.

Wang, L., Zhou, X., Liu, H. and Yan, W. (2012), "Damage detection of RC beams based on experiment and analysis of nonlinear dynamic characteristics." Construction and Building Materials, Vol. 29, pp.420–427.

Wei, J. C., Wang, W., Allemang,R. J., (1990) “Model Correlation and Orthogonality Criteria Based on Reciprocal Modal Vectors,” Proceedings, SAE Noise and Vibration Conference. pp. 607-616.

Yao, S., Zhang, D., Chen, X., Lu, F. and Wang, W. (2016), “Experimental and numerical study on the dynamic response of RC slabs under blast loading.” Engineering Failure Analysis, Vol. 66, pp. 120-129.

Xu, T., Huang, J., Castel, A., Zhao, R. and Yang, C. (2018), Influence of steel–concrete bond damage on the dynamic stiffness of cracked reinforced concrete beams. Advances in Structural Engineering, Vol. 21, Issue 13, pp. 1977–1989.

Xu, T. and Castel, A. (2016), “Modeling the dynamic stiffness of cracked reinforced concrete beams under low-amplitude vibration loads.” Journal of Sound and Vibration, Vol. 368, pp.135–147.

Xu, Y.F.; Zhu, W.D.; Smith, S.A. (2017). Non-model-based damage identification of plates using principal, mean and Gaussian curvature mode shapes. Journal of Sound and Vibration, v. 400, p. 626-659

Zanuy, C., Maya-Duque, L.F., Gallego, J. M. and de la Fuente P. (2014), “Damage identification of RC bridge decks under fatigue loading.” Informes de La Construcción Vol. 66 (EXTRA 1), pp. 1-11.

Zhu, X. Q. and Law, S. S. (2007), “Nonlinear characteristics of damaged reinforced concrete beam from Hilbert-Huang transform.” Journal of Structural Engineering, Vol. 133, No. 8, pp.1186–1191.

Zou, Y., Tong, L., Steven, G. P. (2002) Vibration-Based Model-Dependent Damage (delamination) Identification and Health Monitoring for Composite Structures — a Review, Journal of Sound and Vibration, Vol. 230, Issue 2, pp. 357-378. https://doi.org/10.1006/jsvi.1999.2624